The Dissertation Committee for Terence Travis Garner certifies
that this is the approved version of the following dissertation:

Characterization of Transport Properties in Granitic Rock Fractures with Skins

Committee:

John M. Sharp, Jr., Supervisor

Philip C. Bennett

Randall J. Charbeneau

Randall Marrett

James R. Mayer

Characterization of Transport Properties in Granitic Rock Fractures with Skins

by

Terence Travis Garner, B.S.

Dissertation

Presented to the Faculty of the Graduate School
of The University of Texas at Austin
in Partial fulfillment
of the requirements
for the Degree of

Doctor of Philosophy

The University of Texas at Austin
May 2007

Dedication

To my wife Susan, who without I would not have begun this journey.

Acknowledgements

Thank you to John Lansdown and Todd Housh for helping me experience the UT ICP lab. Dick Sanders and Jim Mayer at the University of West Georgia, Thank you for helping analyze complicated samples that I could not resolve at UT. Thank you to Kitty Milliken for teaching me to use the SEM and EPMA and her help with interpreting images produced in the lab. For all things concerning sample preparation and equipment oriented, thanks to Greg Thompson and Roger Gary. Frank Roberts, Cold Spring Granite, Kevin Carey and Family, and Keystone Granite all helped with access to field sites in one form or another, thank you. Thanks to all my field assistants: Nedra and David Bonal, Don Slottke, Brad Wolaver, and Joel Stevens. Thank you to Bea Garcia-Fresca, Jeff Landrum, and especially Wendy Robertson, who listened to my constant rambling concerning details of this project. Thank you to Neville Robinson, Craig Simmons, Rowl Twidale, and Jennie Bourne, my Aussie collaborators who all assisted and inspire me. Thank you to Jack, Phil, and my committee for advice and opinions. Funding for this project came from multiple awards from the Jackson School of Geosciences, the GSA student research grant, and the National Science Foundation.

Characterization of Transport Properties
in Granitic Rock Fractures with Skins

Publication No. ______

Terence Travis Garner, PhD
The University of Texas at Austin, 2007

Supervisor: John M. Sharp, Jr.

Hydraulic properties of fracture skins in granitic rocks from three climatically different field sites show that fracture skins can increase permeability, compared to unaltered granite, through microfractures or weathering rinds, or decrease it through the effects of mineral nucleation or precipitation and growth of biological organisms. In comparable granitic crystalline rocks, fracture skins formed in more arid climates have a higher porosity than fracture skins formed in more humid climates. Granite fractures have been collected from three field sites Elberton, Georgia, Fredericksburg, Texas, and Eyre Peninsula, South Australia. Fracture skins in Elberton are predominantly surface coatings of dust films, clay infillings, organic growths, and infillings of iron precipitates. Town Mountain Granite skins are dominated by iron banding, weathering rinds, and surface coatings of pyrolusite. The Calca Granites from the Eyre Peninsula have similar fracture skins to the Town Mountain Granite, but skin thicknesses are greater. Modeling studies with fracture skins demonstrate that the most important hydraulic properties are skin porosity, diffusion coefficients, and retardation. Through combined laboratory analyses and field investigations, the variations in transport properties of rock matrix and fracture alteration zones are documented. Transport properties of fracture skins in granitic rocks with surface coatings enhance fracture transport and alteration zones of more porous skins attenuate transport. A new laboratory method is employed to measure diffusion coefficients using laser ablation ICP-MS. Diffusive transport is shown to be preferential to grain boundaries and zones of mineral cleavage planes. Tracer tests show channeling to be a significant factor in breakthrough results on the field scale. Channels on the field scale are imaged using high frequency GPR providing an image of preferential flow paths in a fracture.

Table of Contents

Chapter 4: Field Scale Tracer Tests and Channel Imaging 124

Table of Tables

Chapter 2

Chapter 3

Chapter 4

Table of Figures

Chapter 1

Chapter 2

Chapter 3

Chapter 4

Chapter 1

Introduction

The term “fracture skin” was coined by Wohletz (1981) and given a formal definition by Moench (1984). Moench defined a fracture skin as “a thin skin of low-permeability material, deposited on the surfaces of the blocks, that serves to impede the free exchange of fluid between the blocks and fissures”. Since then, the term has grown to include, not only coatings that impede flow, but any physical, chemical, or biological alteration at the fracture surface that can enhance or impede fluid flow and solute transport (Kreisel and Sharp, 1996; Landrum, 2000; Robinson et al., 1998; Sharp, 1993; and Zimmerman et al., 2002).

In crystalline rock, fracture skins can increase porosity through microfractures and weathering rind formation, while skin porosity can decrease through the effects of mineral nucleation or precipitation and growth of biological organisms. Fracture skin formation is a function of the local environment. Because much of the Earth's surface is igneous or metamorphic rock (~34%), we require a better understanding of how groundwater flows and contaminants are transported in media where fractures are the primary conduits for groundwater flow. This is critical in developing and maintaining potable water for growing populations and for contamination mitigation.

This study holds significance on multiple scales and disciplines. On a microscopic scale, unaltered rock is different in terms of appearance and physical properties. On a larger scale, the loss of mass transported into fracture skins can be significant when considering the lateral extent of a fracture skin. In terms of discipline, reservoir exploitation and management for water and petroleum, storage reservoirs, waste depositories, and waste remediation must consider fractured rock with fracture skins. Understanding fracture skin development and rates of development allows for accurate assumptions to be made when dating land surfaces.

The field evidence for fracture skins is abundant, but understanding how, where, and why they form is not fully understood. The literature contains many studies looking at flow and transport in unaltered fracture systems (e.g., Cook and Simmons, 2000); some have looked at the influence on flow and transport in fractures with fracture skins (Fu et al., 1993; Kreisel, 1996; Kreisel and Sharp, 1996; Landrum, 2000; Phyu, 2002; Robinson et al., 1998; Sharp, 1993; Sharp et al., 1993; Sharp et al., 1995, and Sharp et al., 1996) and few have studied the influence of residual fractures after the matrix rock has completely weathered (McKay et al., 2000, 1993a, 1993b). In qualitatively determining the weathering sequence of granite in the field, a natural progression of weathering features of granite inselbergs has been observed (Bain 1931, Hutton et al., 1977, Larsen 1948, Loughnan 1969, Twidale 1986, and Twidale et al., 2004).

There have been a number of studies modeling solute transport through fractured porous media with fracture skins, and it has been demonstrated that clay filling, mineral precipitation, and growth of organic material commonly decreases permeability in fracture skins compared to the matrix (Fu, 1993; Kreisel and Sharp, 1996; Landrum, 2000; Phyu, 2002; Sharp, 1993; Sharp et al., 1995). In spite of the existence of fracture skins, the impact of fracture skins on solute transport in fractured granitic rocks is commonly ignored. Prediction work that does account for fracture skins has limited datasets from which to pull transport properties and even if data are readily available fracture systems inherently create uncertainty in predictions. Simply illustrating uncertainty in predicting mass transport in fractured systems, Black (1993) stated that contaminants in fractured rocks appear at places we do not expect faster than we had predicted. This paraphrase has been unofficially referred to as “Black’s Law”.

Methodology

This research project addresses the following questions: 1) how do the hydraulic properties differ with respect to skin type and 2) what local environmental factors influence fracture skin formation and their effects on solute transport? The methodology for addressing these questions will be to: 1) observe physical parameters, field conditions, and different fracture skins formed from exposed granite in three different field sites; 2) use previous studies from the literature and direct measurements to establish transport properties having the greatest effect on model results; 3) use existing laboratory methods to determine significant transport properties and establish new fracture skin evaluation methods; 4) conduct small scale tracer tests to determine flow regime and field scale parameters; 5) establish a mathematical model that best predicts solute transport by incorporating parameters collected in the laboratory and the field; and 6) characterize the fracture skins from the field sites in terms of their potential for enhancing or attenuating transport. Tracer tests through isolated single fractures are conducted at sites in the Eyre

Peninsula, South Australia, and one site in the Llano uplift, Texas.

Granitic fracture skins from three different areas are examined. Local environmental factors and fracture skin types influenced the choice of the field locations. From a relatively wet climate, the Elberton granites are a fine-grained pink granite from Elberton, Georgia (Figure 1.01). The fine to medium grained Town Mountain granite from Fredericksburg, Texas, (Figure 1.02) is from a semi-arid climate. Samples of different texture from the Calca granites from the arid climate of the Eyre Peninsula, South Australia, (Figure 1.03) are also considered.

Hypotheses

I hypothesize that

I. the three field sites represent different fracture skin transport properties;

II. the local environmental factors responsible for variation in transport properties for each field site are:

   i. climate (higher rate of weathering in regions with greater precipitation);

   ii. thickness of overburden (thick saprolite provides increased moisture retention and a source for clay transported into the fracture system);

   iii. texture (small minerals provide greater surface area for reactions to occur) and;

    iv. mineralogy (greater percentage of resistant minerals decreases the rate of weathering);

III. laser ablation inductively coupled plasma mass spectroscopy (LA-ICP-MS) can be used to measure diffusion coefficients for aqueous phase diffusion; and

IV. field tracer tests show attenuation of mass transport in fractured granite with skins that cannot be simulated in the laboratory.

Outline of Chapters

Chapter 2 provides a description of the three field sites and explores the sensitivity parameters significant to transport in fractured mediums. The field description outlines the local environment, fracture skins observed, and measured field parameters. Characterization of the rocks and fracture skins is done using bulk chemical analysis and petrographic analysis.

Chapter 3 introduces and outlines methodologies for determining transport properties. Previously and currently used methods for measuring porosity, retardation factors, and diffusion coefficients are discussed.

Chapter 4 characterizes transport properties determined by field tracer tests. These properties include average linear velocity, hydraulic aperture, and dispersion.

Determining effects of and mapping fracture channels in a fracture are done using ground penetrating radar (GPR).

Chapter 5 outlines the conclusions from the previous chapters, provides an overview of results, and proposes future work to be done.

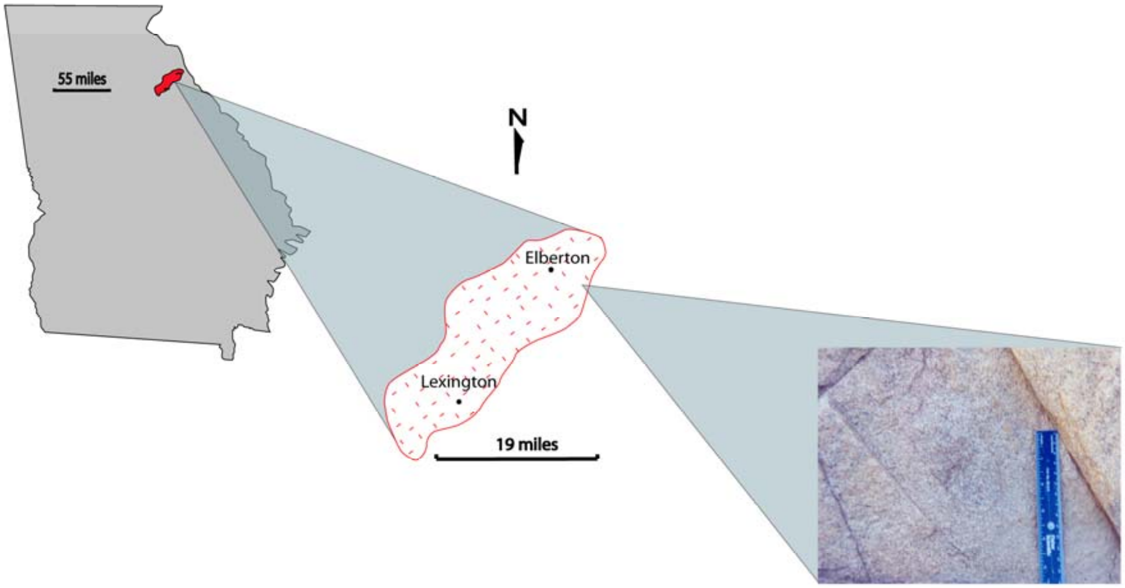

Figure 1.01: Fine grained pink granite from the Elberton Granites from Elberton Georgia.

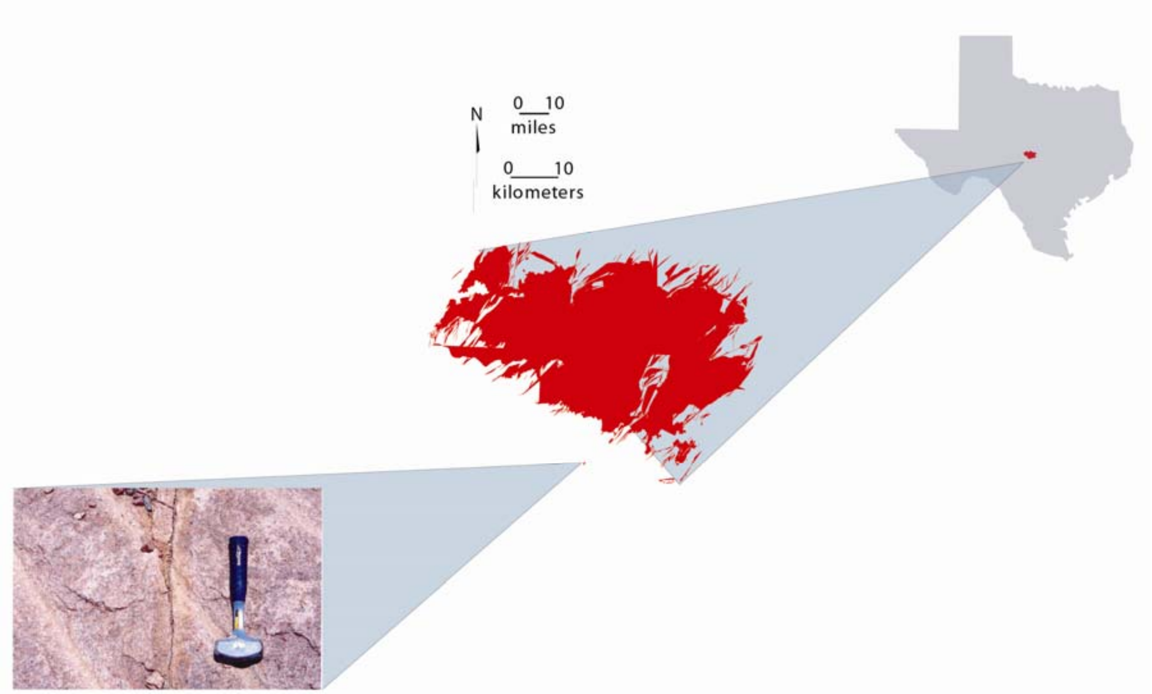

Figure 1.02: Medium grained pink Town Mountain Granite located near Fredericksburg, TX in the Llano uplift.

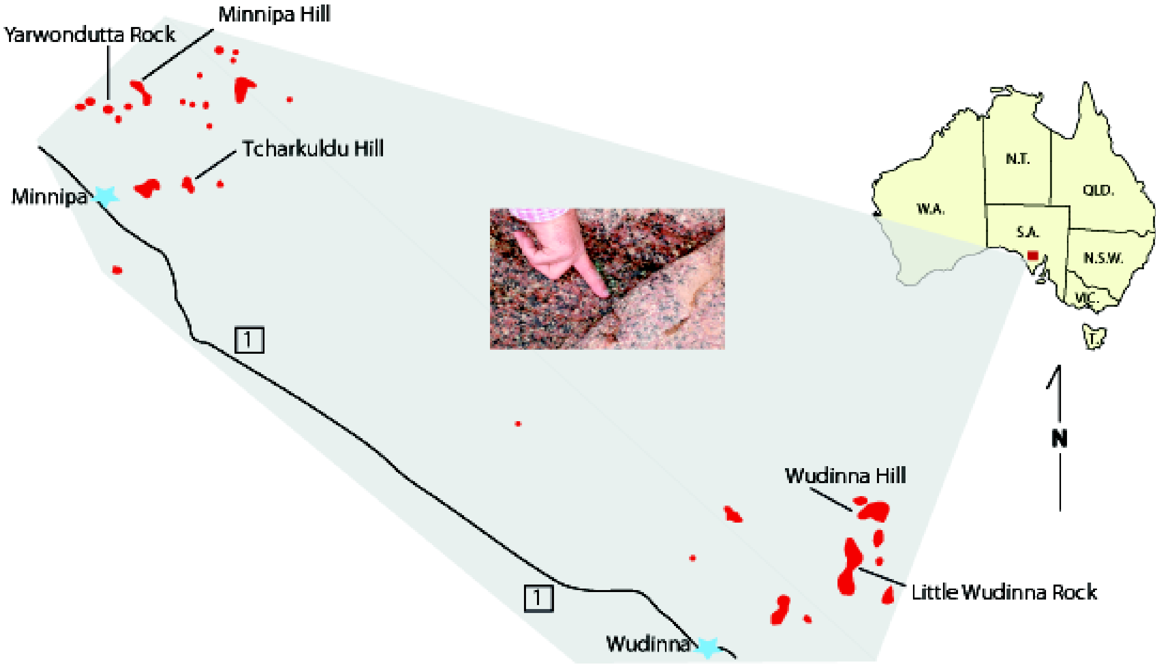

Figure 1.03: Medium grained pink granite of the Calca Granites from Minnipa and Wudina region, South Australia.

Chapter 2

Landscape Variation and Granite Characterization

Introduction

At the field sites of this study, exposed granite is fractured and expresses the domal shape traditional to bornhardts. Surface exposure varies in the field and is hypothesized to affect the type of fracture skin formed and the degree of development. Through bulk chemical analysis, variation in chemistry from matrix to fracture skin is determined. Optical analysis is used to estimate qualitatively how permeability structure varies with fracture skin types. In this chapter, variations in local landscapes of three different field sites are discussed and rock and fracture skin characterization using bulk chemistry and optical analyses are described.

Previous Work

Rock alterations, and their composition, origin, and evolution was first explored by Alexander von Humbolt (1812, trans. Ross 1907). von Humbolt inferred that manganese and iron rock coatings are from a solution of local surface water and groundwater and not the product of rock weathering. Darwin (1897) later explained manganese and iron oxide coatings, from various seashores and riverbanks along his voyage on the H.M.S. Beagle, have similar origins.

Recent investigations of fracture coatings (Carlos, 1985, 1989) show crystallization of heulandite along fractures can be used to determine paleo-vadose zones. Permeability variation in fractured tuffs and liesegang-banded sandstones were explored by Fuller and Sharp (1992) and Fu et al. (1993), respectively. Fu et al. found significant decreases in permeability when pores contained precipitated amorphous iron. This effectively makes a liesegang band a barrier to transport of fluid or mass from a fracture. Thoma et al. (1992) compared water uptake in four fractured tuffs with varying rock coatings. Tuff samples with fracture skins had 5 orders of magnitude decrease of uptake compared with tuffs without skins.

Hydraulic properties of sandstones were measured and modeled by Robinson et al. (1998) showing transport can be enhanced or attenuated by the existence of a fracture skin. Dorn (1998) characterized many rock coatings and other rock alterations. Dorn examined the history, chemical description, and geographic distribution of rock coatings, but hydraulic properties and their effect on flow and solute transport were not addressed. Recently, decreased hydraulic conductivity and permeability from flowmeter tests and pumping tests have been contributed to effects of fracture skins (Ruud and Kabala, 1997 and Kabala, 2001).

In the subdiscipline of geomorphology, extensive work has been done in describing granite weathering and the sequence of alteration that takes place during weathering. Hutton et al. (1977) described the beginning stages of skin formation of norite as

“The course of weathering resulting from the penetration of water joints

> may be followed outwards from the fresh rock corestone into the joint. The first stage of weathering of the norite is represented by the coarse lamination, the next by the finer lamination, and the most advanced by the disappearance of any visible rock with the formation of clay".

Norite is a coarse grained plutonic rock with labradorite is the primary mineral. It is also referred to as black granite. Granite is a coarse-grained plutonic rock containing 10 to 65 percent quartz and 65 to 90 percent of total feldspar is alkali feldspar. The formation of joints and laminations in norite is analogous to granite and the first minerals to weather in both rocks are Ca-plagioclase and mafics. Examination of the chemical composition of the norite corestones and weathered zones show many major cations are recycled in the formation of clay minerals while some are lost to the bulk profile.

An indicator of rapid weathering in granite bornhardts is pitted surfaces (Twidale, 2005). Exposure of granite disks to soil over a period of 4 to 5 years showed reduction of feldspars and mafic minerals. Dixon et al. (2006) suggests that soil overburden expedites the weathering process of granite, forms pitted surfaces, and progresses into weathering rinds.

Field Observations & Rock Descriptions

Fracture skins vary with geographic location and climatic influence (Dorn, 1998). Field sites with different climates are considered: the wettest region is Elberton, Georgia, followed by Fredericksburg, Texas, and finally the driest are the Wudinna and Minnipa region in the Eyre Peninsula and Padthaway, South Australia. Each site has unique fracture skins due to respective fracture origins and climate.

Elberton Granite

The physical appearance of fracture skins in the field vary significantly in Elberton from those from Fredericksburg and the Eyre Peninsula. Fracture skins in Elberton granites range from thin surface coatings of dust films, clay infilling, dendritic and massive pyrolusite coatings, organic infilling (predominantly moss and lichens), and precipitation of amorphous iron (Figure 2.01). Additionally, the Elberton granites have two fracture regimes: vertical and subhorizontal. Vertical fractures are truncated by intersecting sheeting joints.

The Elberton outcrop is divided into two parts. The top portion, ranging from 1 to 4 meters in thickness, has weathered to saprolite while lower portions, about 4 meters high (Figure 2.02 A), are described by Stormer and Whitney (1980) as a 320 million year old, fresh, fine-grained (< 1mm) pink granite. The transition zone from saprolite (Figure 2.02 B) to fresh granite (Figure 2.02 D), contains remnants of consolidated granite with significant weathering rinds of clay and iron precipitates (Figure 2.02 C). Paleofractures within the saprolitic layer are clay-filled with a transition from fracture fill to weathered granite. This transition zone mimics a fracture skin and its formation can be explained by clay transported from the thick saprolite zone above the fractured granite by transient flow or film flow and into the matrix void space by diffusion or capillary forces. Driese et al. (2001) reported zones of low permeability in saprolite caused by clay infilling. This is consistent with the lower porosities measured in the Elberton fracture skins compared to the granite matrix. This type of fracture skin is analogous to case hardening (Dorn, 1998). Decreasing pore throat diameter of a void space increases the capillary forces, which provides a longer water retention time for rate-limited chemical reactions to occur and core softening of the matrix material.

Fracture apertures and skin thicknesses were measured in the field. The mean fracture aperture in Elberton is 1.95×10^{-3} m. For modeling comparison, a minimum (5.0×10^{-4} m) and a maximum (1.0×10^{-2} m) fracture apertures are also considered. Skin thickness ranged from 1.0×10^{-5} m to 5.0×10^{-2} m with a mean of 1.12×10^{-4} m.

Fracture distribution in Elberton did not allow for fracture spacing estimates because of minimal outcrop exposure. Strike and dip of exposed fractures are plotted in rose and equal area diagrams (Figure 2.03). The limited number of fractures (20), make any statistical analysis of orientations problematic, but a single dominant strike direction, north north-west, is apparent. Steeply dipping fractures tend to coincide with the dominant strike direction.

Town Mountain Granite

Town Mountain Granite is a fine to medium grained pink granite dated at ~1.2 billion years (Long, 2003). The granite considered for this study outcrops at Bear Mountain three miles north of Fredericksburg, Texas. The physical appearance of the Town Mountain Granite shows four major types of fracture skins: iron precipitates, weathering rinds, slickenside surfaces, and surface coating of pyrolusite (Figure 2.04).

Unlike the Elberton granites, fracture skins from Fredericksburg are thick and consist of multiple skins. For instance, the most common fracture skin is a white weathering rind on the fracture wall and an iron band of precipitated amorphous iron penetrating beyond the weathering rind.

The soil horizon is thin to nonexistent, which minimizes storage available for slow percolation of fluid into fractures. Weathered granite boulders with pitted surfaces top the bornhardts. Distribution of the boulders is indicative of the existing fracture network. Pitted surfaces with protruding quartz grains are persistent around the boulders. Clay formed by weathering of feldspars has eroded away from the site leaving behind the exposed pitted surface. A profile of a quarry wall (Figure 2.05) shows a high concentration of fractures near the surface with fracture density decreasing with depth. Fracture density measurements were not permitted in the active quarry, therefore estimated thicknesses with fracture densities were made by visual observation.

Fracture geometry measurements in Fredericksburg included fracture aperture, skin thickness, and fracture spacing. Fracture spacing measurements were taken from a scanline through the highly fractured zone just below the boulders. For model input, the arithmetic mean of the fracture spacing (1.31×10^{-2} m) was used in all simulations. The mean, minimum, and maximum aperture measurements are 1.13×10^{-3} m, 2.5×10^{-4} m, and 5.0×10^{-3} m. Skin thickness ranges from 5.0×10^{-4} m to 1.55×10^{-1} m with an arithmetic mean of 2.07×10^{-2} m.

Fracture orientations are plotted in a rose and equal area diagrams (Figure 2.06). From the data, three dominant sets of fractures can be established. The first is striking north-west, the second north-north-west, and the third north-east. Equal area projection shows the dominant strike directions are complimented with steeply dipping fracture planes.

Calca Granite

The geology in the Eyre Peninsula and Padthaway is different from both US field sites. Granite outcrops are bornhardts of Calca Granite dated at 1.519 billion years ± 67 MA (Blissett et al., 1988). Reverse sheeting fractures in the quarries along with A-tent formations indicate the bornhardts are under compressive stress (Twidale et al., 1996). The stresses associated with these topographic features are compressional tectonic as opposed to pressure release from offloading. The result is a significant number of joints and fractures at different stages of skin formation (Figure 2.07).

Skin formation is dominated by weathering rinds and iron banding along the horizontal and sub-horizontal fractures. Throughout the Eyre Peninsula, weathering rinds are thicker than those from the Town Mountain Granite measuring up to 15.5 cm and iron banding is thicker measuring up to 50 cm thick. Visually, fracture skins vary from well developed to beginning stages of development. Early stages of development include those suggested by the two-stage concept of differential weathering (Twidale, 2002). In all three field sites, evidence for differential weathering exists, but the extent of differential weathering can be fully explored in the South Australia region because the various outcrop exposures give a more thorough insite to the weathering sequence.

Vertical weathering profiles were measured from soil horizon to consolidated rock at two sites in the Eyre Peninsula, Yarwandutta Rock, and White's Quarry (Figures 2.08 and 2.09). These profiles show chemical alteration and fracturing is constrained to the upper portion of the outcrop profile. This is similar to the formation of Mn and Fe redox fronts forming at the outcrop surface of fractured shale (Mazurek et al., 1996).

Bulk Chemistry & Mineral Composition

Bulk chemistry is analyzed to quantify variation in chemical composition of the rocks and fracture skins. Trends of cation change from rock matrix to fracture skins indicate the sequence of bulk mineral weathering in the rock. The weathering sequence of minerals follows the Goldich (1938) weathering sequence with loss of mafic and feldspar minerals and the formation of clay.

Bulk chemistry of the rocks sampled was determined using either optical ICP or ICP-MS. Samples were prepared using a fusion method conducted by melting rock samples in a furnace at 1000°C using lithium metaborate ($LiBO_2$) as a flux. Once in the form of a glass bead, samples are dissolved in a 3% nitric acid solution. Analyses of samples included, cations representing the major rock forming minerals in granite, silica (Si), titanium (Ti), aluminum (Al), total iron (Fe), manganese (Mn), magnesium (Mg), calcium (Ca), sodium (Na), potassium (K), and phosphorous (P).

Characterization of granites is commonly done in terms of mineral composition (Blatt and Tracy, 1999). Using the bulk chemical composition acquired from ICP-MS, mineral composition is achieved using Cross, Iddings, Pirsson and Washington (CIPW) normalization. The CIPW normalization program used (Lowenstern, 2000) utilizes a routine that incorporates minerals that are not commonly found in granite (i.e., corundum). By consistently using the same list of minerals for all granites, relative change in the dominant minerals of interest can be estimated. The primary minerals of interest are quartz, orthoclase, plagioclase, hypersthene, and hematite. X-ray diffraction was not used for mineral identification because X-ray diffraction requires mineral abundance to be greater than 5%, and separation of clay minerals from microfractures is problematic.

Elberton, Town Mountain, and Calca Granites classify as alkali granites when plotted on an IUGS classification plot. The use of the IUGS classification plot is not traditionally used to show alteration of quartz and feldspar, but rather to classify igneous rocks based on the percentages of the dominant rock forming minerals. By plotting rock matrix and fracture skins on the IUGS chart a trend of decreasing percentages of plagioclase and orthoclase are evident for all field locations (Figures 2.10, 2.11, and 2.12), which follows the Goldich weathering model. Calcium-rich plagioclase weathers first followed by sodium-rich plagioclase and followed by orthoclase. All rock matrix samples analyzed show higher percentages of Na and K relative to Ca indicating that plagioclase is dominated by high Na.

On the IUGS plots the Elberton granite shows significant loss of feldspar from rock matrix relative to fracture skin. Loss of feldspar in the Town Mountain Granite is not as great as Elberton Granite. Calca Granite shows a similar trend of decreasing plagioclase. The significant change in mineralogy of Elberton Granite is a function of the faster weathering rate inferred from field observations. Also plotted on the Calca Granite plot, are surface coatings despite a chemical difference of what is plotted and what a coating is expected to contain. No obvious trend to plotted surface coatings is seen on the IUGS plot. It is also useful to point out that the IUGS plot only shows variation from rock matrix to alteration with regards to Si, Ca, Na, and K. For example, when feldspar weathers to clay the first weathering product is kaolinite, a two-sheet structure clay that contains significant amounts of Si and Al. As the clay continues to weather, three-sheet structure clay forms and increased substitution of Mg, Na, and Ca occurs.

Further analysis of major cations and the variation from rock matrix to fracture skin compares the weight percent oxide for the cations of interest (Figures 2.13 - 2.26). Variation in cation compositions from rock matrix are shown for liesegang (Fe) bands, surface coatings, and weathering rinds. Many of the samples are associated with the weathering of feldspars and ferromagnesian minerals to clay products. The most common clay minerals are kaolinite, montmorillonite, and illite. Blatt and Tracy (1996) state that clay minerals rarely occur individually. For this reason a combination of commonly occurring clays is associated with the formation of fracture skins in granitic rock. Simple expressions for the weathering of rock forming minerals to clays are (Blatt and Tracy, 1996).

$$3\ \mathrm{KALSi_3O_8} + 2\ \mathrm{H^+} + 12\ \mathrm{H_2O} \rightarrow \mathrm{KAL_3Si_3O_{10}\ (OH)_2} + 6\ \mathrm{H_4SIO_4^o} + 2\ \mathrm{K^+} \tag{2.1}$$

Orthoclase Muscovite

$$2\ \mathrm{KAL_3Si_3O_{10}\ (OH)_2} + 2\ \mathrm{H^+} + 3\ \mathrm{H_2O} \rightarrow 3\ \mathrm{Al_2Si_2O_5(OH)_4} + 2\ \mathrm{K^+} \tag{2.2}$$

Muscovite Kaolinite

$$2\ KALSi_3O_8 + 2\ H^+ + 9\ H_2O \rightarrow Al_2Si_2O_5(OH)_4 + 4\ H_4SiO_4^0 + 2\ K^+ \qquad (2.3)$$

Orthoclase Kaolinite

$$NaAlSi_3O_8 * CaAlSi_2O_8 + H_2O + H^+ \rightarrow$$

Plagioclase

$$(Na, Ca)\ (Al, Mg)_8\ (Si_4O_{10})_4(OH)_8*12\ H_2O + H_4SiO_4^0 + (Na^+, Ca^{2+}) \qquad (2.4)$$

(Na, Ca) Montmorillonite

$$2NaAlSi_3O_8 + 2H^+ + 9H_2O \rightarrow Al_2Si_2O_5\ (OH)_4 + 4H_4SiO_4 + 2Na^+ \qquad (2.5)$$

Albite Kaolinite

$$2K[Mg_2, Fe]\ [Al, Si_3]O_{10}\ (OH)_2 + 0.5O_2 + 6H_2O + 10H^+ \rightarrow$$

Biotite

$$Al_2Si_2O_5(OH)_4 + 2\ K^+ + 4Mg^{2+} + 4H_4SiO_4^0 + 2Fe(OH)_{3.} \qquad (2.6)$$

Kaolinite Amorphous Iron

$$\text{Ferromagnesian minerals} + H^+ + H_2O \rightarrow$$

$$(Na, Ca)\ \text{montmorillonite} + H_4SiO_4 + (Na^+, Ca^+) \qquad (2.7)$$

$$2Fe(OH)_3 \rightarrow Fe_2O_3 + 3H_2O \qquad \text{or}$$

Hematite

$$Fe(OH)_3 \rightarrow FeOOH + H_2O \qquad (2.8)$$

Goethite

Samples E_1 and E_12 are Elberton granites with weathering rinds (Figures 2.13 and 2.16). E_1 is a well developed weathering rind and E_12 being at the very early stages of weathering rind formation. A trend of decreasing Na, Ca (E_12 only), and K is evident in both samples suggesting feldspars weathering to clay. The weathering rind remnants of sample E_1 shows an increase in Si and Ti were E_12 decreases Si and Ti but Al and Fe increase. In all samples with weathering rinds, the accompanying iron bands appear to be the weathering reaction front. Weathering of sample E_1 being a weathering rind, is more advanced than that of E_12 making transport or leaching of clay from the sample an important physical weathering mechanism for increasing porosity and permeability of the alteration zone of weathering rinds. Samples with early stages of chemical weathering appear to be clay filled and potentially decreasing uptake of mass from a fracture by diffusion.

The Elberton Granites are younger and, generally, show less weathering rind formation. The dominant fracture skins in outcrop are surface coatings of predominantly clay with some iron staining. Pyrolusite is a minor surface coating through the outcrops. Samples E_5 and E_10 (Figures 2.14 and 2.15) represent mixed iron and clay coating (E_5) and clay coating (E_10). E_5 mimics the analytical results of E_1 with the difference that Si and Ti are decreasing in the skin. E_10 only shows a decrease in P. Potential differences between fracture skin and rock matrix could be retention of detrital clay in E_10 and transport of mass into the fracture out of the skin for sample E_5.

Town Mountain Granite is dominated by the formation of weathering rinds and iron bands. Outcrop exposures contained pyrolusite coatings. Surface coating of pyrolusite were prevalent on vertical and sub-vertical fractures. Formation of weathering rinds and iron bands occurred predominantly in sub-horizontal fractures. The physical appearance of iron bands varies from sample to sample but they can be characterized by formation of darker bands at the transition from iron band boundary between matrix and weathering rind. In some samples iron bands show uniform color through the width of the band and in some iron bands are not visible.

Four samples (Table 2.02) from the Town Mountain Granite were analyzed: two that did not have iron bands (Figures 2.17 and 2.19) and two did have iron bands (Figures 2.18 and 2.20). The samples without iron bands show varied increased and decreased cations. This suggests weathering products could vary or cation exchange is occurring through the fracture skins because different extents of clay formation could allow additional absorption making cation concentrations vary. Sample F_1 has a fracture alteration of a thin weathering rind and most cations increase in cation concentration in the skin suggesting clay formation and the zone of reaction is at the weathering rind matrix boundary. Sample F_11 represents a slickenside surface were cations decrease in concentration. Through the process of block movement, minerals at the fracture surface rotate and decrease in size. The more resistant minerals would become relatively large and increase in concentration (i.e., quartz). Fault gauge is primarily made of softer minerals and easily washed from the fracture surface.

Samples F_4 and F_12 both have iron bands. Sample F_4 has the darker bands on either side of the band and sample F_12 is uniform in color through the band. Sample F_12 shows the expected decrease in cations, except Fe and Si, from rock matrix to iron band to weathering rind. This progression represents the weathering front moving uniformly through the sample with mass being removed from the iron band and weathering rind by diffusion. Sample F_4 shows a similar progression only into the iron band. Cation concentrations of all, except Fe, increase in the weathering rind, consistent with clay retention in the weathering rind. These two samples illustrate the importance of removal of mass from the alteration zone to the fracture.

Figure 2.21 shows the bulk chemical analysis of granite and alteration from Padthaway, located south of Adelaide, South Australia. These samples incorporate visibly different granites with more well-developed, pitted surfaces. Bulk chemical analysis shows decrease in feldspar forming cations in the pitted weathering rind and increased in Fe, Ca, and Ti in the iron band. No obvious variation from trends is seen in the alteration of the rock.

From the southern portion of the field site in the Eyre Peninsula, samples were analyzed from Mount Wudina (Figure 2.22) and nearby Wudina Quarry (Figure 2.23). Both samples are clay coatings from fractured, exposed bornhardts. Alteration of the fracture zones consisted of tafoni, pitted surfaces, and clay coatings. Tafoni are granite blocks with caverns or hollows forming on the underside. The sites are under compressional stress which is evidenced by A-tent formation at Mount Wudina and reverse faults at Wudina Quarry. Local stress is contributed to the lack of weathering rind formations because greater compressional stress creates a smaller aperture along the flanks of bornhadts. Bulk chemical analyses show increased cation concentrations in Mount Wudina fracture skins and decreases in rock matrix from Wudina Quarry. For clay coating samples, these inconclusive trends mimic those from the Elberton Granite samples.

Fracture alteration of the Calca Granites includes clay coatings, iron bands, weathering rinds, and pyrolusite coatings. A sample of thin weathering rind with some iron banding from Tcharkuldu Hill (Figure 2.24) was analyzed. It is expected that rind formation at Tcharkulda is at an early stage because the outcrop at this site has a mantle residual soil and vegetation covering portions of the outcrop. Chemical analyses show increased cation concentrations in the fracture skins suggesting early rind development and retention of clay minerals in the iron band and weathering rind.

White's Quarry showed the most well-developed weathering rinds of the sampled sites. The first sample analyzed WC_6 (Figure 2.25) has a pitted surface with an abrupt transition from weathering rind to rock matrix. Notable in the sample is the high iron content in the fracture skin. This is attributed to the terrarosa overburden that was removed at the surface prior to quarrying. Both terrarosa and calcrete overlie the outcrop. The Si concentration in the sample increases significantly as expected for a pitted surface. Pits are generally formed by loss of feldspar and ferromagnesium minerals.

The second sample WC_7 (Figure 2.26) from White's Quarry has a thick white weathering rind, ~5cm, with a sharp transition into an iron band than gradually transitions into the rock matrix. Chemical analysis shows retention of clay in the fracture skins through increasing cation concentrations. Outcrop conditions show fracture aperture widening into the alteration zone and the fracture filling with decomposed weathering rind. Under these site conditions, clay transported from the fracture skin would have no place to go except to be deposited in the fracture and slow physical transport out of the skin.

Optical Analysis

Alteration of fracture surfaces includes mineral dissolution, precipitation, and microfracturing. In some cases, the alteration cannot be seen in hand-sample. Optical analysis helps identify mineralogy and types of alteration, as well as inferring the permeability structure and how solute transport would be affected.

Elberton Granite

Field identifications of fracture skins show surface coatings of clay and iron. In order to determine effects of the fracture skins on solute transport greater description is required. Thin sections are made from Elberton granite samples with representative fracture alteration. Optical microscopy and Electron-Probe Micro-Analyzer (EPMA) are used to determine alteration types and extent of skin penetration into the rock.

To get an idea of how a selection of thin sections appear on a larger scale, thin sections are scanned using a flatbed scanner with increased resolution (Figure 2.27). Impregnating samples with blue epoxy prior to the thin sectioning process, *insitu* porosity can be observed. In the Elberton granites, blue epoxy did not penetrate into the rock matrix in samples with surface coatings. This implies the fracture skin acts as a barrier between the rock matrix and the open fracture.

Plain light optical microscopy shows clay formation in microfractres and no visible effective porosity available in the fractures. Images from optical microscopy are combined with an image of a hand sample to show relative locations of plain light images

(Figure 2.28). Using optical microscopy alone is inconclusive for determining extent of alteration. Therefore, EPMA is used to obtain a higher resolution visualization of the fracture skins.

EPMA images from the Elberton Granites show precipitation of clays minerals inside void spaces of microfractures, chlorite precipitation on the fracture surfaces perpendicular to microfracturing, and deformation of the quartz crystals parallel to the fracture (Figure 2.29). EPMA analysis implies the structure of fractures and fracture skins act as a barrier to flow and transport. In particular, images suggest case hardening of the fracture surface by precipitated or detrital clay infiltrating from above in the granite outcrop. Moving from the fracture surface towards the matrix of the rock, alteration of the minerals is evident (Figure 2.30). This is shown in Figure 2.30 by alteration of biotite and feldspars to clay minerals in an enlarged fracture. Transport pathways in the rock matrix appear to be enhanced along grain boundaries and through fracturing or cleavage of the minerals (Figure 2.31). Figure 2.31 also suggests that the rock matrix is “relaxed” near the fracture surface because of the increased visible porosity. This would imply a zone of increased porosity where otherwise visible alteration is not seen.

Town Mountain Granite

Fracture alterations for the Town Mountain Granite from Fredericksburg, TX consist of predominantly dual zones of weathering rind and iron band. Thin sections from the flatbed scanner, using blue epoxy, show significant increase in *insitu* porosity in the weathering rinds and decreases in porosity in the iron bands (Figure 2.32 A, B, C, and

E), relative to the visible rock matrix porosity. Also shown, figure 2.32 D is the relative shallow penetration of epoxy of slickenside material.

Thin sections of weathering rinds commonly display micro-fractures horizontal to the main fracture surface. Hutton et al. (1977) contributes weathering rind formation to the preexistence of laminations parallel to dominant fractures. The smaller horizontal micro-fractures support this theory.

Optical microscopy proved more useful in showing fracture skin formations of Town Mountain Granite than it did for the Elberton Granites. The cross-sectional image, (Figure 2.33) is of a Town Mountain Granite sample with a well formed weathering rind and uniform iron band. Plain light microscopy images illustrate the visible available effective porosity in the weathering rind, the blocked pore space along microfractures and cleavage planes created by precipitation of amorphous iron, and the enhanced transport of epoxy around grain boundaries in the rock matrix.

Samples further from the fracture surface also show porosity in the grain boundaries. Yellow, orange, white, and black colors are quartz crystals from the rock matrix of a hand sample of Town Mountain granite (Figure 2.34). The blue along the mineral boundaries shows penetration of blue epoxy into the sample. In some samples, microfracturing of minerals is prevalent beyond the visible alteration of a hand sample (Figure 2.35).

In hand sample, the zones of visible alteration are iron banding and weathering rinds for most Town Mountain granite samples. The iron banding section at 2x magnification shows precipitation of amorphous iron along grain boundaries, microfractures, and cleavage planes (Figure 2.36). Biotite appears to be relatively unaltered compared to the plagioclase. In the weathering rind of the Town Mountain Granites, clay formation occurs along feldspar grain boundaries (Figure 2.37).

Calca Granite

Calca Granites are coarse grained and the weathering rind formations are thicker than in other field sites. Thin sections of samples show the fracture surface at the top of each image with thick weathering rinds that transition into iron band and rock matrix (Figure 2.38). The visible porosities of the samples are greatly increased in the weathering rinds relative to iron bands and rock matrix. Large weathering rind formation on a sample from White's Quarry with an abrupt change into iron banding then a gradual transition into rock matrix is shown as a representative sample of Calca Granite with alteration at the fracture surface (Figure 2.39).

South Australia's Calca Granite is an alkali-rich granite composed predominantly of orthoclase with lamella of albite. This texture is referred to as perthitic. The perthite in the samples is abundant throughout and is significant to the potential transport of solutes. Albite weathers faster than orthoclase and the surface reaction removing albite from a perthitic texture has been documented and referred to as etch pits by Lee and Parsons (1995). The secondary electron microscope (SEM) images shown by Lee and Parsons show rectangular plugs of albite removed from the host orthoclase. In optical microscopy albite is granular while the host orthoclase remains consolidated (Figure 2.40). In figure 2.40 A and B the images are identical but shown in plain light (A) and polarized light (B). The plain light image shows significantly increased porosity through the albite and orthoclase with the albite acting as the main flow pathway through a weathering rind sample. Polarized light shows the brittle deformation to the albite and the perthitic texture.

Comparing the texture seen in the weathering rind to the perthitic texture relatively unaltered (Figure 2.41), the albite lamella are more competent in the rock matrix. For a sample of inferred rock matrix, clay formation occurs along the mineral boundaries in the sample. As in the Town Mountain Granite, the rock matrix appears to be undergoing alteration. The alteration appears to be more surface reaction along grain boundaries and the visible porosity does not appear to be as significant as in the Town Mountain Granites.

A representative sample of Calca granite with a clay coating was sampled from Minnipa Hill (Figure 2.42). The clay coating is shown at 10x magnification and zones of yellow and orange can be seen at the rim of a feldspar crystal and in the weathered cleavage planes.

Conclusions

Three different granites from different climatic regions are sampled for alterations along fracture surfaces, Elberton Granite, Town Mountain Granite, and Calca Granite. Site observations, bulk chemical analyses, and optical analyses, indicate formation of granite fracture skins are a function of:

1) thickness of overlying soils;

2) compressional stress;

3) fracture orientation;

4) external sources (soluble salts); and

5) petrology and mineral textures.

Transport of solutes through fractures with alterations is affected by how a fracture skin forms. Therefore, understanding skin formation is a first step in determining how fracture skins affect transport.

All fracture skin samples are taken in the shallow subsurface. Outcrop profiles show fracture skin formation and rock alteration is more pervasive in the top few meters at all locations. At sites with thicker overlying soils, fracture alterations are dominated by clay coating, iron-stained surfaces, pitted surfaces, and overall increasing cation concentrations in the alteration zones. If well exposed outcrops are under compressional stress, fracture apertures are tighter and mimic results of outcrops with clay coating.

Weathering rinds and iron bands tend to form along sub-horizontal fractures. The fracture orientation allows prolonged fluid penetration into the rock from the fracture. Vertical fractures are dominated by surface coatings, particularly pyrolusite, controlled by redox reactions which require the loss of fluids for coatings to form.

In the Calca Granites, soluble salts have been cited (Bradley et al., 1978) as a contribution to the formation of tafoni. The early stage of tafoni formation is synonymous with fracture skin formation. Soluble salts are transported into fractures by infiltrating rainfall where the water dries allowing salts to deposit in the available pore space. As the salt crystallizes it expands and physically breaks minerals, thereby increasing surface area available for chemical weathering.

Perthitic texture is shown through optical analysis to provide direct reaction pathways through consolidated orthoclase crystals in Calca Granite. Without a perthitic texture, Town Mountain Granite disaggregates around mineral boundaries, which potentially slows the rate of weathering. The region, where Town Mountain Granite is found, is a source of gruss, which is mined for use as gravel.

Granite fracture skin formation is not the same in three different geographic locations. The influences on fracture skin formations, listed above, combine with local climatic and time of outcrop exposure to create a dynamic sequence to rock alteration that is independent from site to site.

Iron Precipitates and Clay Coating

Organics and Clay Coating

Clay Coating

Clay Infilling in Residual Fractures

Figure 2.01: Photos showing various alteration types from the Elberton Granite.

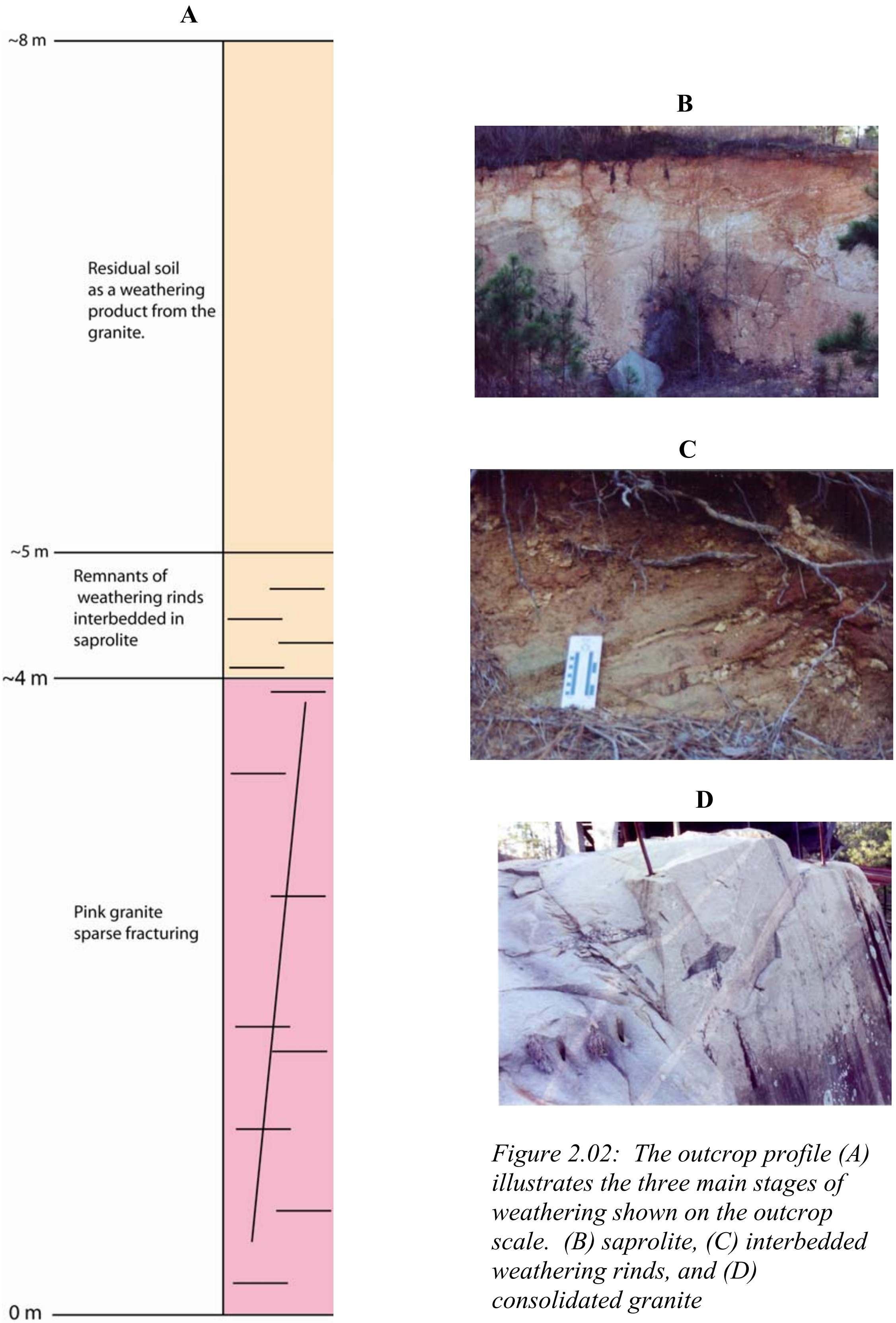

Figure 2.02: The outcrop profile (A) illustrates the three main stages of weathering shown on the outcrop scale. (B) saprolite, (C) interbedded weathering rinds, and (D) consolidated granite

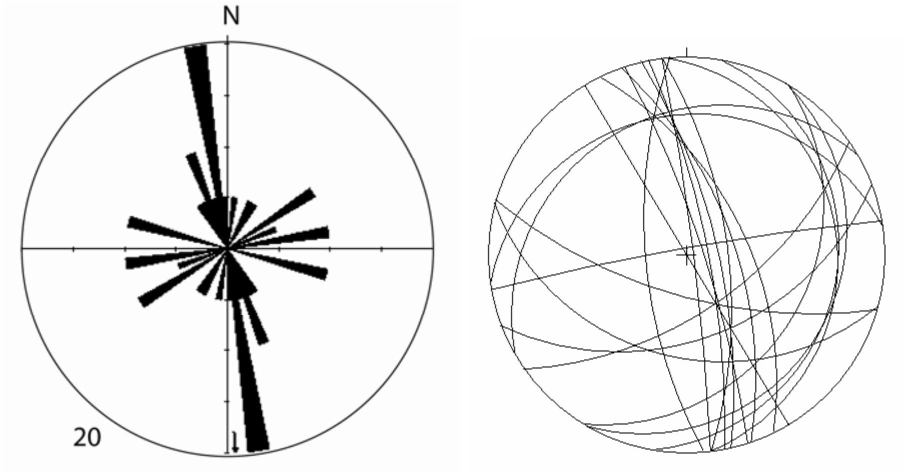

Figure 2.03: Rose and equal area diagrams plotted from 20 strike and dip measurements taken from Elberton.

Iron precipitation

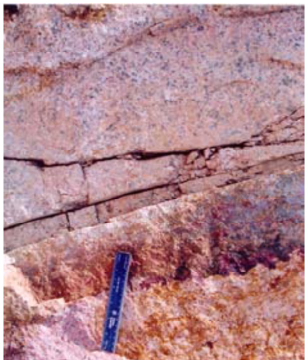

Formation of weathering rind and migration of iron precipitation

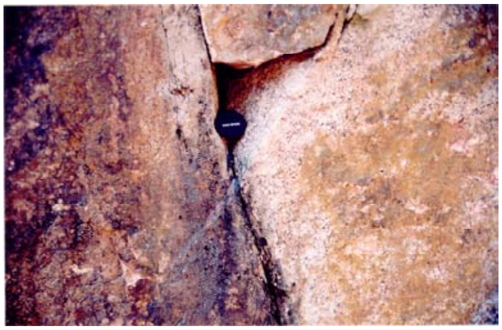

Pyrolusite coating

Weathering rind

Figure 2.04: Photos showing various alteration types from the Town Mountain Granite in Fredericksburg, Texas.

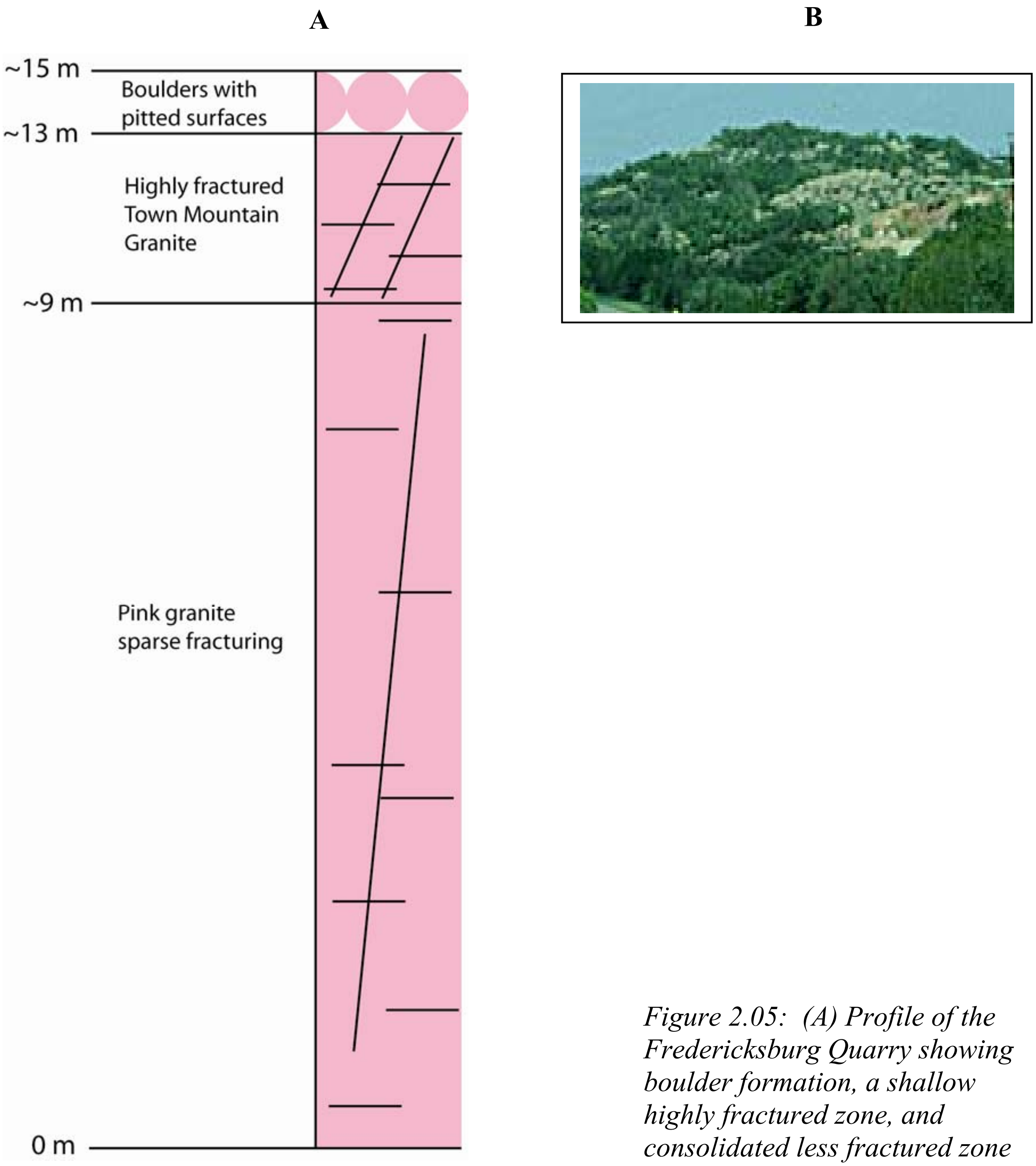

Figure 2.05: (A) Profile of the Fredericksburg Quarry showing boulder formation, a shallow highly fractured zone, and consolidated less fractured zone at the base(B) picture of Bear Mountain.

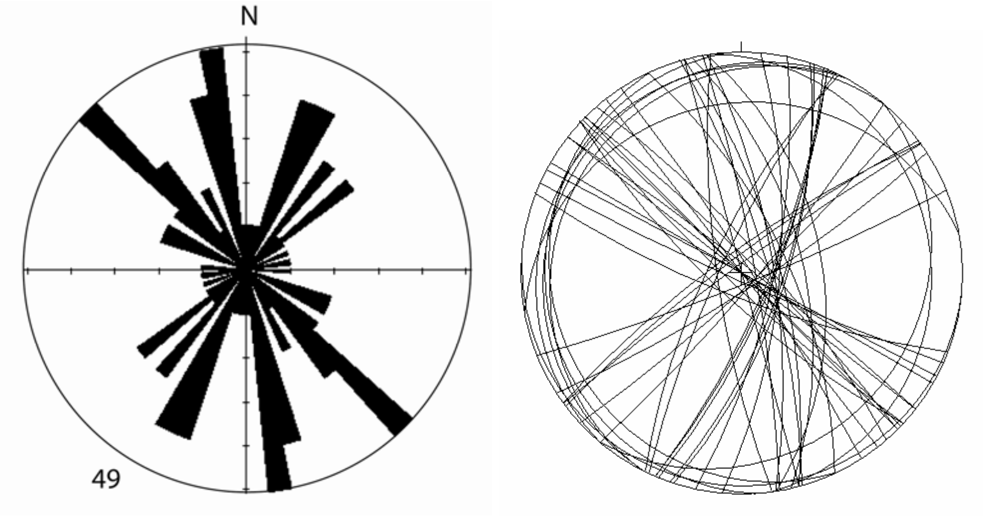

Figure 2.06: Rose and equal area diagrams plotted from 49 strike and dip measurements taken from Bear Mountain north of Fredericksburg.

Weathering rinds & Fe banding Pyrolusite and clay coatings

Leaching from soil contact Weathering rinds & Fe banding

Close-up of a pitted surface Pitting at edge of quarry wall

Figure 2.07: Photos showing various alteration types from the Calca Granites in the Wudina and Minnipa, South Australia

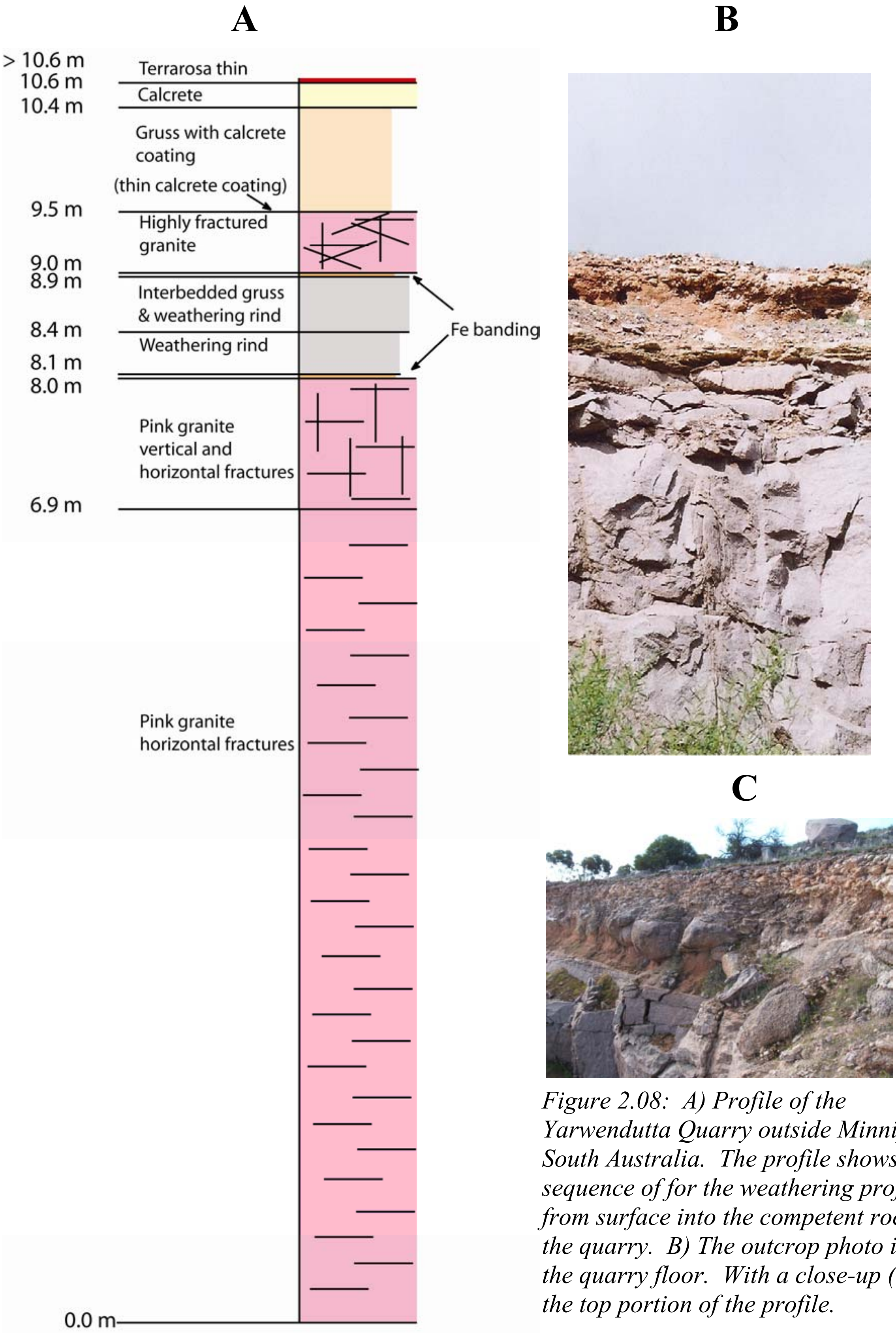

Figure 2.08: A) Profile of the Yarwendutta Quarry outside Minnipa, South Australia. The profile shows the sequence of for the weathering profile from surface into the competent rock in the quarry. B) The outcrop photo is from the quarry floor. With a close-up (C) of the top portion of the profile.

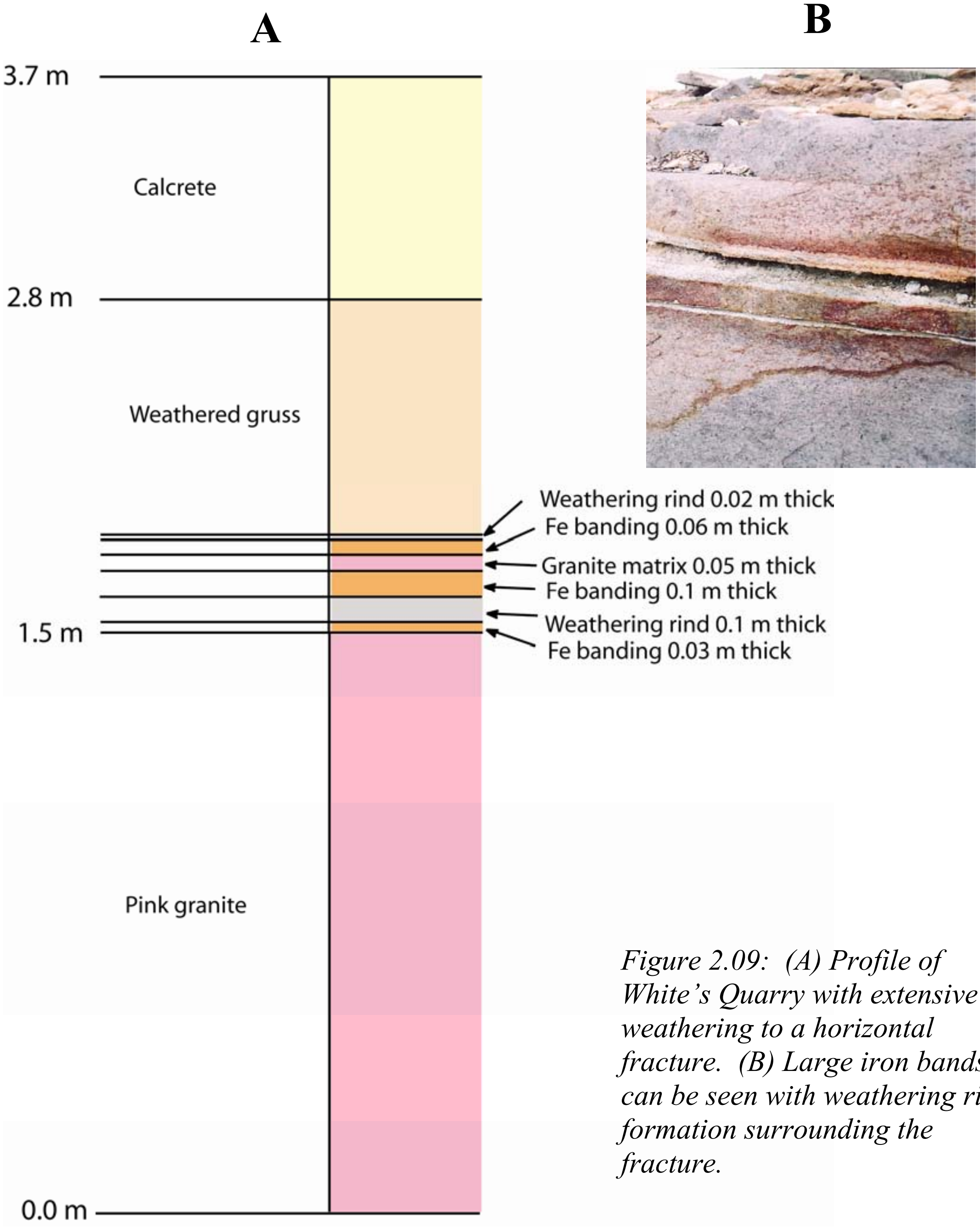

Figure 2.09: (A) Profile of White's Quarry with extensive weathering to a horizontal fracture. (B) Large iron bands can be seen with weathering rind formation surrounding the fracture.

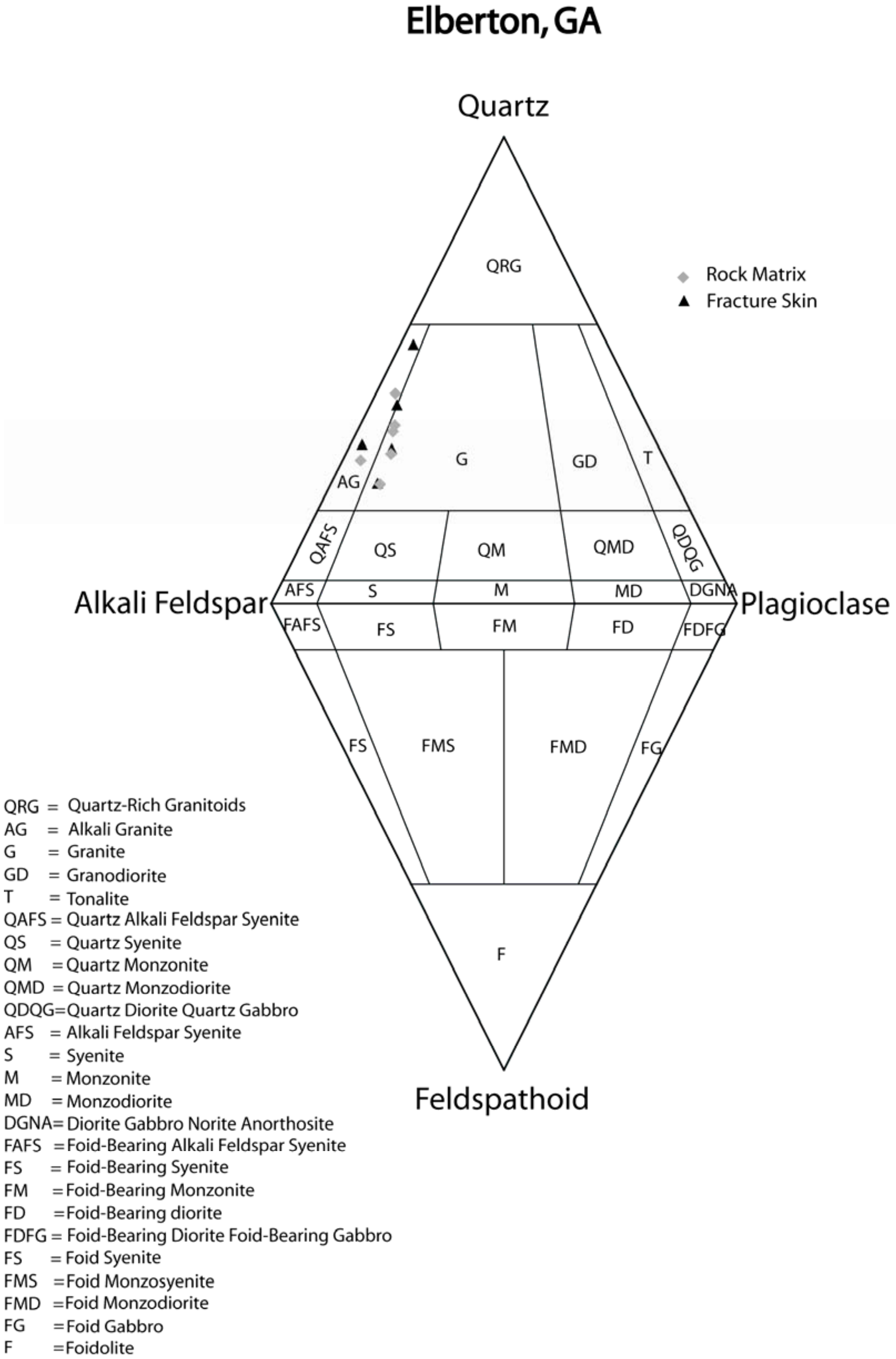

Figure 2.10: IUGS Plot showing Elberton rock matrix alteration trending towards more alkali and quartz rich granite.

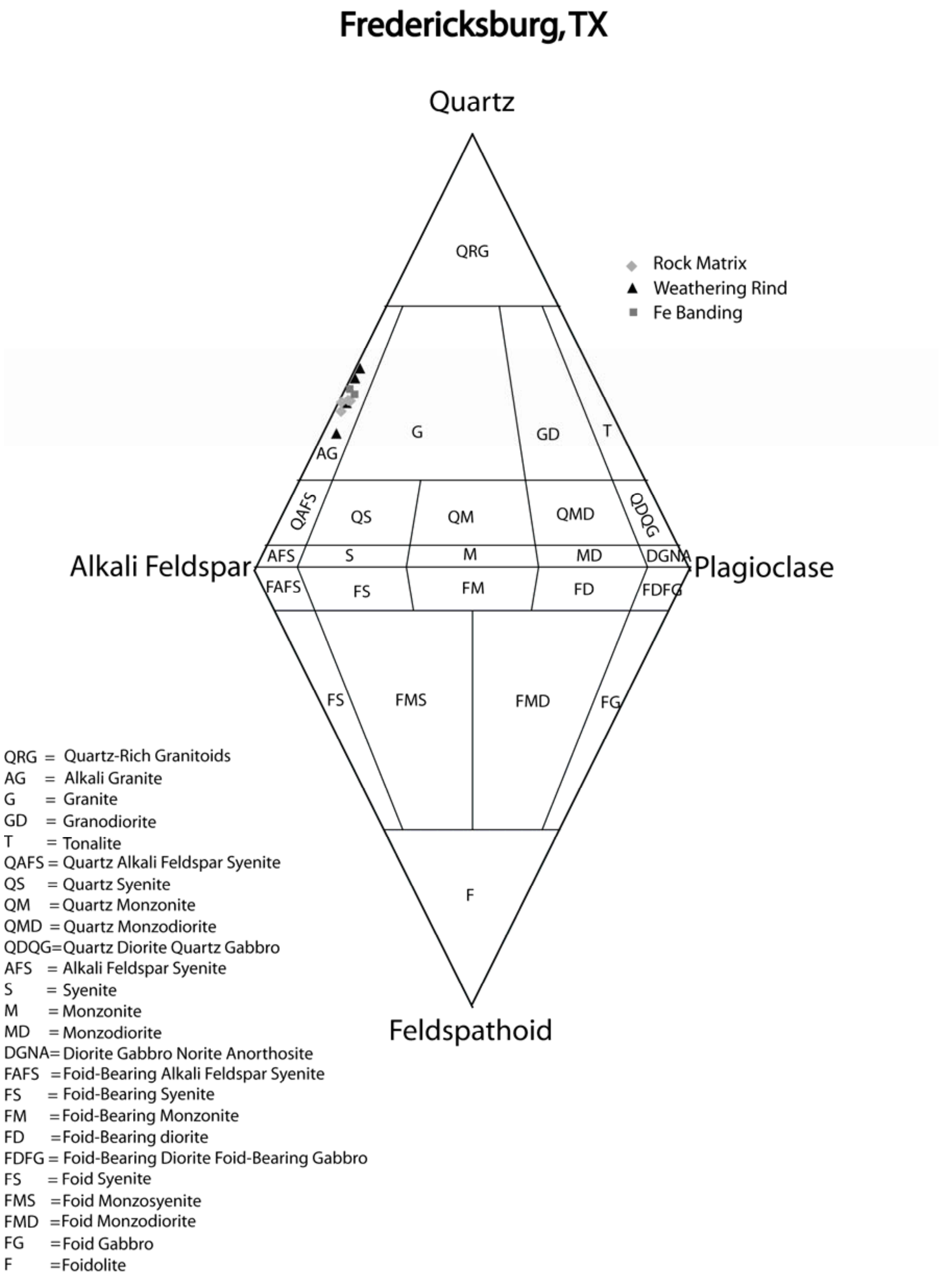

QRG = Quartz-Rich Granitoids
AG = Alkali Granite
G = Granite
GD = Granodiorite
T = Tonalite
QAFS = Quartz Alkali Feldspar Syenite
QS = Quartz Syenite
QM = Quartz Monzonite
QMD = Quartz Monzodiorite
QDQG = Quartz Diorite Quartz Gabbro
AFS = Alkali Feldspar Syenite
S = Syenite
M = Monzonite
MD = Monzodiorite
DGNA = Diorite Gabbro Norite Anorthosite
FAFS = Foid-Bearing Alkali Feldspar Syenite
FS = Foid-Bearing Syenite
FM = Foid-Bearing Monzonite
FD = Foid-Bearing diorite
FDFG = Foid-Bearing Diorite Foid-Bearing Gabbro
FS = Foid Syenite
FMS = Foid Monzosyenite
FMD = Foid Monzodiorite
FG = Foid Gabbro
F = Foidolite

Figure 2.11: IUGS Plot showing Town Mountain Granite rock matrix, iron banding, and weathering rinds.

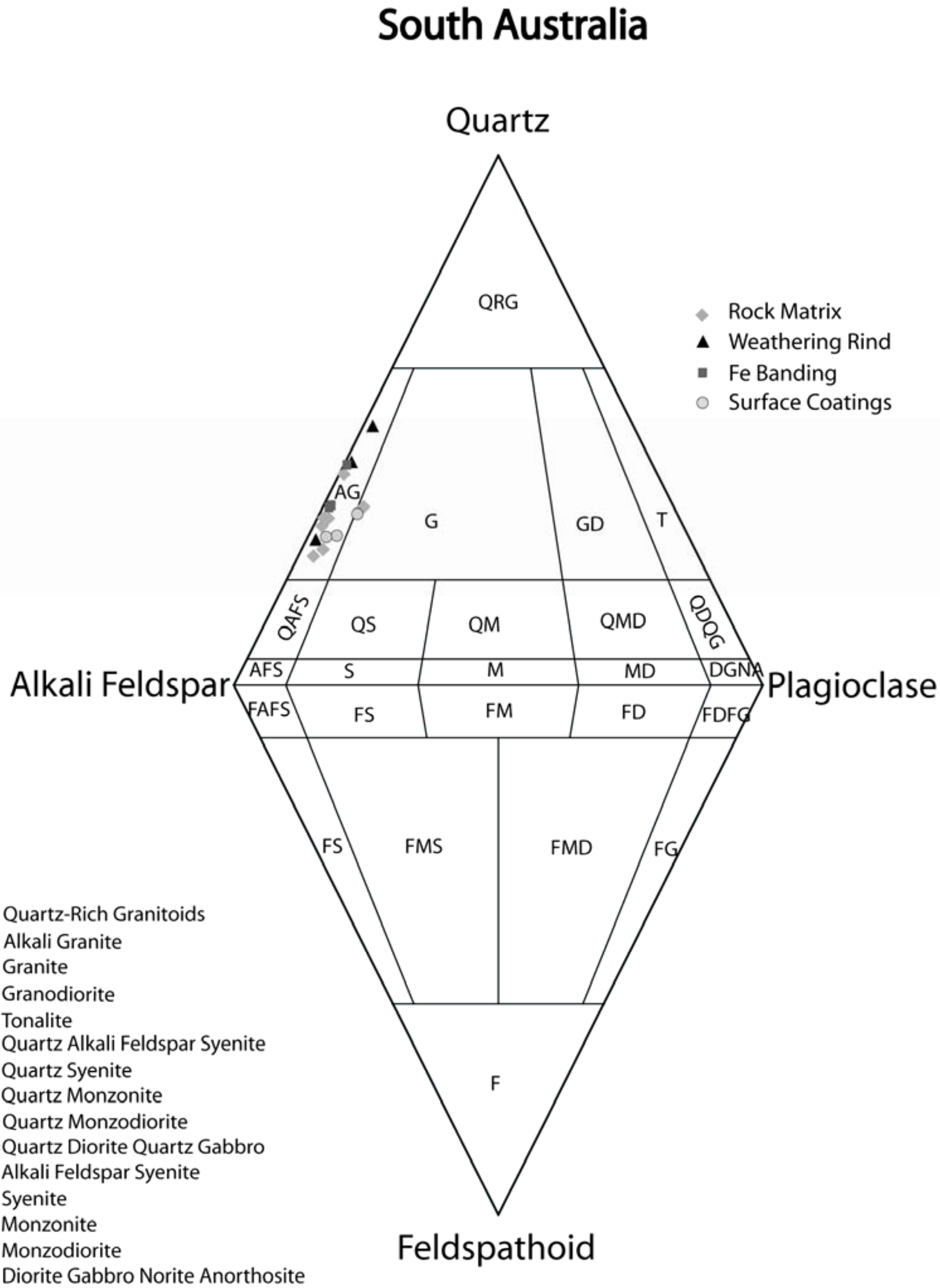

QRG = Quartz-Rich Granitoids
AG = Alkali Granite
G = Granite
GD = Granodiorite
T = Tonalite
QAFS = Quartz Alkali Feldspar Syenite
QS = Quartz Syenite
QM = Quartz Monzonite
QMD = Quartz Monzodiorite
QDQG=Quartz Diorite Quartz Gabbro
AFS = Alkali Feldspar Syenite
S = Syenite
M = Monzonite
MD = Monzodiorite
DGNA= Diorite Gabbro Norite Anorthosite
FAFS = Foid-Bearing Alkali Feldspar Syenite
FS = Foid-Bearing Syenite
FM = Foid-Bearing Monzonite
FD = Foid-Bearing diorite
FDFG = Foid-Bearing Diorite Foid-Bearing Gabbro
FS = Foid Syenite
FMS = Foid Monzosyenite
FMD = Foid Monzodiorite
FG = Foid Gabbro
F = Foidolite

Figure 2.12: IUGS Classification of Calca Granites and fracture alterations from South Australia.

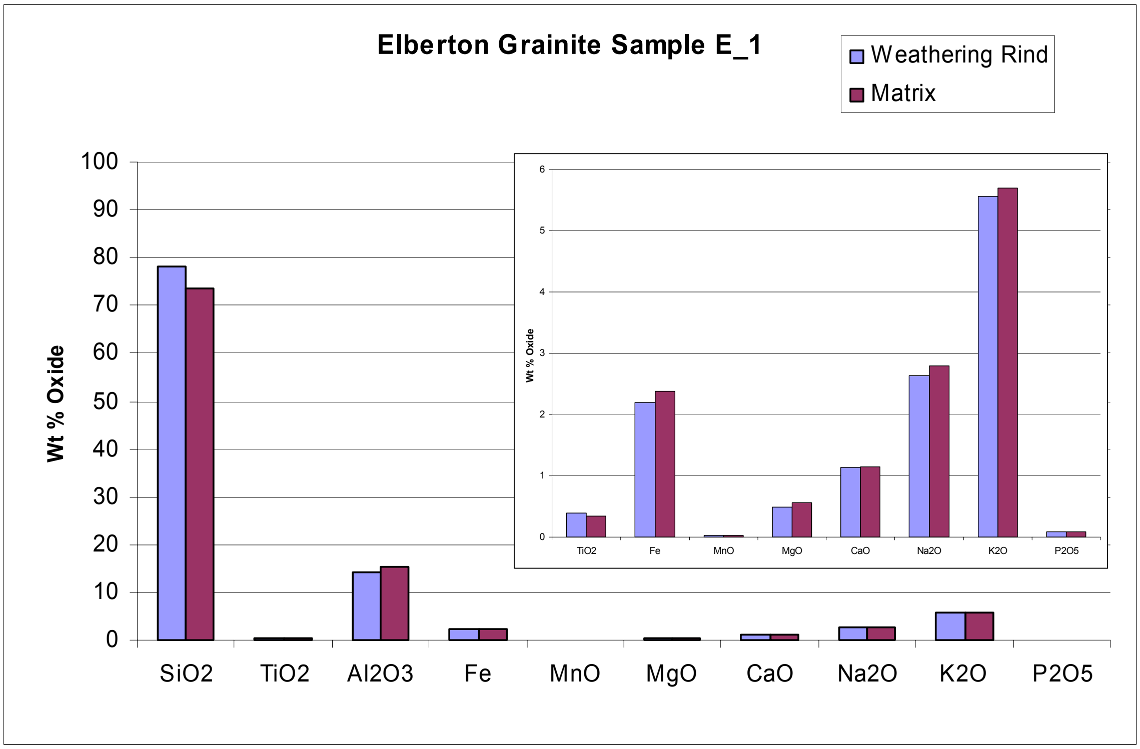

Figure 2.13: Bulk chemical analysis of rock matrix and fracture alteration.

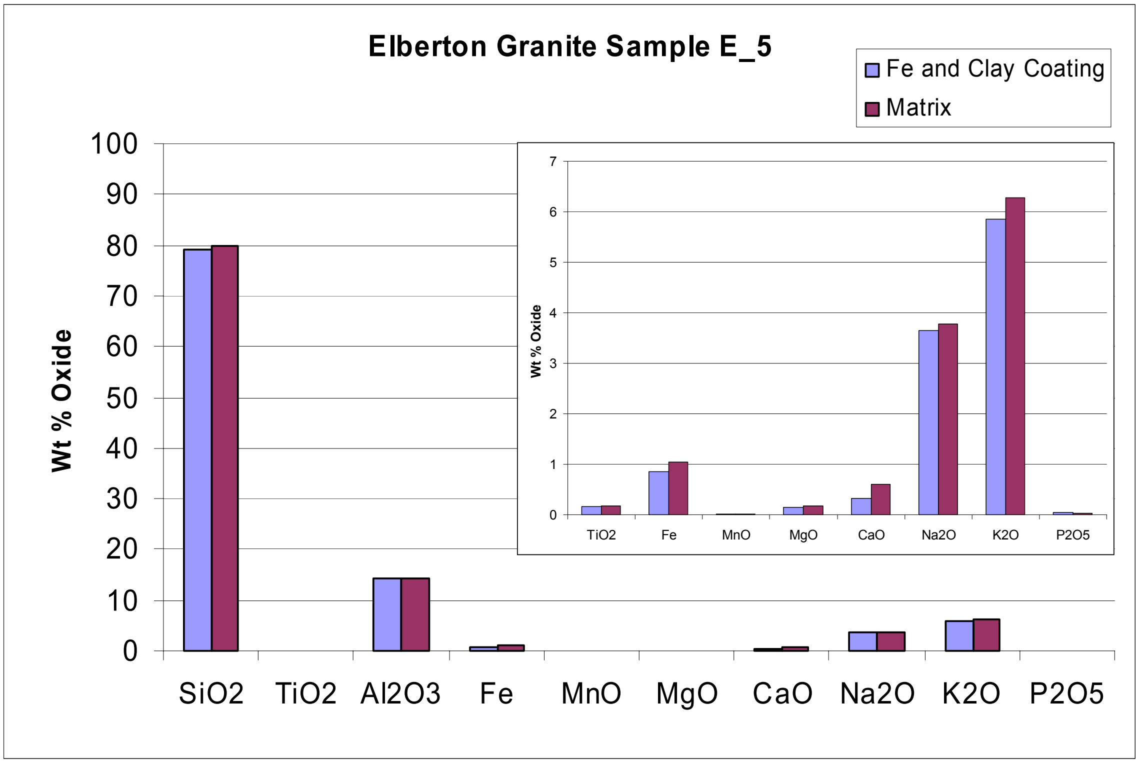

Figure 2.14: Bulk chemical analysis of rock matrix and fracture alteration.

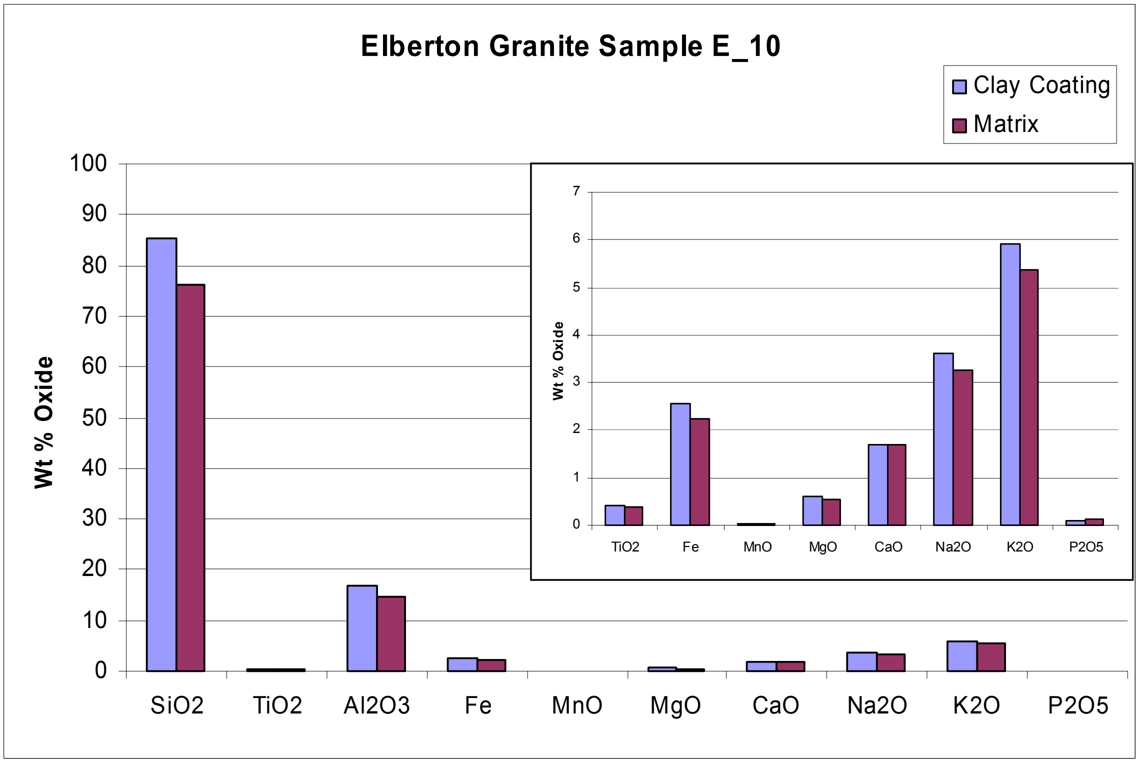

Figure 2.15: Bulk chemical analysis of rock matrix and fracture alteration.

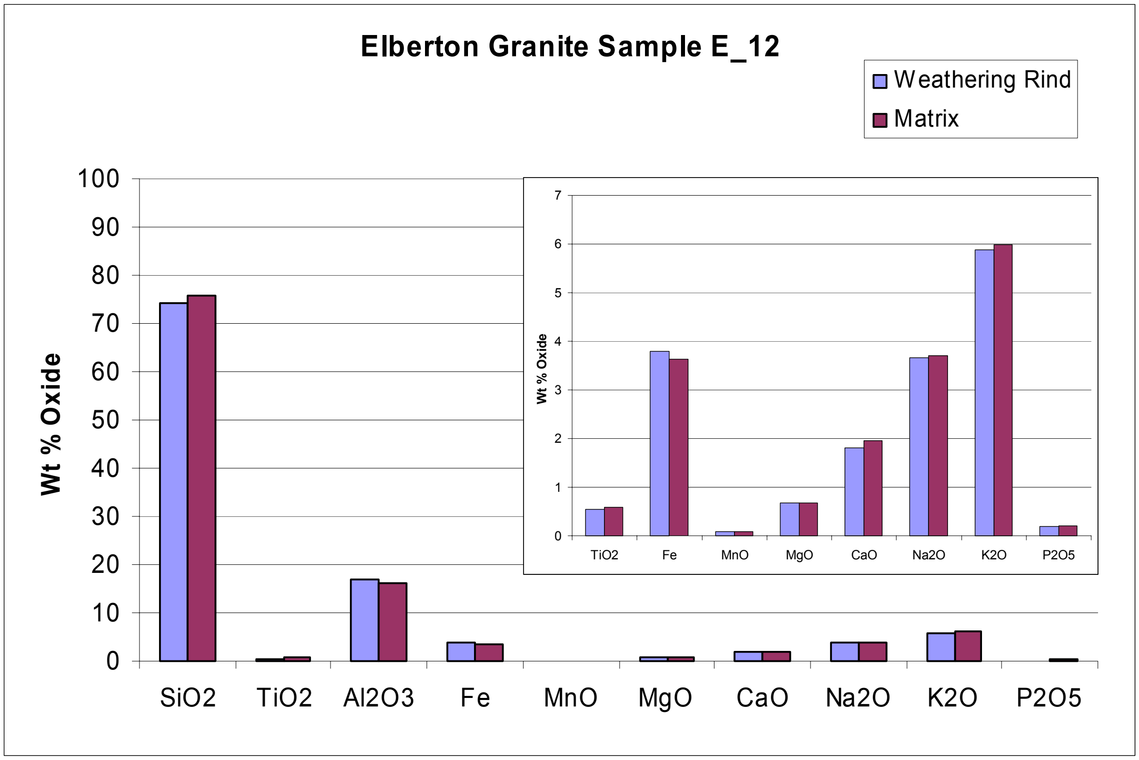

Figure 2.16: Bulk chemical analysis of rock matrix and fracture alteration.

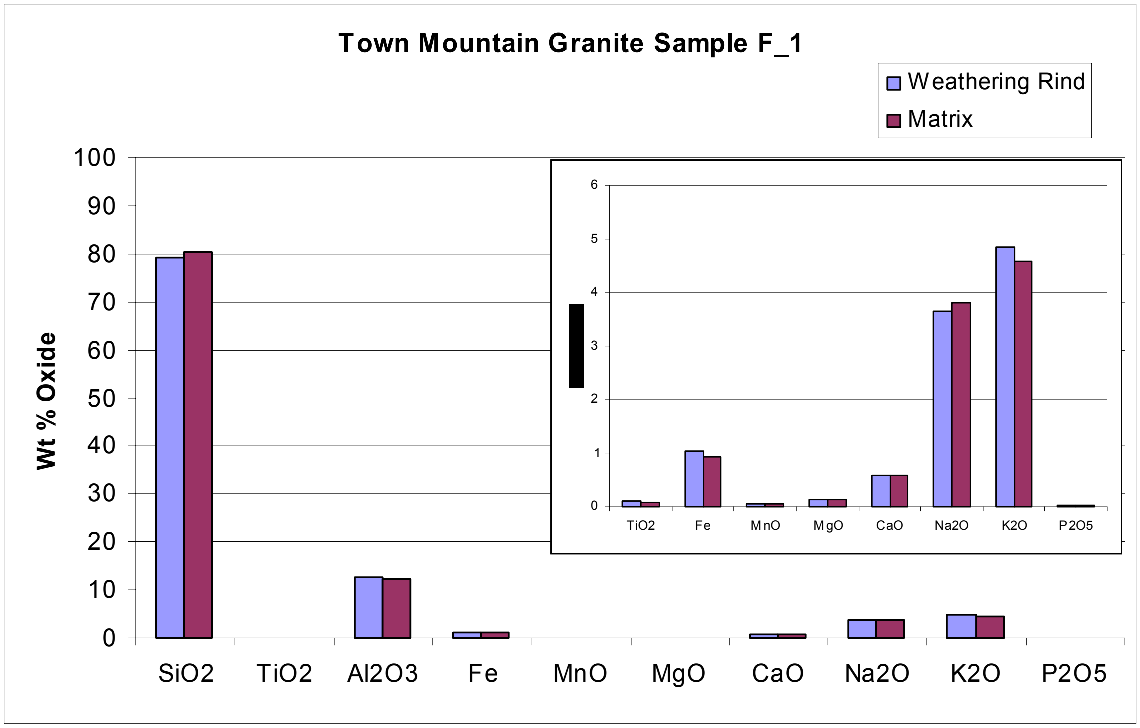

Figure 2.17: Bulk chemical analysis of rock matrix and fracture alteration.

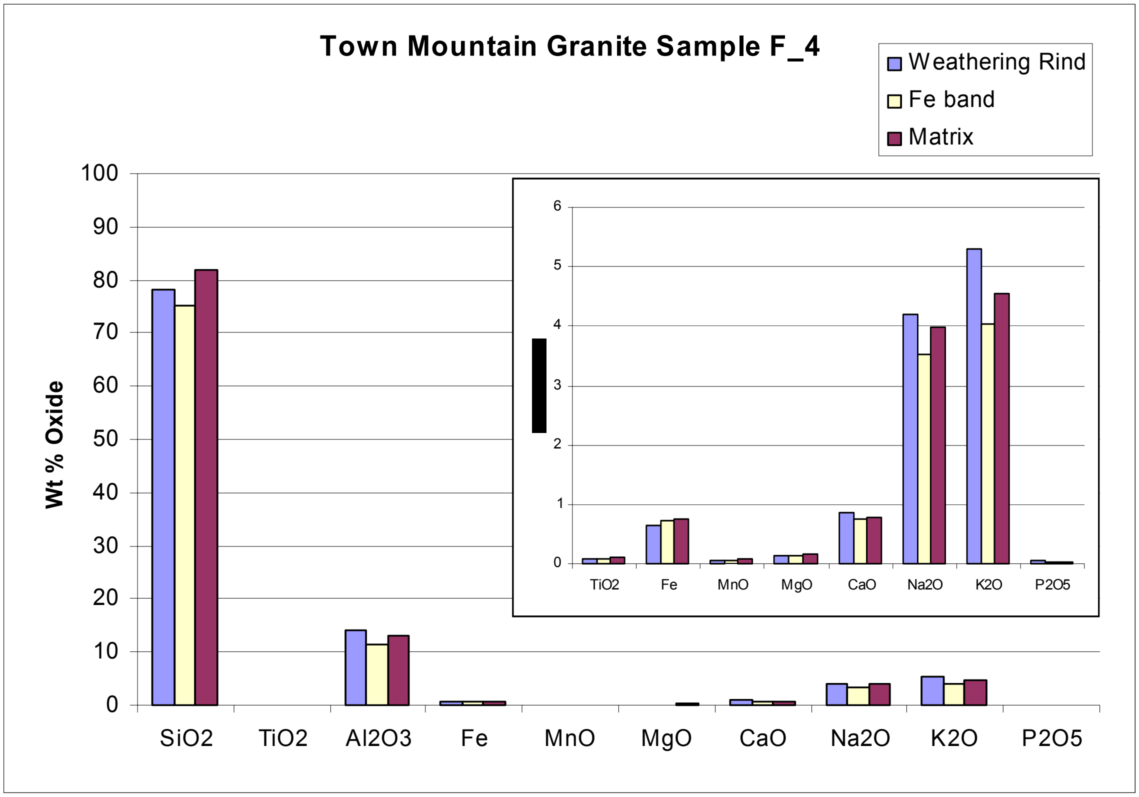

Figure 2.18: Bulk chemical analysis of rock matrix and fracture alteration.

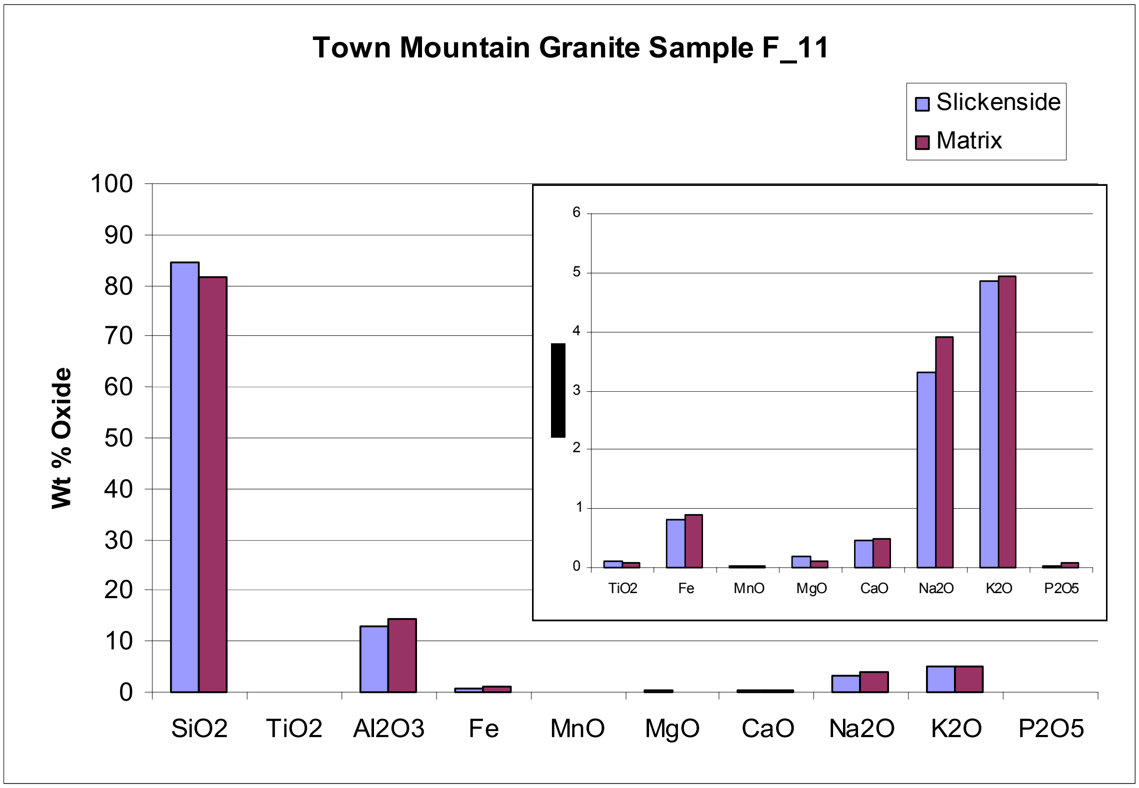

Figure 2.19: Bulk chemical analysis of rock matrix and fracture alteration.

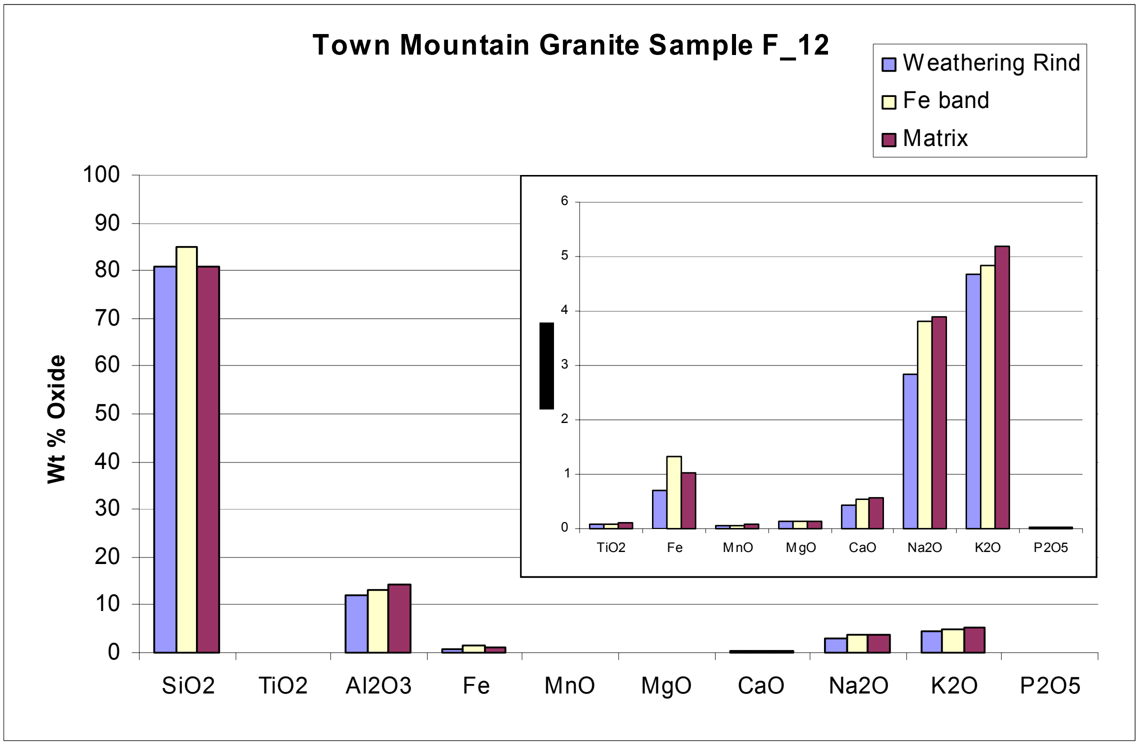

Figure 2.20: Bulk chemical analysis of rock matrix and fracture alteration.

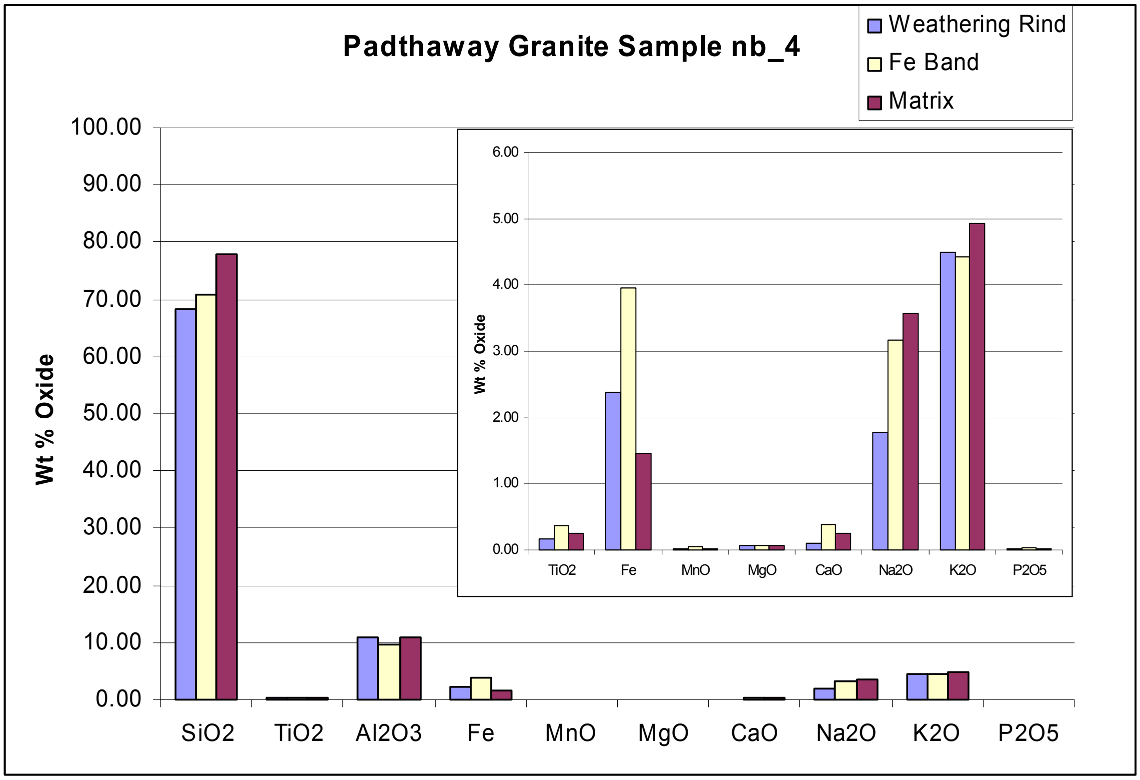

Figure 2.21: Bulk chemical analysis of rock matrix and fracture alteration.

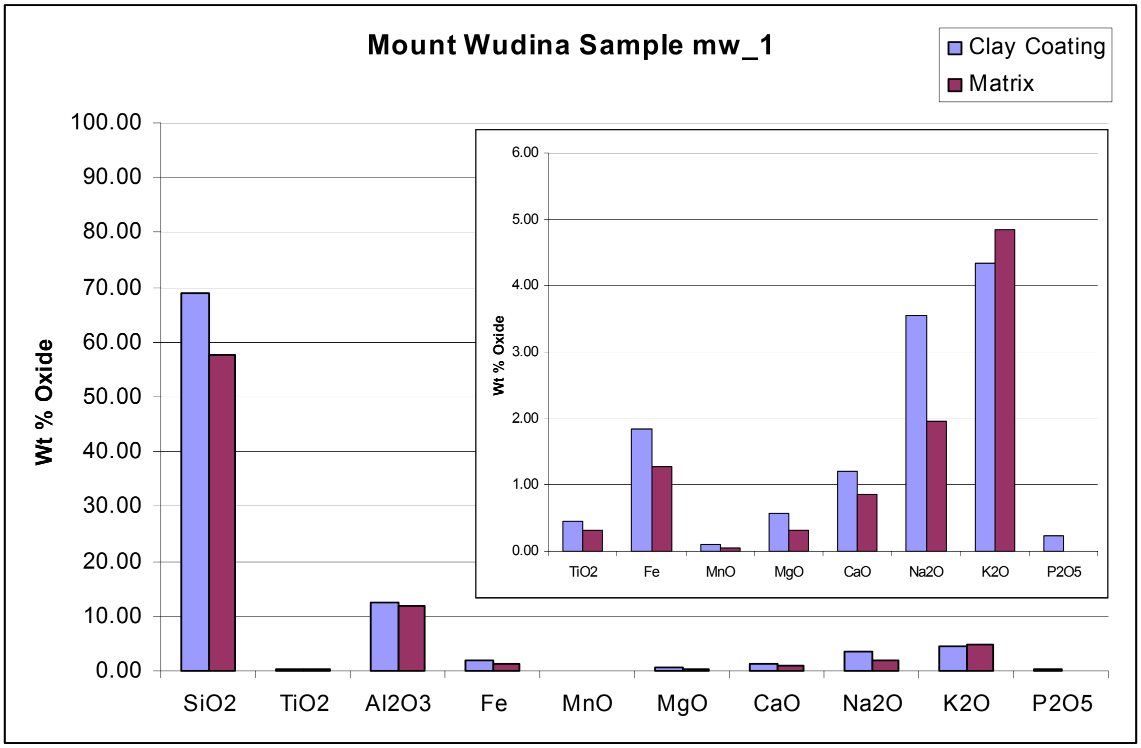

Figure 2.22: Bulk chemical analysis of rock matrix and fracture alteration.

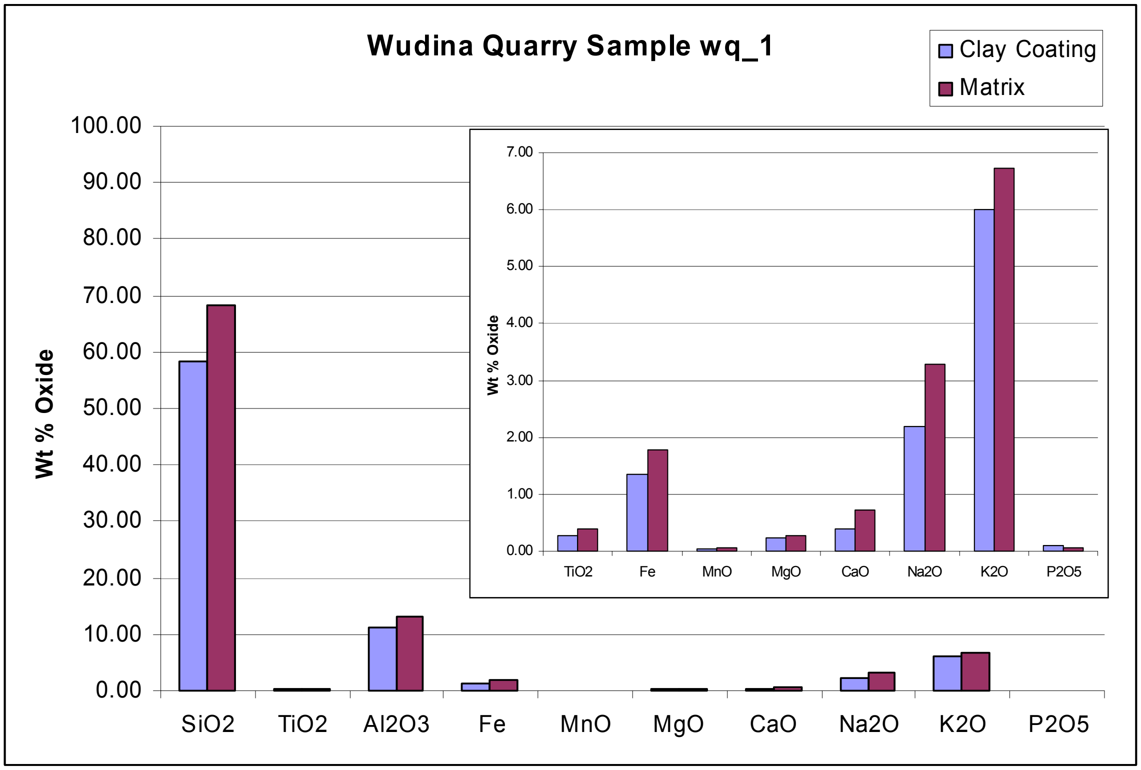

Figure 2.23: Bulk chemical analysis of rock matrix and fracture alteration.

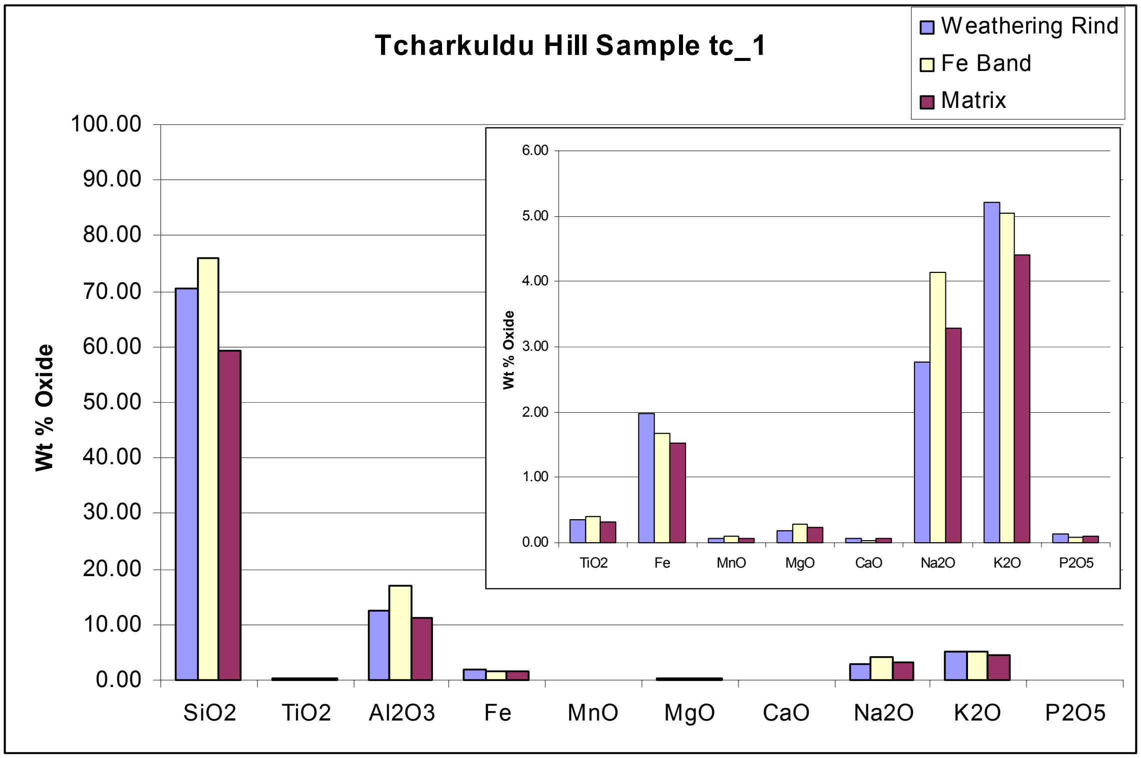

Figure 2.24: Bulk chemical analysis of rock matrix and fracture alteration.

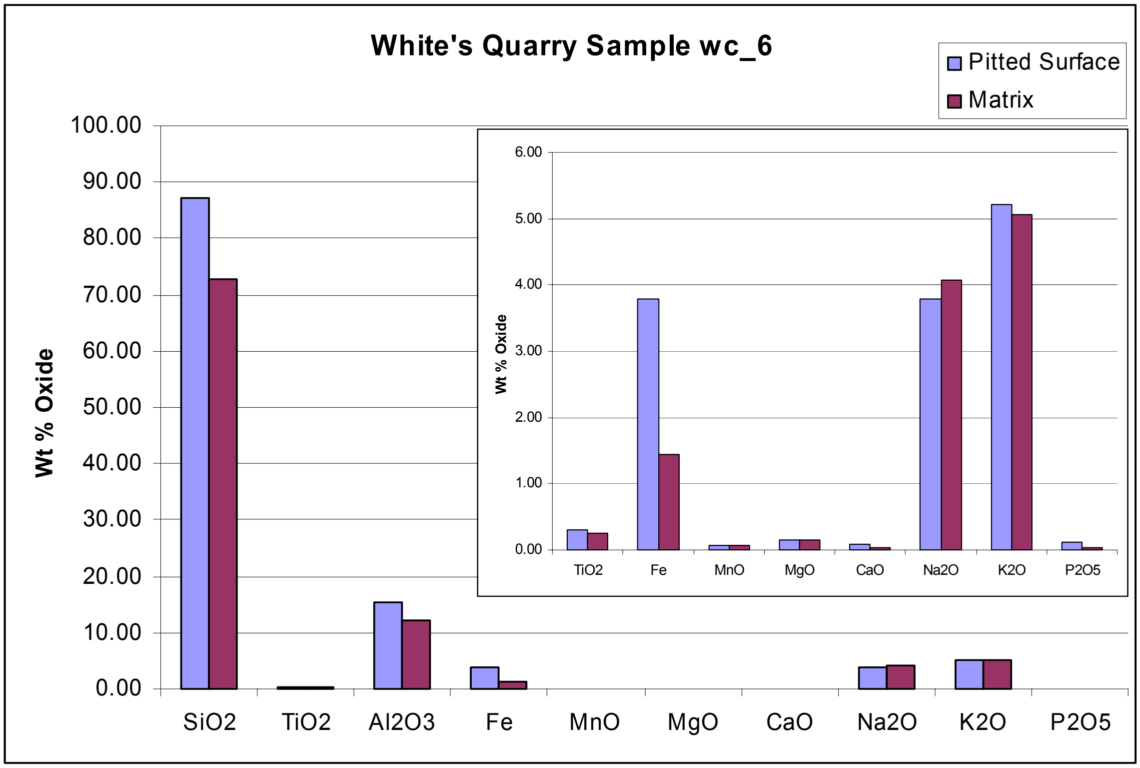

Figure 2.25: Bulk chemical analysis of rock matrix and fracture alteration.

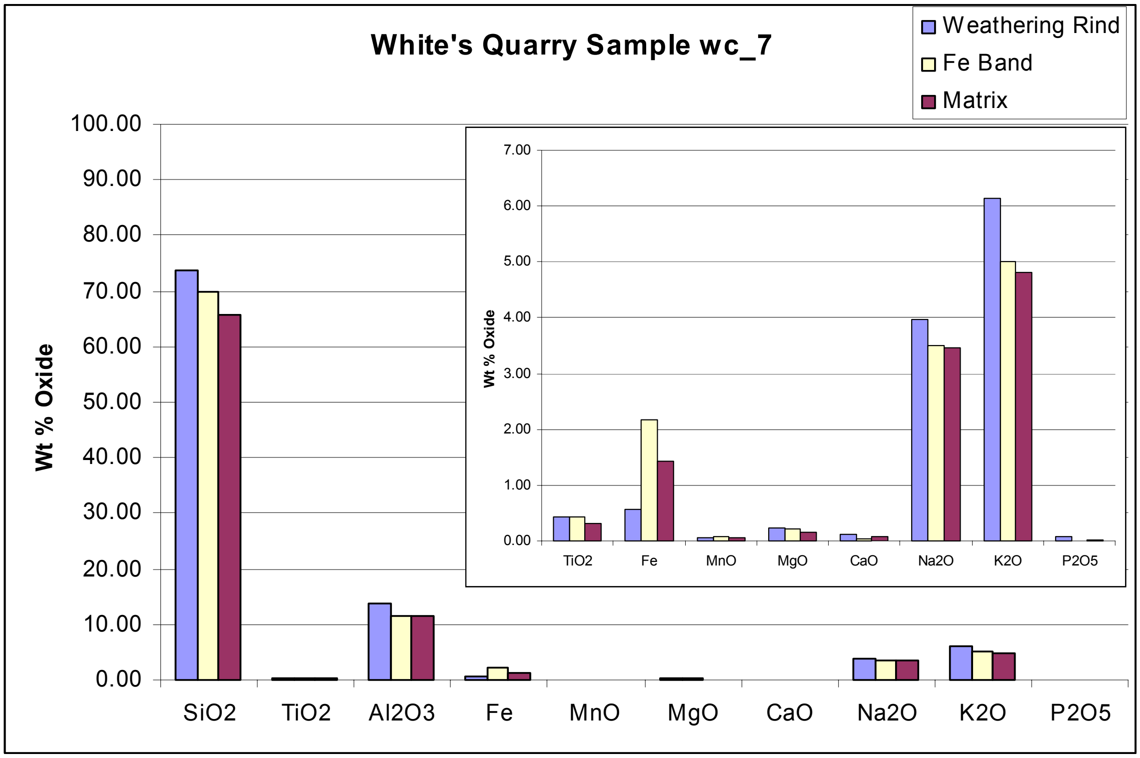

Figure 2.26: Bulk chemical analysis of rock matrix and fracture alteration.

Elberton Sample #	**Alteration Type**	**SiO2**	**TiO2**	**Al2O3**	**Fe**	**MnO**	**MgO**	**CaO**	**Na2O**	**K2O**	**P2O5**
E_1A	Matrix	73.60	0.34	15.21	2.38	0.03	0.56	1.15	2.79	5.69	0.09
E_1B	Weathering Rind	78.23	0.39	14.36	2.20	0.03	0.49	1.14	2.64	5.56	0.09
E_5A	Fe and Clay Coating	79.29	0.16	14.46	0.86	0.02	0.14	0.32	3.65	5.86	0.04
E_5B	Matrix	79.99	0.17	14.38	1.05	0.01	0.17	0.61	3.78	6.28	0.03
E_10A	Clay Coating	85.26	0.41	16.99	2.56	0.04	0.62	1.70	3.61	5.90	0.11
E_10B	Matrix	76.29	0.37	14.50	2.24	0.03	0.54	1.68	3.27	5.37	0.12
E_12A	Weathering Rind	74.39	0.55	16.79	3.79	0.09	0.68	1.81	3.66	5.88	0.19
E_12B	Matrix	75.88	0.59	16.17	3.63	0.09	0.68	1.95	3.71	5.99	0.20
Mean	Alteration	79.29	0.38	15.65	2.35	0.05	0.48	1.24	3.39	5.80	0.11
Mean	Matrix	76.44	0.37	15.07	2.33	0.04	0.49	1.35	3.39	5.83	0.11

Table 2.01: ICP analysis of rock matrix and fracture alteration samples from the Elberton Granite in Elberton Georgia.

Town Mountain Sample #	Alteration Type	SiO2	TiO2	Al2O3	Fe	MnO	MgO	CaO	Na2O	K2O	P2O5
F_1A	Weathering Rind	79.08	0.11	12.71	1.04	0.05	0.14	0.58	3.65	4.86	0.03
F_1B	Matrix	80.25	0.08	12.35	0.93	0.06	0.14	0.60	3.82	4.58	0.04
F_4A	Weathering Rind	78.09	0.08	14.05	0.65	0.05	0.14	0.87	4.19	5.30	0.05
F_4B	Fe band	75.27	0.07	11.53	0.72	0.05	0.13	0.74	3.52	4.03	0.03
F_4C	Matrix	81.91	0.11	12.94	0.75	0.07	0.17	0.78	3.98	4.54	0.03
F_11A	Slickenside	84.53	0.10	12.87	0.81	0.03	0.18	0.45	3.32	4.86	0.04
F_11B	Matrix	81.61	0.08	14.48	0.90	0.02	0.12	0.50	3.91	4.94	0.08
F_12A	Weathering Rind	80.77	0.07	12.15	0.69	0.06	0.13	0.42	2.84	4.67	0.04
F_12B	Fe band	85.02	0.09	13.26	1.33	0.05	0.13	0.55	3.81	4.83	0.03
F_12C	Matrix	80.82	0.12	14.35	1.04	0.07	0.13	0.56	3.89	5.20	0.04
Mean	Weathering Rind	80.62	0.09	12.95	0.80	0.05	0.15	0.58	3.50	4.92	0.04
Mean	Fe Band	80.15	0.08	12.40	1.03	0.05	0.13	0.65	3.67	4.43	0.03
Mean	Matrix	81.15	0.10	13.53	0.91	0.06	0.14	0.61	3.90	4.82	0.05

Table 2.02: ICP analysis of rock matrix and fracture alteration samples taken from the Town Mountain Granites in Fredericksburg Texas.

Calca Sample #	Alteration Type	SiO2	TiO2	Al2O3	Fe	MnO	MgO	CaO	Na2O	K2O	P2O5
Nb_4a	Weathering Rind	68.34	0.17	10.78	2.38	0.01	0.07	0.10	1.78	4.49	0.02
Nb_4b	Fe Band	70.80	0.37	9.57	3.95	0.05	0.07	0.39	3.16	4.42	0.03
Nb_4c	Matrix	77.93	0.24	10.89	1.45	0.02	0.07	0.25	3.57	4.93	0.01
MM_7a	Epidote Vein	60.59	0.20	12.49	3.01	0.08	0.26	0.57	2.66	5.47	0.03
MM_7b	Matrix	64.82	0.20	13.13	1.78	0.05	0.17	0.48	3.72	5.19	0.03
Mw_1a	Clay Coating	68.94	0.46	12.48	1.84	0.10	0.57	1.22	3.56	4.34	0.23
Mw_1b	Matrix	57.62	0.31	11.72	1.28	0.06	0.32	0.86	1.96	4.85	0.01
Tc_1a	Weathering Rind	70.59	0.34	12.52	1.97	0.07	0.18	0.07	2.77	5.21	0.14
Tc_1a	Fe Band	75.96	0.41	16.86	1.68	0.10	0.28	0.03	4.13	5.05	0.08
Tc_1a	Matrix	59.30	0.33	11.08	1.53	0.07	0.23	0.06	3.28	4.41	0.10
WC_3	Fracture Fill	67.45	0.28	12.86	1.45	0.01	0.96	0.40	2.58	3.69	0.05
WC_6ba	Pitted Weathering Rind	87.33	0.31	15.53	3.78	0.06	0.14	0.09	3.78	5.21	0.11
WC_6bb	Matrix	72.66	0.25	12.20	1.44	0.06	0.15	0.03	4.07	5.06	0.04
WC_7a	Weathering Rind	73.59	0.43	13.87	0.57	0.05	0.24	0.12	3.97	6.14	0.07
WC_7b	Fe Band	69.89	0.43	11.62	2.16	0.08	0.21	0.03	3.50	5.00	0.0
WC_7c	Matrix	65.57	0.32	11.44	1.44	0.05	0.15	0.08	3.45	4.81	0.01
WQ_1a	Clay Coating	58.18	0.27	11.33	1.34	0.04	0.24	0.39	2.19	6.00	0.09
WQ_1b	Matrix	68.29	0.38	13.29	1.77	0.06	0.28	0.73	3.28	6.73	0.06
Mean	Weathering Rind	74.96	0.31	13.17	2.18	0.05	0.16	0.09	3.08	5.26	0.09
Mean	Fe Band	72.21	0.40	12.68	2.60	0.08	0.19	0.15	3.60	4.82	0.03
Mean	Matrix	66.60	0.29	11.97	1.53	0.05	0.20	0.36	3.33	5.14	0.04
Mean	Surface Coatings	62.57	0.31	12.10	2.06	0.07	0.36	0.73	2.80	5.27	0.12

Table 2.03: ICP analyses of rock matrix and alteration zones from samples of Calca Granite from the Wudina and Minnipa region of South Australia.

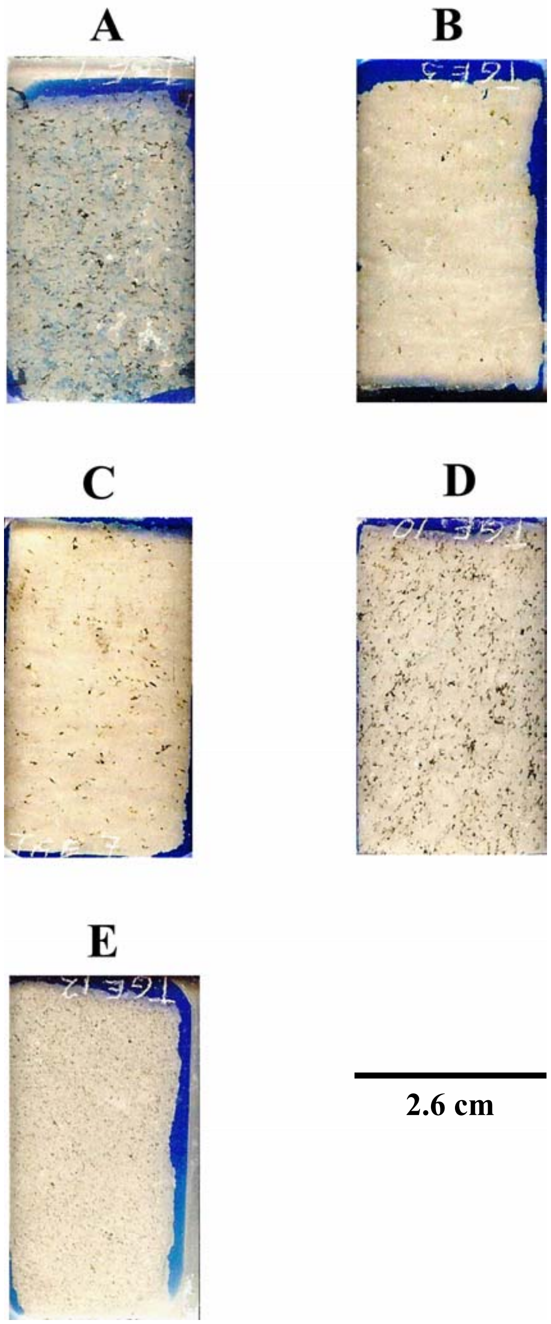

Figure 2.27: Thin sections of Elberton granites in cross-section scanned on a flatbed scanner. Tops of all slides represent fracture surface. Alterations include A) sample E_1 weathering rind (from remnant in soil horizon), B) sample E_5 iron and clay coated fracture surface, C) sample E_7 clay coating with organic wads, D) sample E_10 clay coated fracture surface, and E) sample E_12 very early weathering rind formation.

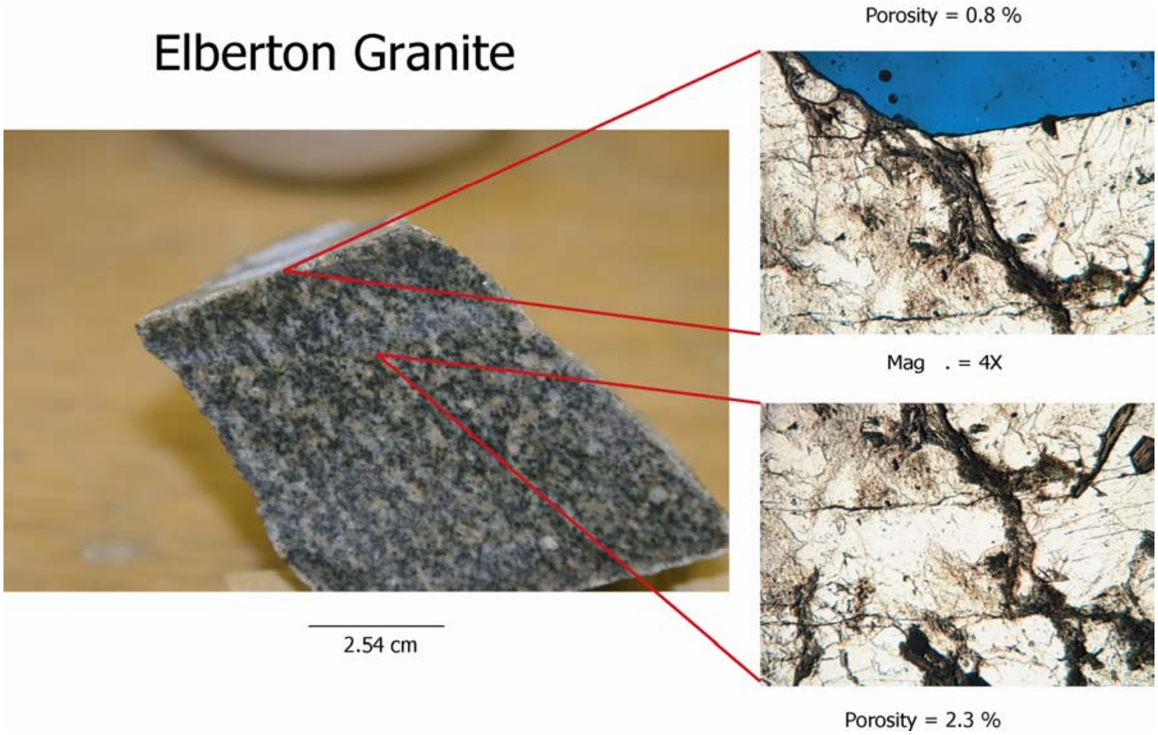

Figure 2.28: Picture of hand sample profile with clay coated top surface. Optical microscopy images show little distinguishable difference between clay coated surface and rock matrix.

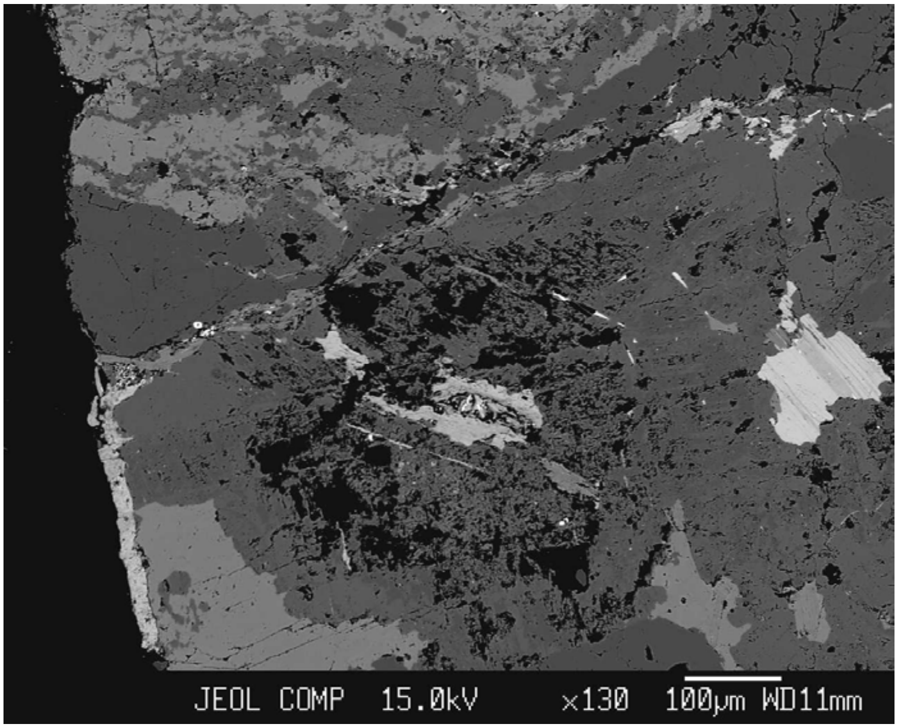

Figure 2.29: EPMA image of chlorite precipitation at microfracture in Elberton granite.

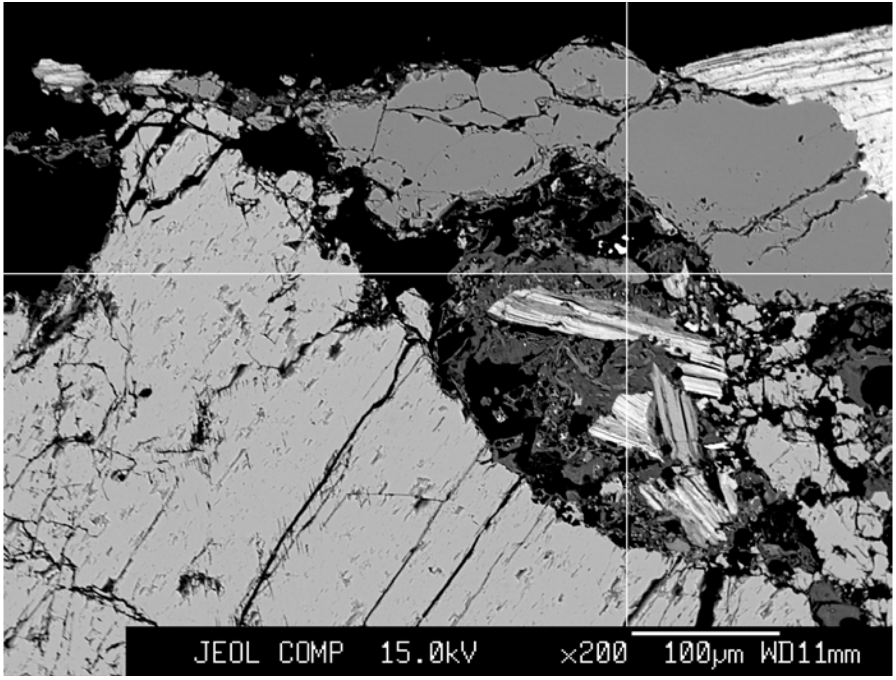

Figure 2.30: EPMA image of core softening in Elberton granite.

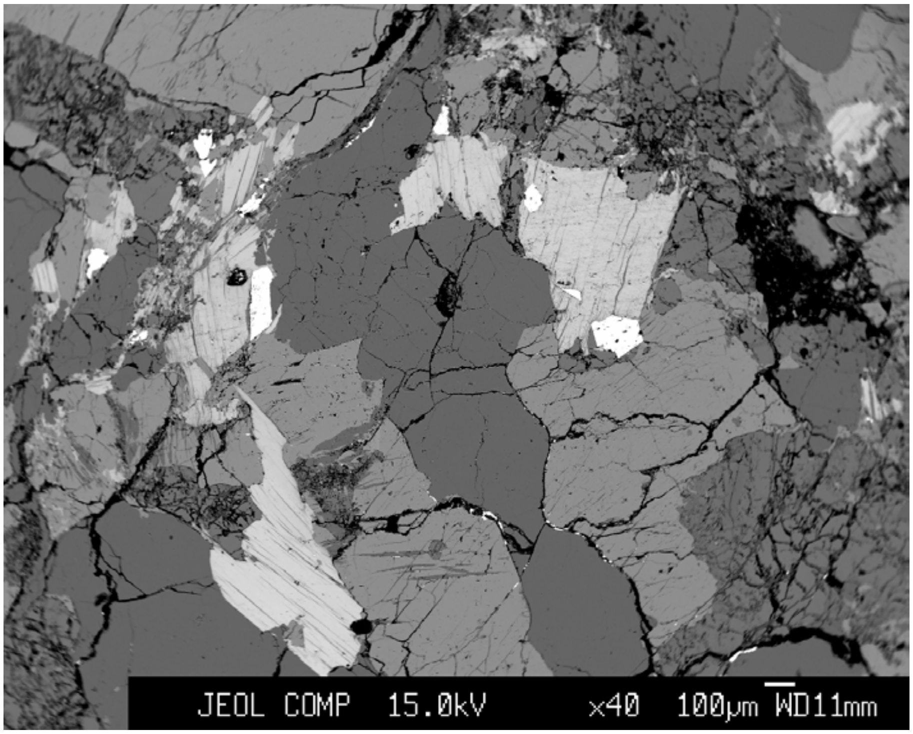

Figure 2.31: EPMA image of microfracture containing clay and hematite in Elberton granite.

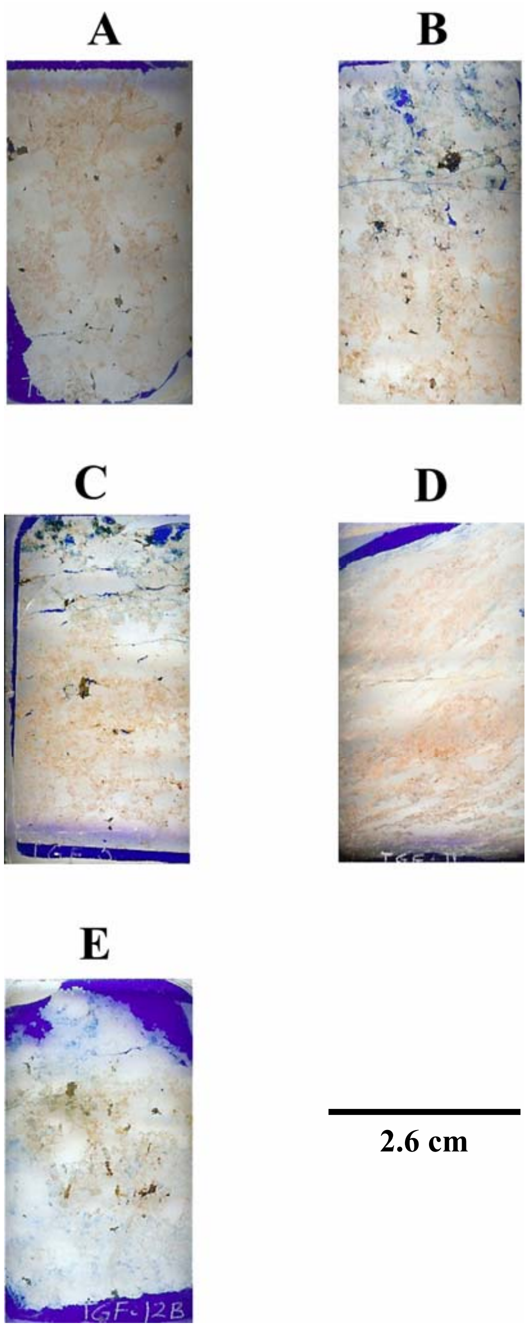

Figure 2.32: Thin sections of Town Mountain Granites in cross-section scanned on a flatbed scanner. Tops of all slides represent fracture surface. Alterations include A) sample F_1 weathering rind, B) sample F_4 weathering rind with iron banding, C) sample F_5 weathering rind with iron band, D) sample F_11 slickenside surface, and E) sample F_12 weathering rind with iron banding.

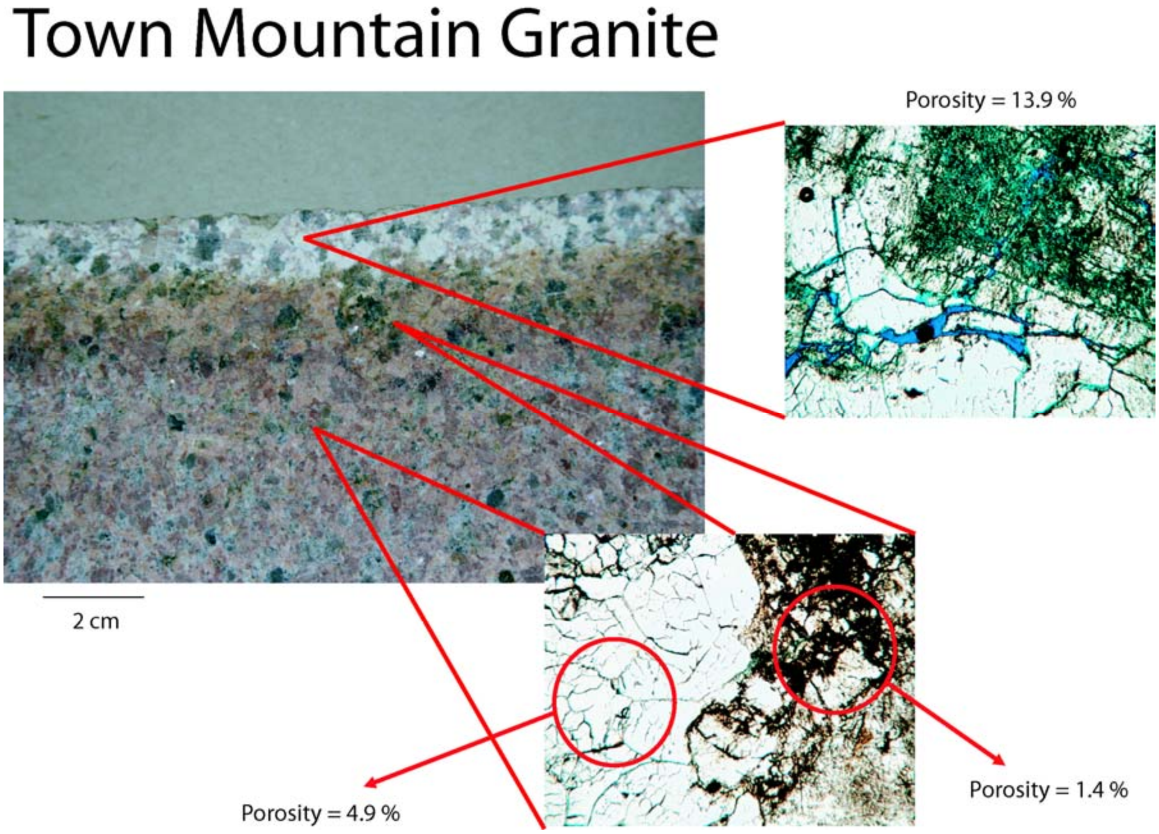

Figure 2.33: Town Mountain granite showing variation in insitu porosity using optical microscopy.

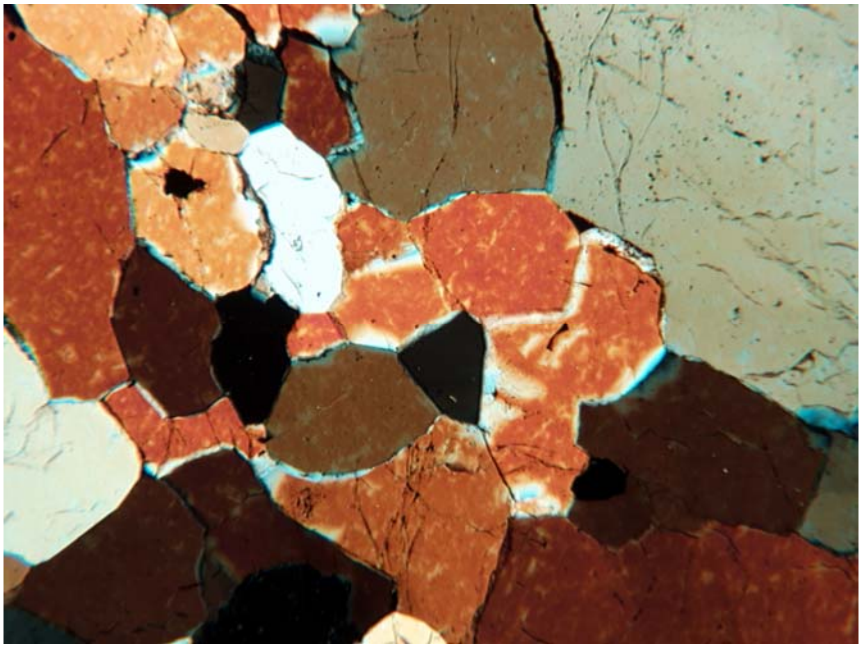

Figure 2.34: 2x magnification of rock matrix of Town Mountain Granite.

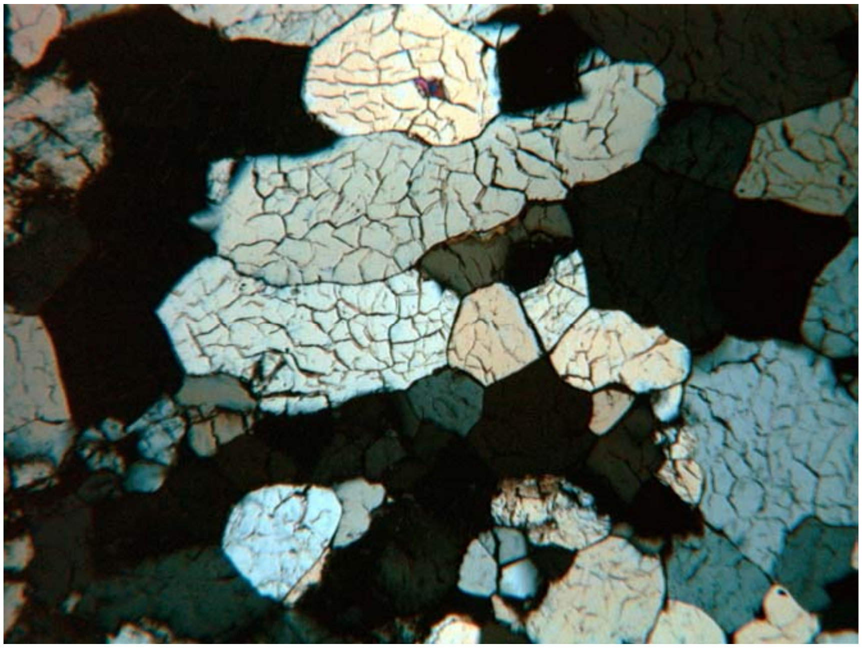

Figure 2.35: 5x magnification of fracture quartz crystals in the inferred rock matrix of a hand sample.

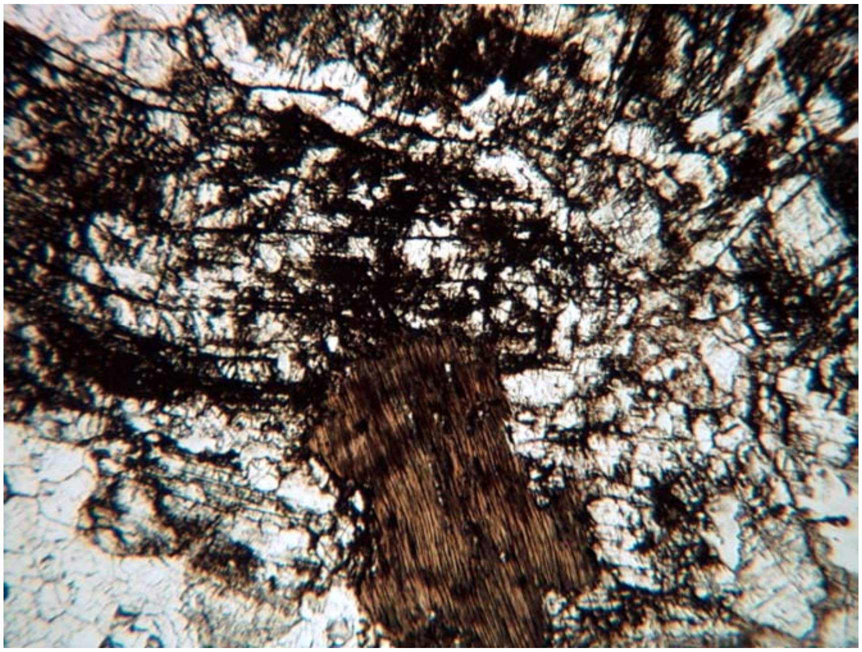

Figure 2.36: 2x magnification showing precipitation of amorphous iron and clay formation in micro-fractures and degrading plagioclase crystals.

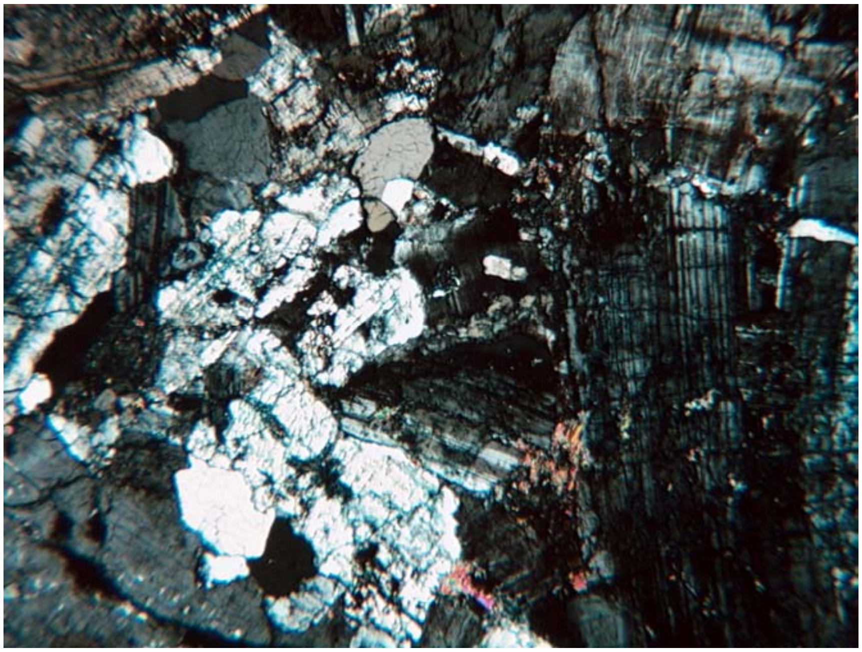

Figure 2.37: Clay formation is predominantly along plagioclase boundaries in the weathering rind. Magnification is 2x.

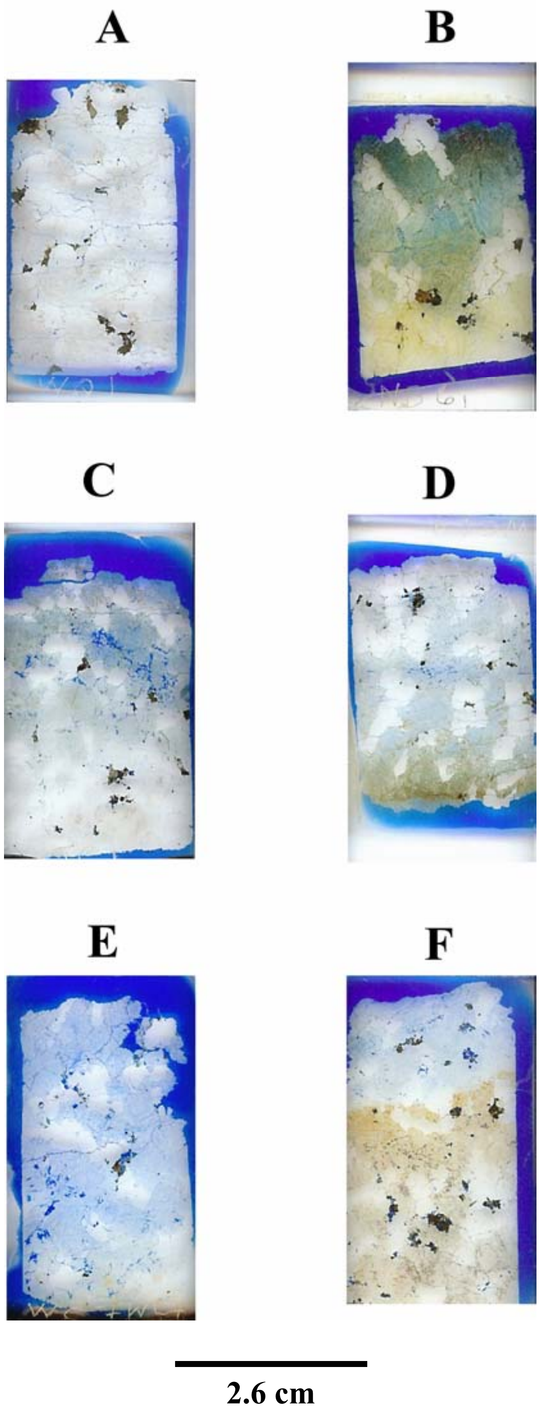

Figure 2.38: Thin sections of Calca Granites in cross-section scanned on a flatbed scanner. Tops of all slides represent fracture surface. Alterations include A) sample WQ_1 clay coated surface, B) sample NB_6 weathering rind with iron banding, C) sample TC_1 weathering rind with iron band, D) sample WC_6 pitted surface, E) sample WC_7 weathering rind with beginning of iron banded zone, and F) sample WC_5a weathering rind with thin iron band and matrix rock.

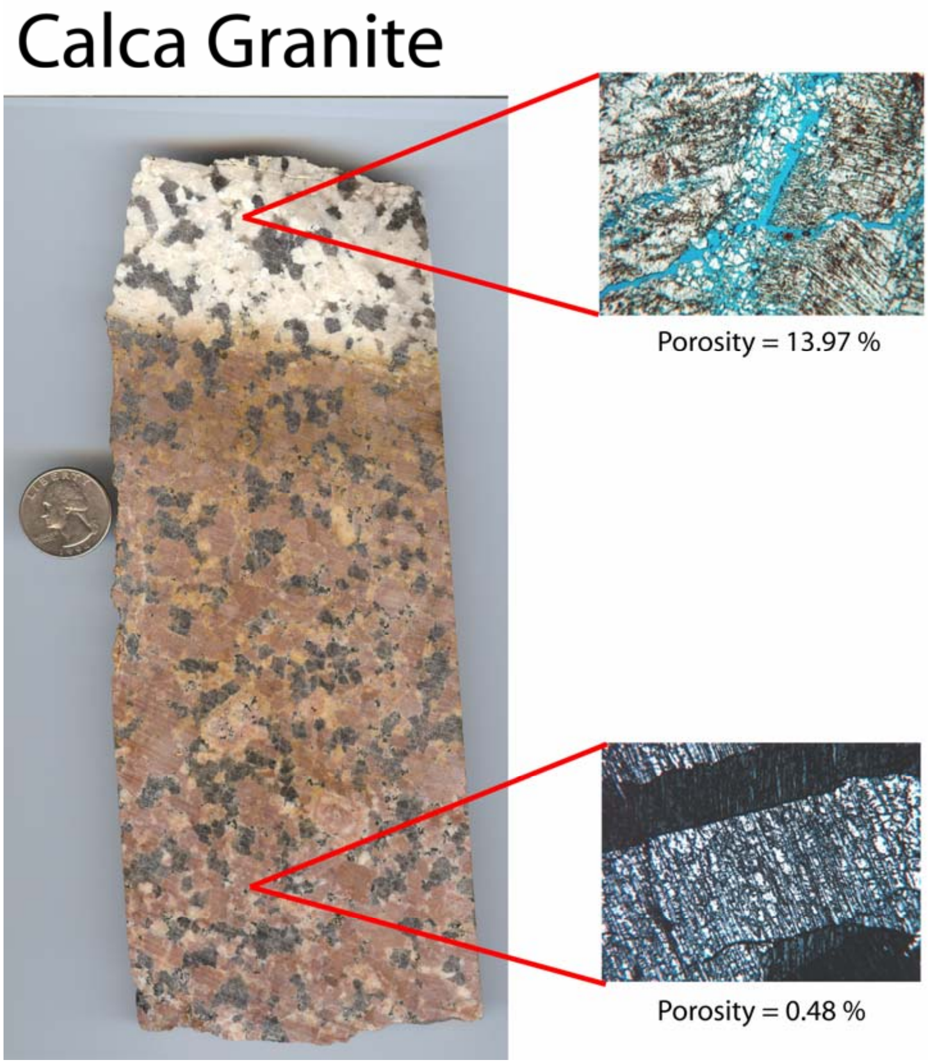

Figure 2.39: Calca granite with weathering rind and iron band. Optical images show variation in porosity.

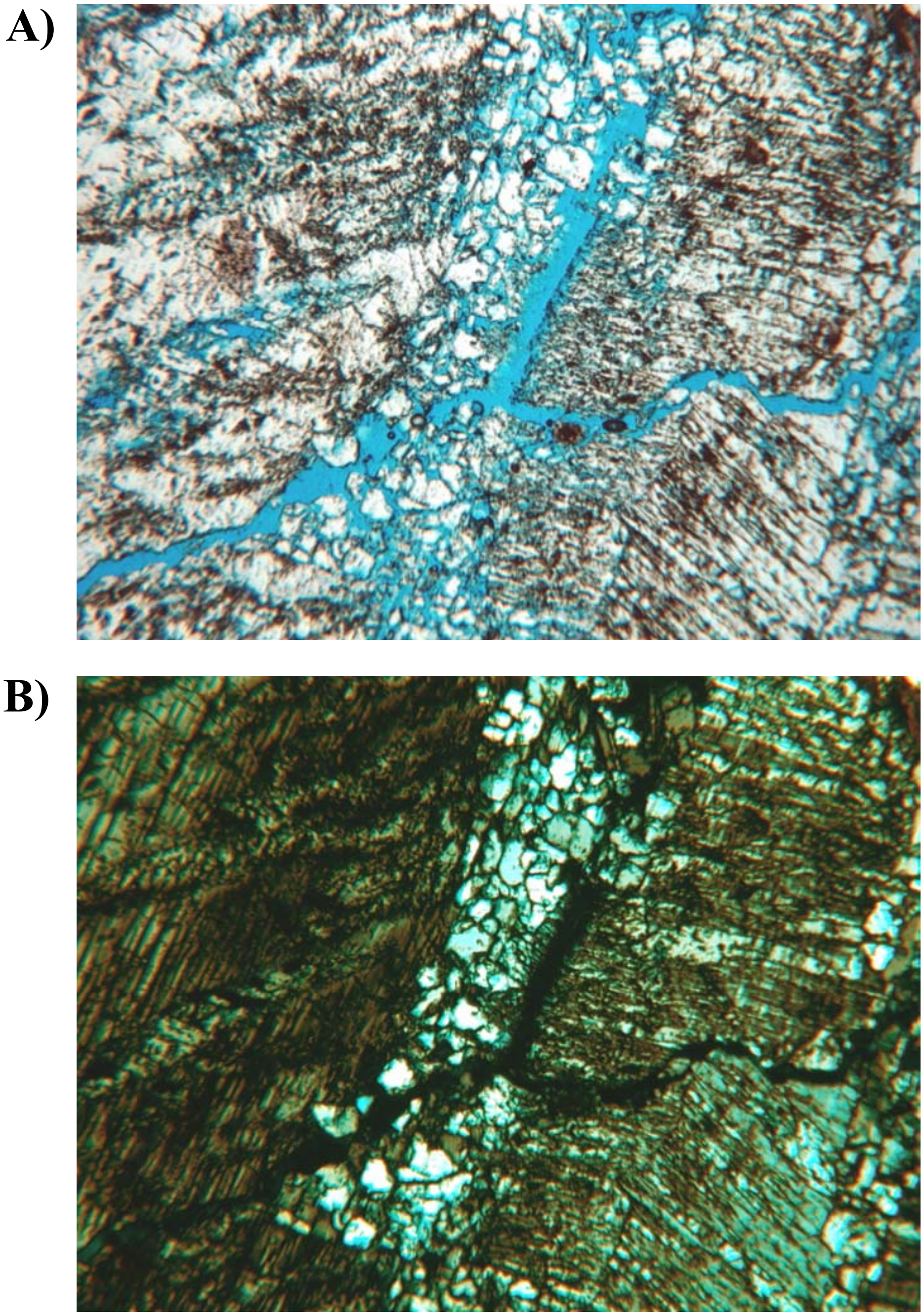

Figure 2.40: Image A shows perthite in the weathering rind of Calca granite in plain light at 5x magnification. Image B is the same image as A but shown in polarized light.

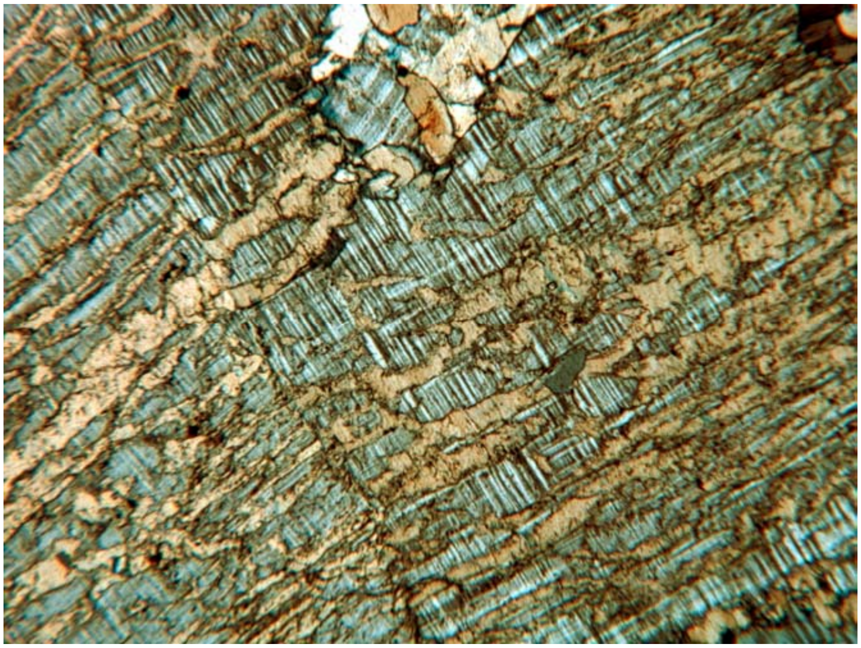

Figure 2.41: Unaltered alkali feldspar with lamella of plagioclase in Calca Granite. 5x magnification.

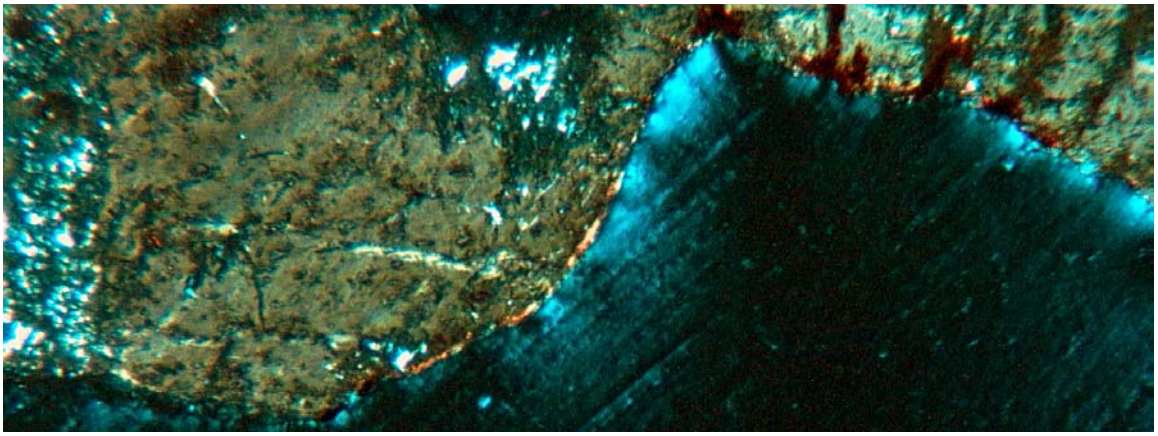

Figure 2.42: Gold to yellow at the edge of plagioclase crystals is clay forming coating along fracture edge. 10x magnification.

Chapter 3
Transport Properties

Granite is generally assumed to be a low porosity-low permeability crystalline rock. Twidale (1982) states primary porosity of unaltered granite is less than 1%. Twidale discusses secondary porosity of granite in the form of fractures, but neglects porosity variation caused by alteration around the fractures. In model prediction, matrix diffusion and sorption are treated as a homogeneous uniform constant with regards to the rock matrix surrounding the fracture. In this study, variation in granite transport properties in various fracture skin types and rock matrix are determined.

Porosity Measurements

Introduction

Porosity is commonly divided into primary and secondary porosity. Transport through fracture skins and rock matrix occurs through the grain to grain contacts and if present through micro-fractures. Thus, effective porosity is a function of both the primary and secondary porosity. Characterization of transport between the two types of porosity is of little use in granite.

Distinguishing between the larger pores and smaller dead-end pores is of significance for characterizing transport. It has been shown that even conservative tracers can be retained in the intergranular porosity within a sample primarily composed of sand and clay (Wood et al., 1990). For this reason porosity is sub-divided into macro-porosity, meso-porosity, and micro-porosity. Macro-porosity includes pores with diameters greater than 500 Å, meso-porosity includes pores with diameters ranging from 20 Å to 500 Å, and micro-porosity includes pores with diameters less than or equal to 20 Å. Macro and meso-porosity is measured by mercury injection porosimetry and micro-porosity is measured by the Brunauer, Emmett, and Teller (BET) method with argon (Ar) gas.

Macro-Porosity

Mercury injection porosimetry is used to determine the porosity of the fracture skins and rock matrices. Porosity measurements are made using a Micrometrics Autopore III Mercury Injection Porosimeter. Samples from Elberton, Fredericksburg, and South Australia are selected based upon skin types commonly observed at the field sites and the volume of samples available.

Samples are prepared by coring 2.54 cm cores from hand samples. South Australia (Calca Granite) samples with thick skins measured either fracture skin or rock matrix independently. Domestic granite samples measured porosity of skins and rock matrix combined. For samples consisting of multiple fracture skins, additional independent measurements are made in order to determine porosity of each skin type and the rock matrix.

Measured fracture skins from Elberton included clay and iron surface coating, infiltrated organic debris, and a remnant weathering rind. The weathering rind sample with a porosity of 8.17% is from the transition zone between the saprolite overburden and the outcropping granite. The highest porosity yielded is by the weathering rind. Table 3.01 shows Elberton skin types and porosities. The mean surface coating porosity is 1.81% and the granite matrix is 2.62%. No iron banding was found adjacent to fractures in the quarry. Elberton Granites display a core softening trend -- a lower porosity / permeability external layer over the higher porosity / permeability layer. The Georgia climate enhances the rate of weathering, but fracture skins are thin in comparison to Fredericksburg weathering rinds. Differences in porosity of ~0.5% occur in several samples between the fracture skin and the rock matrix. This enhances solute transport through these fracture-dominated flow systems.

The dominant skin type in Fredericksburg granite is an exterior weathering rind with an iron band forming a second fracture skin (Figure 3.01). Dendritic and massive pyrolusite is also common on fracture faces in the quarries (Figure 3.02). From the six samples analyzed four represented dual skin formation of weathering rind and iron precipitates (Table 3.02). The mean porosity for the weathering rinds is 8.0%, which is significantly higher than that of iron precipitate (1.66%) and matrix (2.4%). The arid climate of Texas and the lack of overburden contribute to a core hardening trend that would suggest attenuation of solute transport.

Also measured from Fredericksburg samples, are porosities from slickensides and pyrolusite coatings. The porosity of granite with slickensides is 3.5%, in comparison to the mean matrix measurement of 2.4%; this is a significant porosity increase. The increase in porosity for the granite with slickensides is due to the mineral recrystallization in the rock. During deformation, quartz crystals undergo subgrain rotation recrystallization (SR recrystallization) (Passchier and Trouw, 1996). SR recrystallization is the process of turning large crystals into smaller crystals. The cause of SR recrystallization is the mineral resistance to the release of energy and movement of a fault block. Increased porosity is caused by formation of small quartz crystals from large quartz crystals, or an increase in grain boundary density. The pyrolusite coatings are too thin to separate from the host rock and measure porosity. To determine the porosity, equation (3.1) was used to calculate skin porosity based on the total sample porosity and matrix porosity measured.

$$\phi_t V_t = \phi_s V_s + \phi_m V_m \tag{3.1}$$

Here ϕ_t is the total porosity, V_t is the total volume measured, ϕ_s is skin porosity, V_s is skin volume, ϕ_m is the matrix porosity, and V_m is the volume of the matrix.

Porosity measurements from the Calca granites show mean weathering rind porosity of 11.28%, mean surface coating porosity of 4.53%, mean iron band porosity of 2.33%, and rock matrix averages of 3.79% (Table 3.03). Surface coatings tend to have a higher porosity than the rock matrix, suggesting that the origin of the clay is from the weathering of the granite matrix and not detrital clay transported from overburden.

Comparing porosity measurements from different field sites show the South Australia samples have the highest measured porosity for rock matrix, iron bands, surface coatings, and weathering rinds. This is contributed to several factors including age of the rock 1477 ± 34 Ma, active compressional stress (Twidale, 1996), and enhanced deterioration caused by salts (Bradley et al., 1978). Porosity measurements from Elberton and Fredericksburg correlate well with each other. The differences between the two domestic sites are the presence of iron bands at Elberton and lack of clay coatings in Fredericksburg.

Weathering rinds provide a significant increase in porosity of the fracture skin in comparison with the rock matrix, where as iron coatings appear to have little impact on porosity. The influence of iron banding on porosity is significant if the iron banding is concentrated at the boundaries between iron band and weathering rind or iron band and rock matrix. Dispersed iron bands show similar porosity trends to weathering rinds (i.e., sample F_4 Table 3.02). In samples containing both weathering rinds and iron bands solute transport is expected to be attenuated due to the increased porosity of the weathering rinds. Samples with single surface coatings (i.e., pyrolusite) are expected to enhance solute transport because the outer coating decreases the effective porosity in contact with solute being transported through the fracture.

Rock samples from two sites in Padthaway, South Australia were collected. The first site is Mount Monster a rhyolite quarry and the second Padthaway an abandoned granite quarry, both are located southeast of Adelaide outside of Keith, South Australia.

Fracture skin formation from Mount Monster showed similar alteration parallel to the fracture as the granites from the Eyre Peninsula and Fredericksburg. Weathering rinds form at the fracture surface with an iron band underneath. Porosity measurements of the rhyolites show more extreme change in porosity than that of the granites (Table 3.04). Matrix porosity is higher than granite on average by 2 to 3 %, iron bands have lower porosity, and weathering rinds are significantly more porous (i.e. sample MM1, Table 3.04).

Padthaway quarry produces a medium- to coarse-grained green granite. Texture is similar to that of the granites from the Eyre Peninsula. Porosity measurements trend the same as that of Eyre Peninsula and Fredericksburg (samples NB6, Table 3.04) with high porosity in the weathering rind and the lowest porosity in the rock matrix.

Micro-Porosity

Micro-Porosity is measured using a Quantachrome Autosorb 1 injecting argon (Ar) gas. Samples are prepared by powdering the rock to pass a #200 sieve. This allows the measurement to only take into account inter-granular porosity and increase the amount of sample surface area available in a sample chamber. For best results it is suggested that no less than 1 m^2 of sample be used per run.

Measuring micro-porosity requires two separate measurements. The first is sample density by helium pycnometry and the second is the pore volume analysis using Ar injection. Both measurements are required to determine the micro-porosity by using the product of the density ($g\ cm^{-3}$) and the pore volume ($cm^3\ g^{-1}$).

Density is determined by injecting a measured pressure (~ 700 psi) of helium into the Autosorb manifold of volume $21.43 cm^3$ and releasing the helium into the sample chamber and measuring the pressure of helium in the chamber. Using the relationship

$P_1V_1=P_2V_2$ allows the volume of in the chamber to be determined. The sample chamber has a measured volume of 33.89 cm^3 and the difference between the volume of the chamber and the volume in the chamber with sample is the volume of the sample. Pre-measured mass of the sample and the volume of the sample allows for easy determination of sample density (Table 3.05).

Pore volume and pore size analysis was done using three different methods Dubinin-Radushkevich (DR), Horvath-Kawazoe (HK), and Saito-Foley (SF). Three methods are used for the initial set-up. The DR method assumes a Gaussian distribution of pore widths, the HK is independent of the Kelvin equation allowing the negation of capillary condensation and assumes slit-shaped pores, and the SF is the same as HK except that pores are assumed to be cylindrical in shape. Determining the pore size geometry is done using the hysteresis isotherm showing sorption and de-sorption of sorbate, hysteresis curve analysis follows characterization by de Boer (1958).

de Boer (1958) showed variation in the development of hysteresis curves, plotted as mass of adsorbed sorbate verses relative pressure, based on the geometry of the pore opening. There are five characteristic pore geometries: A) cylindrical; B) slit-shaped; C) wedge-shaped with one or two open ends; D) wedge-shaped with narrow necks; and E) “ink-bottle” pore shape. Pore shapes for the samples powdered to a sieve size #200 or less are dominated by cylindrical or slit-shaped pore geometry. From the hysteresis curves the extent of micro-porosity can also by predicted. For macro and meso-porosity hysteresis curves close before the relative pressure reaches 0.3, but they remain open when significant micro-porosity is present.

The hysteresis curves for skin and matrix of the Elberton Granites (Figure 3.03) indicates pore space is slit-shaped. Results from the helium pycnometry measurements show a decrease in density of clay coating relative to the rock matrix (Table 3.05). Density change from rock matrix to clay coating in Elberton is a decrease of 12 %. The overall micro-porosity is small relative to the meso-porosity measured by mercury injection. Micro-porosity measurement of clay coating (0.138%) is greater than the rock matrix (0.121%). Significant attenuation in the fracture would not be expected as a result of the increased micro-porosity in the clay coating. The increased available micro-porosity in the clay coating would retard mass being transported through the fracture, but when the sample is not disaggregated transport into the clay is impeded making intergranular porosity unavailable for surface reactions. Wood et al. (1990) showed micro-porosity would show retardation of conservative tracers in a sand aquifer. As the surface area of the micro-porous fractured material approaches the surface area of Wood's sand aquifer the micro-porosity becomes more important.

Rock matrix and combined alteration of weathering rind and iron band from the Town Mountain Granite both show slit-shaped pore spaces by method of hysteresis (Figure 3.04). Density change (Table 3.05) from skin to rock matrix represents a decrease of ~18%. The Town Mountain Granite matrix (0.126%) is slightly more porous than the Elberton Granite matrix (0.121%). In comparing meso-porosity from the two locations, the Town Mountain Granite is less porous. The difference could be cleavage from larger feldspar crystals in the Town Mountain Granite. Micro-porosity of the thin weathering rind and iron band increases to 0.147% from 0.126% in the rock matrix.

Fresh granite being sampled near the surface suggests increased intergranular porosity is caused from weathering of ferromagnesian minerals and feldspars. The idea of stress release increasing intergranular porosity by the order seen in the samples would be plausible if samples were collected from an area under stress (i.e., from depth).

Hysteresis curves are shown for a weathering rind, iron band (Figure 3.05), and the rock matrix (Figure 3.05) for the Calca Granite from White's Quarry. The curves all indicate slit-shaped pores with variation in separation of adsorption and desorption isotherms and magnitudes in volume. Granular density and micro-porosity are shown in Table 3.05. The smallest density (2.35 $g^{1}cm^{-3}$) is in the iron band with the middle density being the weathering rind (2.47 $g^{1}cm^{-3}$) and the largest being the rock matrix (2.74 $g^{1}cm^{-3}$). Micro-porosity is the lowest in the weathering rind (0.126 %) the rock matrix being the middle porosity (0.14 %) and the most porous grains compose of the iron banded section of the sample (0.176%).

With the trend in density and micro-porosity, a hypothetical model of skin formation could be the iron banded section as the zone of reaction with clay as a bi-product being transported by diffusion through the weathering rind. If transport through the weathering rind is slower than that of the iron banded zone then build-up of clay would increase the density and micro-porosity. In terms of potential effect on transport, mass back diffusing from the iron banded zone into the fracture would be impeded by the slow transport through the weathering rind. This would attenuate remediation efforts of a spill and make tracer test results appear retarded for both reactive and conservative constituents.

Retardation

Introduction and Background

Retardation coefficients R are used extensively in modeling transport and fate of contaminants. Retardation is defined by Jenne, 1998 as $R = V_W/V_M$, where V_W is the velocity of groundwater and V_M is the velocity of the solute or colloid of interest. Differences in groundwater and tracer velocities can be characterized as a function of tracer sorbed to the available surface area within a fracture. The term sorption incorporates both adsorption and absorption. In the case of short term tracer tests and small scale contaminant spills, sorption is primarily adsorption (attraction of metal to a rock surface) with limited absorption (incorporation of metal into the structure of rock forming minerals).

Determining retardation is done numerically using the distribution coefficient (K_d), bulk density (ρ_b), and porosity (ϕ) of the material of interest. The problematic component in determining retardation is the distribution coefficient. Distribution coefficient is the measure of solute sorbed to the mineral or rock in question or how much tracer is retained in the fracture caused by adsorption. Measuring retardation coefficients (R_d) is done by batch reaction (ASTM 4319, 1993).

The ASTM 4319 method describes a short-term batch reaction that allows a known concentration of solution to react with the rock. As explained by Jenne (1998), determining (K_d) by batch experiments are rarely taken to equilibrium. The K_d term by definition is a reaction in equilibrium. Retardation coefficients (R_d) where introduced as a response to criticisms to work done by Wahlberg and Fishman (1962), Baker et al. (1964), and Wahlberg et al. (1965) at the Nevada Test Site for the U.S. Atomic Energy Commission. R_d assumes that reactions approach equilibrium with insignificant effect when used numerically. In this study, the distribution coefficient is used and assumed to be equivalent to the retardation coefficient.

Methodology

The retardation factor R of the tracer in a porous media is determined by measuring the distribution coefficient K_d (L^3/M), porosity ϕ (-), and bulk density ρ_b (M/L^3) of the material. The relationship is expressed as:

$$R = 1 + \frac{\rho_b K_d}{\phi} \tag{3.2}$$

Bulk density is calculated simultaneously with porosity measurements from mercury injection porosimetry. K_d is calculated from the isotherm data determined by batch experiments using ICP-MS to measure solution concentrations.

Retardation of solutes transported by diffusion into the rock matrix is described as a surface reaction that is a function of the available specific surface area. The equation

$$\langle R \rangle = 1 + \langle a \rangle K_a \tag{3.3}$$

is given by Wels et al., (1996) where <a> specific surface area, K_a is the surface distribution coefficient, and <R> is retardation factor as a function of surface area. Determination of <a> is done using $A_{s,\ Hg}\ \rho_b/\phi$, the properties surface area ($A_{s,\ Hg}$), ρ_b, and ϕ are measured using mercury injection porisemetry. Properties are determined using mercury injection because the pore structure is lost in sample preparation for BET. Batch experiments are used to determine K_D from disaggregated samples and the surface area ($A_{s,\ BET}$) is measured using BET. Normalizing K_D with the surface area from BET gives the term K_a.

An alternative view of looking at the determination of surface area available for the given geometry of a plug sample is to assume porosity is available in the form of microfractures and cleavage planes. Conceptually, both microfractures and cleavage planes can be approached as a fracture network and can be explained by an equivocal parallel plate model at a small REV. In this scenario, K_a remains the same, but <a> simplifies to 2 times the inverse of the fracture aperture (b) assuming a smooth continuous fracture (Wels et al., 1996 and Wels and Smith, 1994).

$$R = 1 + \frac{2}{b} K_a \, . \tag{3.4}$$

Aperture is assumed equivalent to the average pore throat diameter given by mercury injection measurements.

Modifying ASTM standard 4319 by decreasing the rock mass used to 2 grams and the volume of solution to 10 ml allows limited rock sample to be used and a rock to solution ratio of 5 g ml $^{-1}$ is maintained. Granites are crushed to pass a 200 sieve that has a mesh size of 75 micrometers. In order to create an isotherm three concentrations (10, 1, and 0.1 ppb CsCl) are used to evaluate change in mass adsorbed verses change in equilibrium concentration. Solution concentrations are sampled at 3, 7, and 17 days to determine if reactions are approaching equilibrium.

Models and methods for determining distribution coefficients are numerous (Freundlich 1909, Langmuir, 1918, 1981, 1997, van Bemmelen, 1878, 1888, Vandergraff et al., 1993, Wahlberg et al., 1965). For the purpose of modeling transport of solutes it is common to use the simplest solution. The four most commonly used models are the Langmuir

$$Q = \frac{Q_{mb} C_e}{1 + bC_e}; \tag{3.5}$$

BET

$$Q = \frac{Q_{mc} C_e}{(C_s - C_e)\left[1 + (C - 1)\left(C_e / C_s\right)\right]}; \tag{3.6}$$

Freundlich

$$Q = KC_e^{1/n}; \text{ and} \tag{3.7}$$

linear relationship

$$Q = KC_e. \tag{3.8}$$

Q is the adsorbed concentration normalized to particle concentration (mg Kg^{-1}), C_e is solution concentration (mg L^{-1}), K is the distribution coefficient (ml g^{-1}), n is a constant,

C_s is the sorbate concentration, Q_{mb} and Q_{mC} represents their respective distribution coefficients at low concentrations, b is the distribution coefficient as a function of vacant sites, and C is the BET constant. The linear relationship between the concentration in solution and the concentration adsorbed is the simplest. In the batch experiments low initial concentrations (0.1, 1, and 10 ppb) are used to locate the results of the test at the initial portion of the sorption isotherm. To illustrate the linear portion of a Langmuir curve, a dashed box shown in Figure 3.07. In this region, at low relative concentrations all the presented models are approximately linear.

Batch experiment data can be expressed in one of two ways, the first is the ratio volume of solution used to mass of media used (ml g^{-1}) or the second is the ratio volume of solution to the surface area available for adsorption (m^2 g^{-1}). In this study surface area is estimated with the BET method injecting argon gas. By normalizing K_d to surface area, grain size does not need to be evaluated. An additional benefit of BET is that micro-porosity can be evaluated. This is important for solute transport because solute diffuses into micro-pores retarding transport and also cause back-diffusion (Wood et al., 1990). This makes conservative tracer test results mimic characteristics of reactive tracers and leads to overestimates of transport properties (dispersion, retardation, and matrix diffusion).

Experimental Results

The batch experiment is to determine how much reactive tracer sorbs to the granite rock matrix and fracture skins. Allowing reactions to reach complete equilibrium is unnecessary if the reaction is demonstrated to approach equilibrium (Jenne, 1998). To determine if the batch experiments approached equilibrium, each media is reacted for 3, 7 and 17 days (Figures 3.08, 3.09, and 3.10). By plotting solution concentration (C_e) verses reaction time, all reactions approached equilibrium at 17 days. The C_e plots approaches the difference of initial concentration and sorption capacity of the rock in a negative log fashion. By using the minimum of three points at 17 days, it is assumed that equilibrium has been approached to a point of diminishing return.

Adsorption data are analyzed by plotting the adsorption isotherm and curve matching models to determine an appropriate distribution coefficient. The data plotted represent rock matrix samples for Elberton, Town Mountain, and Calca Granites. Alteration samples include clay coating of Elberton Grantie, combined weathering rind and iron banding of Town Mountain Granite, and individual weathering rind and iron banding of the Calca Granite.

The adsorption isotherms for the batch reactions all approach linearity (Figures 3.11, 3.12, and 3.13). By modeling the slope of each set of data, the distribution coefficient in units of milliliter of solution per gram of rock is determined. Normalizing K_D to the available surface area gives K_a. K_a for the rock matrix for Elberton, Town Mountain, and Calca Granites are 4.21×10^{-6} m, 4.16×10^{-6} m, and 5.16×10^{-6} m (Table 3.07). Fracture skins for the three granites are clay coatings for Elberton ($K_a = 3.87 \times 10^{-6}$ m), combined weathering rind and iron band for Town Mountain ($K_a = 2.94 \times 10^{-6}$ m), and separated iron band ($K_a = 3.42 \times 10^{-6}$ m) and weathering rind for Calca ($K_a = 5.59 \times 10^{-6}$ m).

The retardation factors for the rock and alteration samples increases from 17 in the rock matrix to 32 in the clay coating for Elberton Granites. The Town Mountain Granites show virtually no change in R between the rock matrix (R = 8) and fracture skin (R = 7). Calca Granites show a decreasing trend from 170 in the matrix to 10 in the iron band to 4 in the weathering rind.

The two factors with the greatest change from rock matrix to fracture skin are porosity and composition. Porosity appears to have the greatest effect on R. For example, the Town Mountain Granites show no change in R and the difference in porosity is between the rock matrix (4.9%) and fracture skin (5.8%) is about 1%. For the Calca Granites the porosity of the fracture skin increases relative to the rock matrix, R decreases. The Elberton Granites show a decrease in porosity in the skin and R increases as a result. Thus, change in porosity from rock matrix to fracture skin has the greatest influence on R.

Treating the available porosity as a fracture network, R is calculated using equation 3.4. The data shown in Table 3.07 shows a similar trend of changing R for Elberton Granites and Calca Granites in the fracture skins relative to the rock matrix with overall lower values as when treated as porous media. Town Mountain Granites show a decrease in R from matrix to skin by a factor of 3. This change in trend is a result of the mean pore throat diameter for the rock matrix being significantly smaller. Similar to the porous media assumption, R is influenced most by the pore throat diameter.

Diffusion Coefficients

Abstract

Laser Ablation Inductively Coupled Plasma Mass Spectroscopy (LA-ICP-MS) is used to measure diffusion of cesium chloride into granite and fracture skin samples. The effective diffusion coefficients for cesium (Cs) are 9×10^{-11} m^2 sec^{-1} in the rock matrix of Elberton Granite and 1.75×10^{-11} m^2 sec^{-1} in the clay coating fracture skin. Granite samples where collected near surface; the diffusion coefficients are about two orders of magnitude greater than previously published data. In weathering rind and iron banded altered samples from the Calca Granite (South Australia) the diffusion coefficients are estimated at 3.8×10^{-11} m^2 s^{-1} and 1.9×10^{-12} m^2 s^{-1}, respectively. In two dimensions, spikes of tracer can be followed along grain boundaries and microfractures showing preferential diffusion pathways. Layers of weathering rind and iron banding show higher concentrations of the tracer in the weathering rind with an order of magnitude decrease in relative concentration through the iron band.

Introduction and Background

We measure diffusion coefficients of granite and granite fracture skins using Laser Ablation Inductively Coupled Plasma Mass Spectroscopy (LA-ICP-MS). Diffusion coefficient data are needed to quantify transport through porous media and fracture systems to address a variety of issues, including aquifer and petroleum reservoir exploitation, contaminant transport, and waste repository evaluation.

Diffusion is defined (Crank, 1975) as "the process by which matter is transported from one part of a system to another as a result of random molecular motions." This molecular motion (Brownian motion) is the means which ions diffuse in porous media and through fractures.

We have been evaluating flow and transport in fractured porous media with fracture skins (Fuller and Sharp, 1992; Fu et al., 1994; Kreisel and Sharp, 1996; Robinson et al., 1998; Sharp et al., 2003; Garner and Sharp, 2004; Garner et al., in press). It is documented that diffusion coefficients in the fracture skins is a key variable in attenuating or accelerating solute transport in fractured systems. However, diffusion coefficient data in specific rocks are not abundant in the literature. Our recent studies involving transport in granite fracture systems have found paucity of data. Researchers are forced to use the few experimental data (e.g., Skagius and Neretnieks, 1988) or adopt generic numbers that may or may not correspond to the specific sites in question. We have experimented with several methods used to estimate diffusion coefficients in sandstones and tuffs, but found inherent problems with all of the common methods (e.g., Fu et al., 1994, Landrum, 2000).

Diffusion coefficients in granite are traditionally measured in one of three ways: 1) ion flow through diffusion cells; 2) electrical resistivity; and 3) radioactive isotopes. The most utilized method for determining diffusion coefficients in granite uses ion diffusion cells (Garrels et al., 1949; Melnyk, 1983; Wadden and Katsube, 1982; Skagius and Neretnieks, 1982; Skagius and Neretnieks, 1985; Bradbury and Green, 1985, and Bradbury et al., 1982). Figure 3.14 demonstrates the first method in which concentrations of a selected ion, commonly chloride, are measured as it diffuses through a rock sample. Plotting measured concentration increase over time provides a straight line, the slope of which is used to estimate the diffusion coefficient. Landrum (2000) and Skagius and Neretnieks (1986a) applied the second method by measuring the diffusion coefficient as a function of resistivity. The physical set-up is similar to the first method but electrodes are used on each side of the flow through cell. (Figure 3.15) This technique is based on an analogy between Fick's Law, which is a function of the diffusion coefficient, and Ohm’s Law. The mathematical treatment is provided by Klinkenberg (1951). Resistivity measurements have the advantage in that they are much faster to measure, but resistivity is a function of a number of factors and, when compared the results from resistivity with diffusion cell methods, the estimated diffusion coefficients can vary significantly. The third method of measuring diffusion coefficients requires the use of radioactive isotopes and measuring the radioactivity profile in the sample (Wood et al., 1996).

Of the three methods, the diffusion cell is most acceptable in porous media (i.e., sandstone). If the media are relatively tight (i.e., granites), diffusion is slow and faster breakthrough may occur along the boundary between the sample and sample mount. In addition, preparing the thin rock disks can cause microfractures that can become significant in low porosity material. Resistivity methods overcome the time problem with the diffusion cells but, accuracy of the method is questionable. The third method, measuring radioactivity of isotopes does not require complete breakthrough of the diffusing ion. This is an advantage in terms of time, boundary effects, and sample alteration through preparation. If the concentration at the end of a sample remains zero, this allows for semi-infinite boundary conditions to be used to mathematically evaluate the diffusion coefficient. The ability to stop a test prior to tracer breakthrough and measure the concentration gradient is a distinct time advantage over waiting for concentration solution to increase with time. A major disadvantage is that there is an inherent problem with purchasing and handling radionuclides. We modify the third method and measure diffusion coefficients in low permeability media using CsCl salt and Laser Ablation ICP-MS. This method allows determination of diffusion coefficients for whole rock and delineation of preferential pathways through mineral grain boundaries and microfractures.

Methodology

Our method is designed so that: 1) complete breakthrough is not needed; 2) effects of transport along apparatus boundaries are minimized; 3) inexpensive and readily available cation tracers can be used; and 4) the spatial variability can of analyzed. The overall goal is to incorporate simplicity in a timely fashion.

Granite samples are cylindrical cores with a diameter of 2.54 cm and lengths varying between 1.27 cm and 5.08 cm. The cores are cut lengthwise into two halves and dried for one week. One half is saved for baseline analysis while the second half is saturated with a 1M LiBr solution. In order to expedite saturation, the sample is placed in a beaker with LiBr solution and set in a vacuum bell jar for 48 hours. After saturation, the sample is coated with paraffin wax leaving one end of the sample open (Figure 3.16) following the methodology of Wood et al. (1996). The samples coated in wax are placed in 1M CsCl solution for a period of time, in this case 8 months.

At the end of the time period, the samples are removed from the solution and the paraffin wax is removed. The samples are dried in an oven for 1 week to dry the pore fluid stopping diffusion and then cut in half lengthwise using a dry diamond blade. When the cut sample surface is relatively flat, the sample can be mounted in the laser-ablation apparatus. If the cut surface is rough, it must be leveled using a lapidary wheel.

Concentration profiles are measured using a New Wave 213 nm wavelength laser ablation unit coupled with a Micromass Platform Quadrapole ICP-MS. Transects were determined perpendicular to the direction of diffusive flux (y direction), 2mm apart. The data collected are cation concentrations measured on a sampling interval of 0.6996 seconds. By using the laser scan speed (25 $\mu m\ s^{-1}$), distance along transect can be determined. In order to determine if cation diffusion has occurred through the paraffin wax, plotting concentration vs. distance along a transect shows the concentration distribution along each transect. If diffusion has occurred through the wax layer the cation concentration will be consistently elevated at the ends close to the wax layer. We have not observed increased concentrations caused by diffusion through the wax or along the rock wax boundary.

This method provides a concentration gradient in one dimension (x axis) and requires the concentrations for each transect to be calculated with the arithmetic mean. The concentration gradient is shown by plotting the mean concentration vs. distance.

Mathematical Evaluation

The mathematical model calculates one-dimensional diffusion through fracture skins and into the rock matrix. The conceptual model (Figure 3.17) shows diffusion of solute into the end of the sample that is not covered with paraffin wax. Concentration within the skin is C_1 for the given skin thickness d for a penetration depth x_1 for a given time. Through the length of the matrix L concentrations C_2 are for penetration depth x_2.

The initial conditions for the skin and matrix are

$$C_1 = 0, \qquad C_2 = 0 \tag{1}$$

$$x_1 \geq 0, \qquad x_2 \geq 0. \tag{2}$$

The boundary conditions at the skin – matrix interface are

$$C_1 = C_2 \qquad \text{at} \qquad x_1 = b \tag{3}$$

$$\phi_1 D_1 \frac{\partial C_1}{\partial x_1} = \phi_2 D_2 \frac{\partial C_2}{\partial x_1} \text{ at} \qquad x_2 = 0 \tag{4}$$

where b is the skin thickness, D_1 is the effective diffusion coefficient for the fracture skin (m^2s^{-1}), D_2 is the effective diffusion coefficient in the rock matrix (m^2s^{-1}), ϕ_1 and ϕ_2 are porosity for the skin and matrix. The effective diffusion coefficient is less than the molecular diffusion coefficient in water because of the effects of tortuosity and, perhaps, ion exclusion by restricted pore throats.

Boundary conditions for the solution - skin interface and wax boundary – solution interface, respectfully are

$$C_1 = C_0 \qquad \text{at} \qquad x_1 = 0 \tag{5}$$

$$\frac{\partial C_2}{\partial x_2} = 0 \qquad \text{at} \qquad x_2 = L. \tag{6}$$

Transport of mass through the fracture skin and rock matrix is diffusion controlled. Therefore the basic equations for the skin and matrix are

$$D_1 \frac{\partial^2 C_1}{\partial x^2} = R_1 \frac{\partial C_1}{\partial t} \tag{7}$$

$$D_1 \frac{\partial^2 C_2}{\partial x^2} = R_2 \frac{\partial C_2}{\partial t} \tag{8}$$

where R1 and R2 are retardation factors accounting for mass absorption.

The Laplace transform equation

$$\{U_1, U_2\} = \mathcal{L}\{C_1, C_2\} = \int_0^\infty e^{-pt} \{C_1, C_2\} dt \tag{9}$$

gives the differential equations

$$\frac{\partial^2 U_1}{\partial x_1^2} - \frac{p}{D_1} U_1 = 0 \tag{10}$$

$$\frac{\partial^2 U_1}{\partial x_2^2} - \frac{p}{D_2} U_2 = 0 \tag{11}$$

where

$$\alpha_1^2 = R_1 \frac{p}{D_1} \tag{12}$$

$$\alpha_2^2 = R_2 \frac{p}{D_2}. \tag{13}$$

The above differential equations (10) and (11) can be solved with the boundary conditions surrounding the sample.

$$U_1 = \frac{C_0}{p} \qquad \text{at} \qquad x_1 = 0 \tag{14}$$

$$\frac{\partial U_2}{\partial x_2} = 0 \qquad \text{at} \qquad x_1 = L \tag{15}$$

And the boundary conditions at the skin – matrix interface.

$$U_1 = U_2 \tag{16}$$

$$\phi_1 D_1 \frac{\partial U_1}{\partial x_1}\bigg|_{x_1=\omega} = \phi_2 D_2 \frac{\partial U_2}{\partial x_2}\bigg|_{x_2=0} . \tag{17}$$

Using numerical inversion solving for the ideal complete expressions for U_1 and U_2 provides

$$\begin{aligned} U_1 &= \frac{C_0}{p}\left\{\cosh\alpha_1 x_1 - \sinh\alpha_1 x_1\left[\frac{\sinh\alpha_1\omega + k\cosh\alpha_1\omega}{\cosh\alpha_1\omega + k\sinh\alpha_1\omega}\right]\right\} \\ &= \frac{C_0}{p}\left\{\frac{\cosh\alpha_1(\omega - x) + k\sinh\alpha_1(\omega - x)}{\cosh\alpha_1\omega + k\sinh\alpha_1\omega}\right\} \end{aligned} \tag{18}$$

and

$$\begin{aligned} U_2 &= \frac{C_0}{p}\left[\frac{\cosh\alpha_2 x_2 - \tanh\alpha_2 L\sinh\alpha_2 x_2}{\cosh\alpha_1\omega + k\sinh\alpha_1\omega}\right] \\ &= \frac{C_0}{p}\frac{\cosh\alpha_2(L - x_2)}{\cosh\alpha_2 L[\cosh\alpha_1\omega + k\sinh\alpha_1\omega]} . \end{aligned} \tag{19}$$

Because of robustness of the solutions for U_1 and U_2 in Laplace space, (18) and (19) are not analytically transformed back into terms of C_1 and C_2. Results of equations (18) and

(19) are solved using a simple yet robust code for numerical inversion of Laplace transforms (Robinson and Maul, 1991) based on theoretical work by Green (Talbot, 1979).

Experimental Results and Discussion

Diffusion coefficients are determined for granite samples with clay coating fracture skin and weathering rind with iron banding parallel to the fracture surface. Specimen E10 shows clay coating alteration at the fracture surface; specimen NB4 shows weathering rind and iron banding. These samples are selected to show variation in diffusion coefficients for fracture skins that enhance (E10) and attenuate (NB4) transport in a fracture (Garner et al., in press; Robinson et al., 1998).

Plotting the raw data in counts verses time provides a chromatogram for each sample. Both sample show trends to the pathways tracer penetrates into the sample. Spikes of high concentration form linear patterns in sample E10 migrating from the top right to the bottom left (Figure 3.18). Chromatogram transects correlate to the lines drawn in the sample photo. For sample E10 the y-axes are not scaled the same in each transect. This is done to magnify the linear diffusion pathways represented by concentration spikes. Sample NB4 (Figure 3.19) shows the y-axes to scale showing the significant drop in concentration transitioning from the weathering rind to the iron band. Linear pathways can also be seen in the two dimensional cut of sample NB4.

Chromatograms clearly show diffusion pathways are channeled on a small scale. Comparing linear diffusion pathways shown on the chromatogram of sample E10 to the sample image shows preferential diffusion in the same direction finer grained mafic minerals are arranged in the sample. This suggests diffusive flux is preferential along grain boundaries and cleavage planes in low-permeability crystalline rocks. The difference in tracer concentration between weathering rind and iron band is shown to be about one order of magnitude in sample NB4.

When multiple cations are measured grain boundary contacts and transport pathways can be determined (Figure 3.20). Measuring multiple cations that characterize the major rock forming minerals along a single line enables mineralogy to be determined. When tracer is simultaneously measured with rock forming cations transport pathways across the line appear in the form of tracer spikes.

The diffusion coefficient determined for the rock matrix of sample E10 (Figure 3.21) is $9x10^{-11}$ m^2 s^{-1} and the clay coating is $1.75x10^{-11}$ m^2 s^{-1}. Fracture surface alteration by clay coating decreases the diffusion coefficient by approximately one order of magnitude. Comparing the diffusion coefficients of the rock matrix of E10 to published values ($1x10^{-12}$ to $1x10^{-13}$ m^2 sec^{-1} from Skagius and Neretnieks, 1986b), shows that diffusion in E10 is faster by two to three orders of magnitude. We attribute this to the fact that ours are near-surface samples and the diffusion experiment is not conducted under pressure. Samples of granites collected near the land surface can be expected to have differing properties to conventional samples at depth (Skagius and Neretnieks, 1986b). We have, for instance, measured porosities in granite exceeding 10% in our samples.

Results for sample NB4 show a faster diffusion flux through the weathering rind and a slower flux through the iron banding (Figure 3.22). The diffusion coefficients are $3.8\text{x}10^{-11}$ m^2 s^{-1} and $1.9\text{x}10^{-12}$ m^2 s^{-1} respectively, for weathering rind and iron banding. Observed data through the weathering rind tails off through the weathering rind which, is not expected for the samples. It is believed that by drying the sample fluid with tracer is driven from the sample creating the rising limb. Assuming the loss of tracer through the more porous weathering rind provides two points to model diffusion in the sample. Because the diffusion coefficient falls within a reasonable range for more porous weathering rinds in granite sampled at the surface, it is inferred the reported diffusion coefficient and interpretation is justified.

Conclusions

Laser ablation ICP-MS is a relatively new technique and has not been applied to hydrogeological problems. We demonstrate its usefulness in determining aqueous phase diffusion coefficients and the potential for showing channel paths on the micro-scale. By simplifying the diffusion cell method to allow the diffusive flux to enter a sample in one direction, the time needed to determine diffusion coefficients is reduced. Processing samples as outlined above allows cation measurement with laser ablation ICP-MS. Transects are scanned and the arithmetic means of the transect concentrations are used to determine one dimensional concentration profiles. The effective diffusion coefficients can be estimated with a mathematical solution (provided above) or a numerical approximation, if preferred. The LA-ICP-MS data in two dimensional chromatograms show spikes of solute as linear features through sample E10. These linear features can represent microfractures, grain boundaries, or cleavage planes. These data imply diffusive transport controlled by the macroporosity and delineate preferred transport pathways. Three dimensional paths could be determined by using a lap to remove layers of sample and re-ablating the grid of transects. Sample NB4 show a significant concentration of tracer in the weathering rind with an order of magnitude decrease in tracer concentration in the iron band.

Diffusion coefficients in fresh granite have been estimated to range between $1\text{x}10^{-12}$ and $1\text{x}10^{-13}$ m^2 sec^{-1} (Skagius and Neretnieks, 1986b). Our measured rock matrix value of $9\text{x}10^{-11}$ m^2 sec^{-1} from LA-ICP-MS is about two orders of magnitude higher. This difference is contributed to sampling locations for this study and the fact that Skagius and Neretnieks (1986b) conducted their studies under pressure on samples collected in tunnels at depth. Our samples were collected from the near-surface sites where stresses are reduced. With this in mind, we infer the method presented above presents accurate diffusion coefficients that represent correct values for granites at the near surface.

The LA-ICP-MS allows for multiple diffusion coefficients to be measured within a double layer sample (e.g., granite fracture skins and matrix). Fracture skin forming the first layer of the sample discussed has a clay coating fracture skin that enhances transport through the fracture. The estimated diffusion coefficient in the clay coating is $1.75\text{x}10^{-11}$ m^2 sec^{-1}. Variation in diffusion coefficients from fracture skin to the rock matrix is roughly one order of magnitude. The lower diffusion coefficient for the clay coating allows less diffusion of mass from the fracture reducing the effect of matrix diffusion and enhancing transport through the fracture. Using the double layer model with a weathering rind and iron band shows a significant decrease in the diffusion coefficient in the iron band relative to the weathering rind. This increased diffusive flux at the fracture surface allows more mass to be temporarily stored in the skin and attenuates transport along the fracture.

This paper shows several applications for determining transport properties using LA-ICP-MS. Throughout the literature laser ablation has been used for determining solid state diffusion of cations on the individual grain scale. As the number of research facilities that use laser ablation increases new applications will continue to appear in the literature. In the mean time laser ablation is under utilized in hydrogeology as a research tool and in particularly for quantifying transport properties.

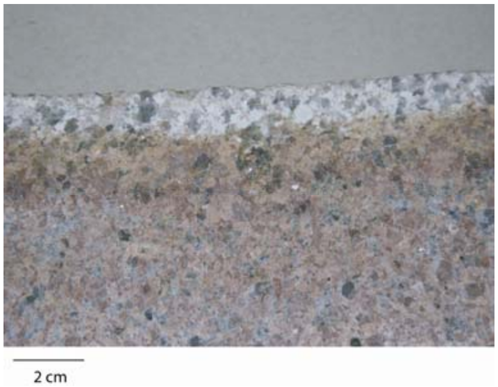

Figure 3.01: Town Mountain granite with dual fracture skin.

Figure 3.02: Town Mountain granite with pyrolusite coating fracture surface.

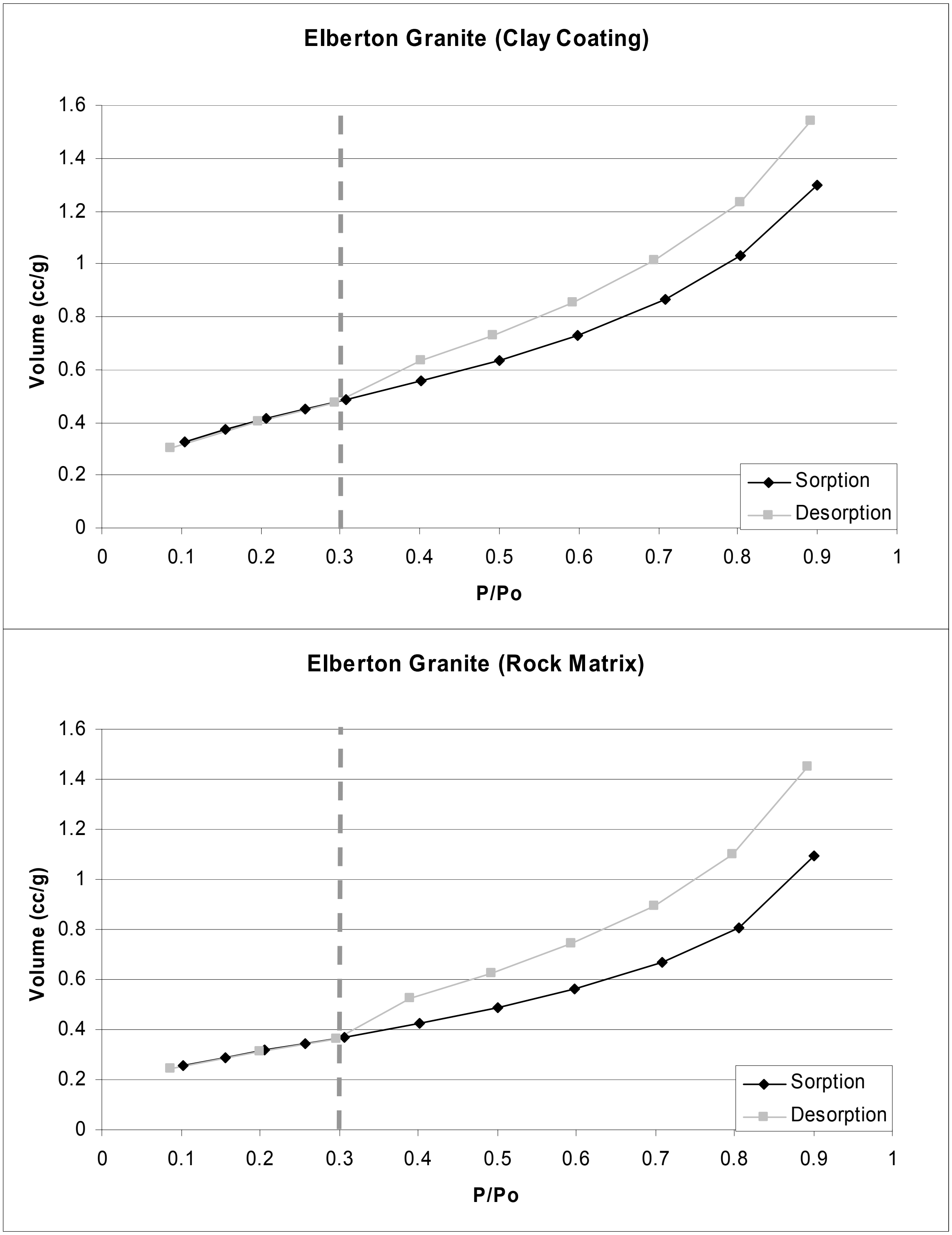

Figure 3.03: Hysteresis curves for Elberton Granites fracture skin and rock matrix. Both curves are indicative of slit-shaped pores. The dashed line shows the relative pressure 0.3.

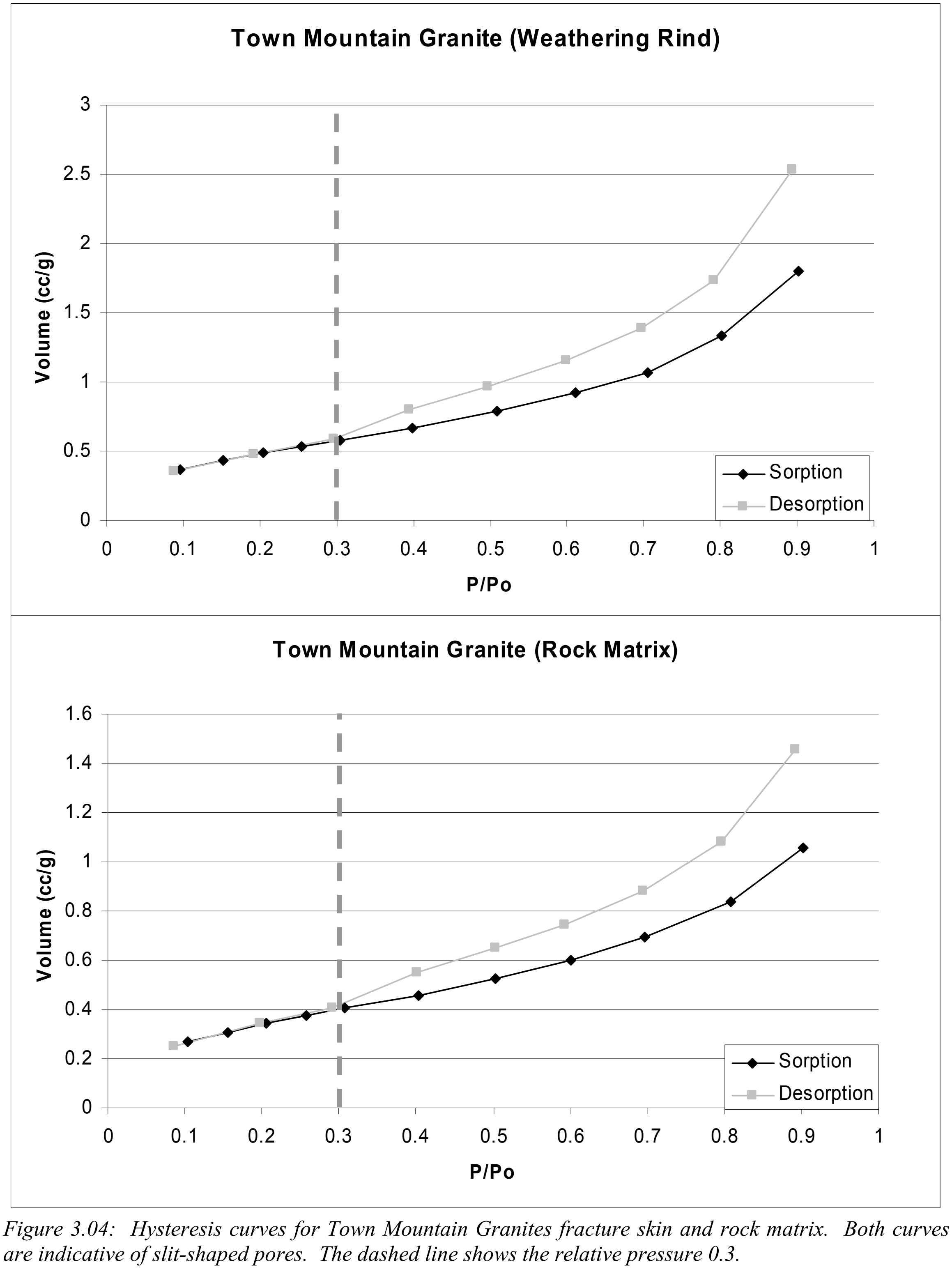

Figure 3.04: Hysteresis curves for Town Mountain Granites fracture skin and rock matrix. Both curves are indicative of slit-shaped pores. The dashed line shows the relative pressure 0.3.

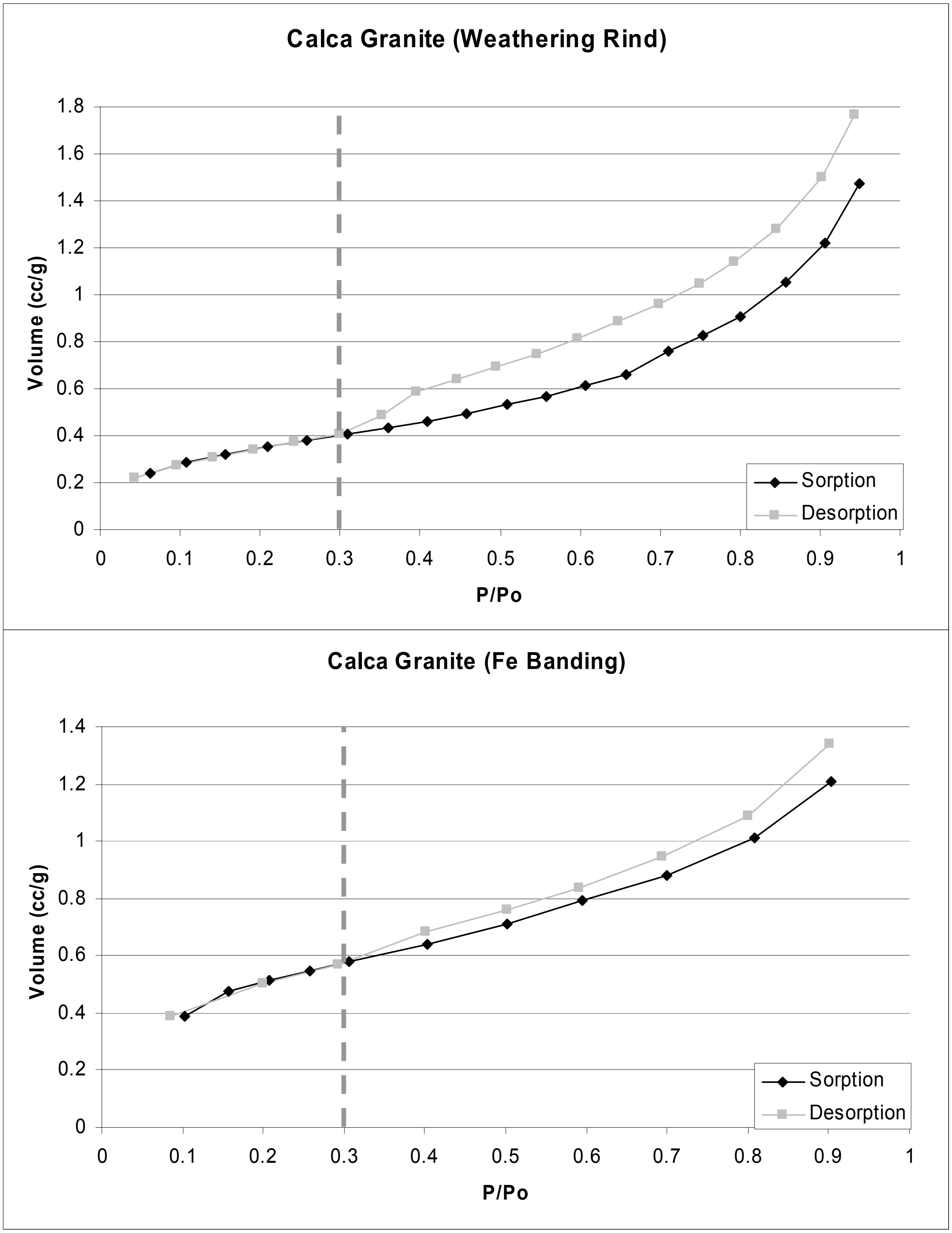

Figure 3.05: Hysteresis curves for Calca Granites weathering rind and iron banding. Both curves are indicative of slit-shaped pores. The dashed line shows the relative pressure 0.3.

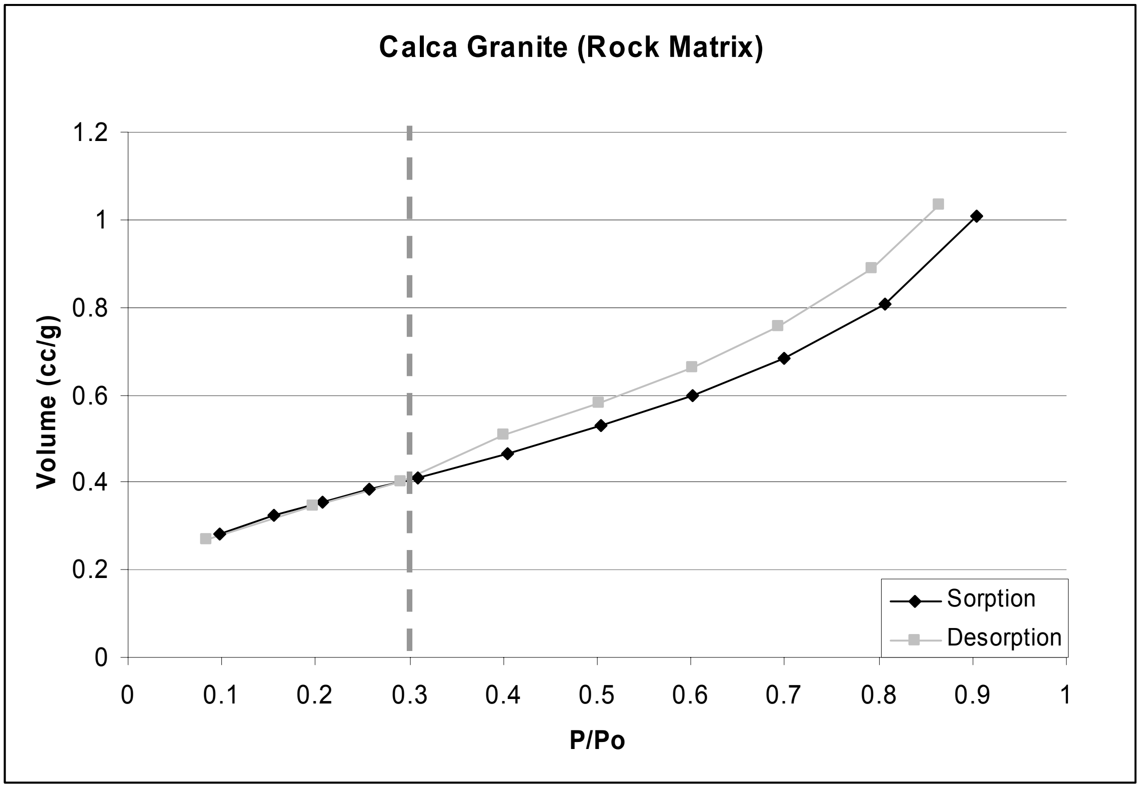

Figure 3.06: Hysteresis curve for Calca Granites rock matrix. Both curves are indicative of slit-shaped pores. The dashed line shows the relative pressure 0.3.

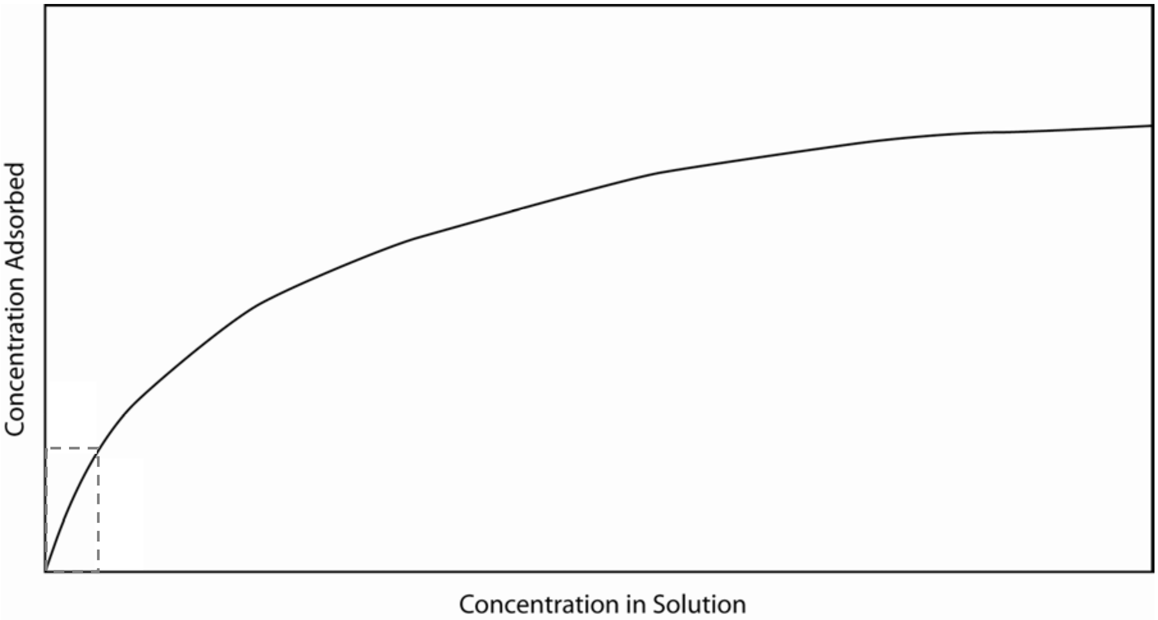

Figure 3.07: An illustration of a Langmuir isotherm. The gray dashed box represents the area of the curve that approaches a linear relationship between concentration in solution and concentration adsorbed.

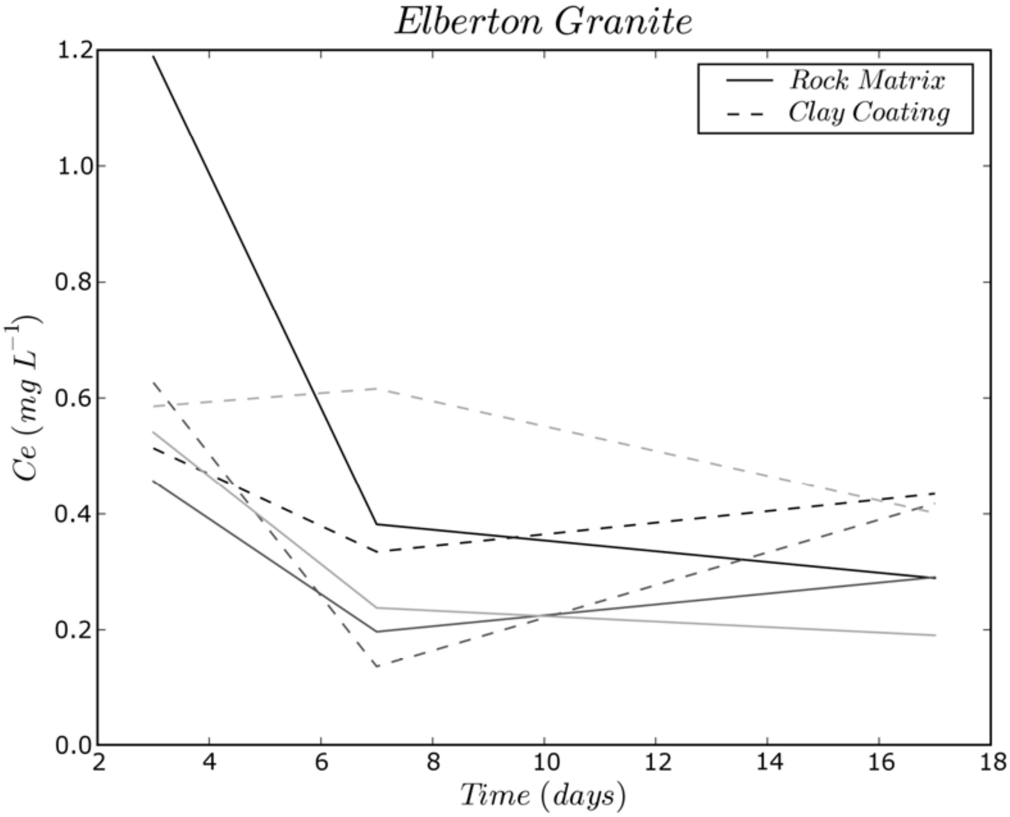

Figure 3.08: Plot showing concentration of solution concentration change with time. The Elberton Granite approaches equilibrium in 17 days. Darker shades represent higher initial concentrations and lighter shades represent lower initial concentrations.

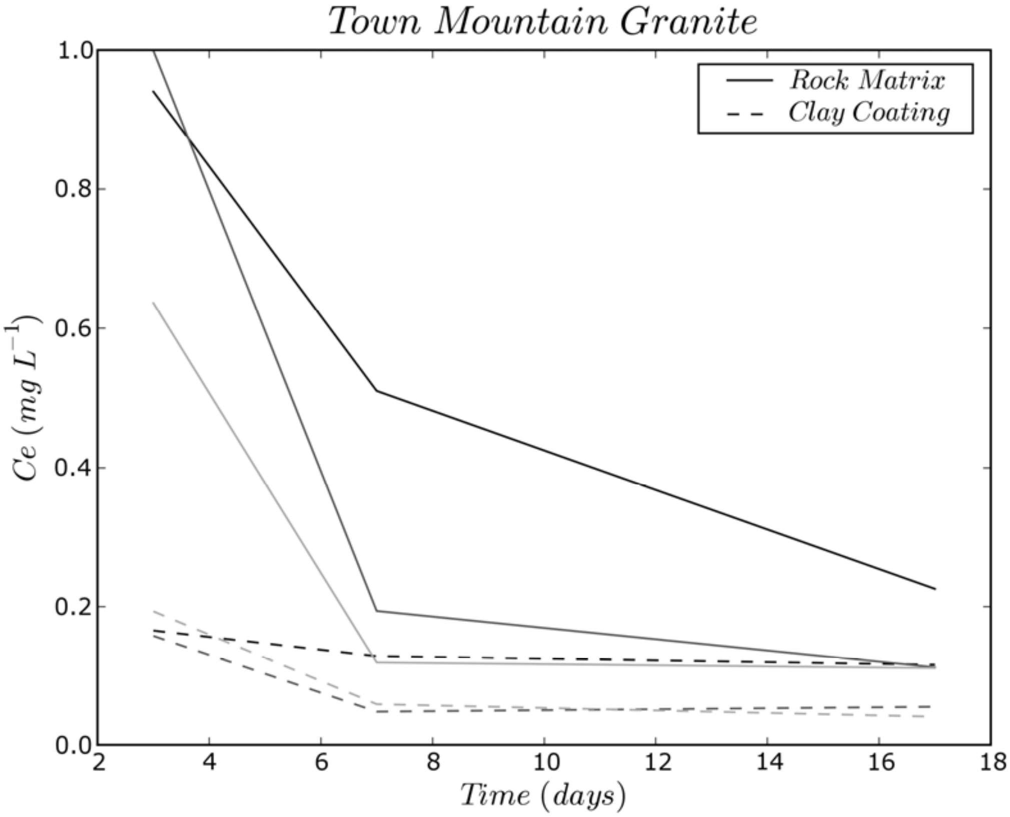

Figure 3.09: Plot showing concentration of solution concentration change with time. The Town Mountain Granite approaches equilibrium in 17 days. Darker shades represent higher initial concentrations and lighter shades represent lower initial concentrations.

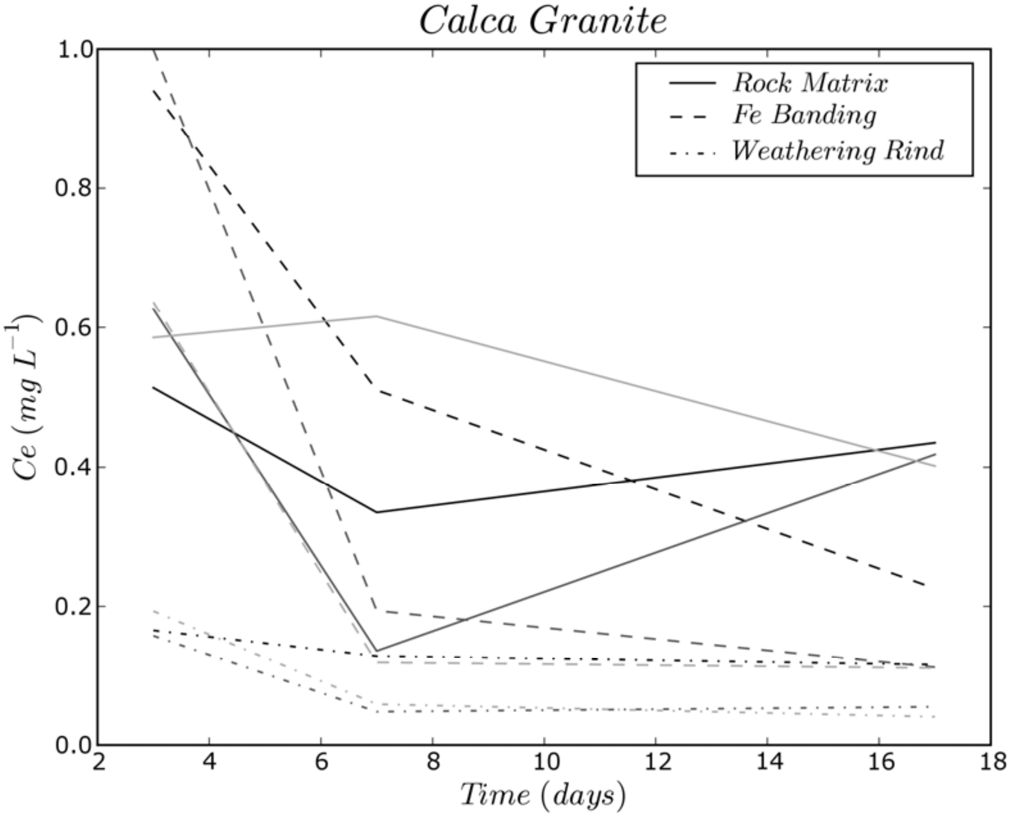

Figure 3.10: Plot showing concentration of solution concentration change with time. The Calca Granites approaches equilibrium in 17 days. Darker shades represent higher initial concentrations and lighter shades represent lower initial concentrations.

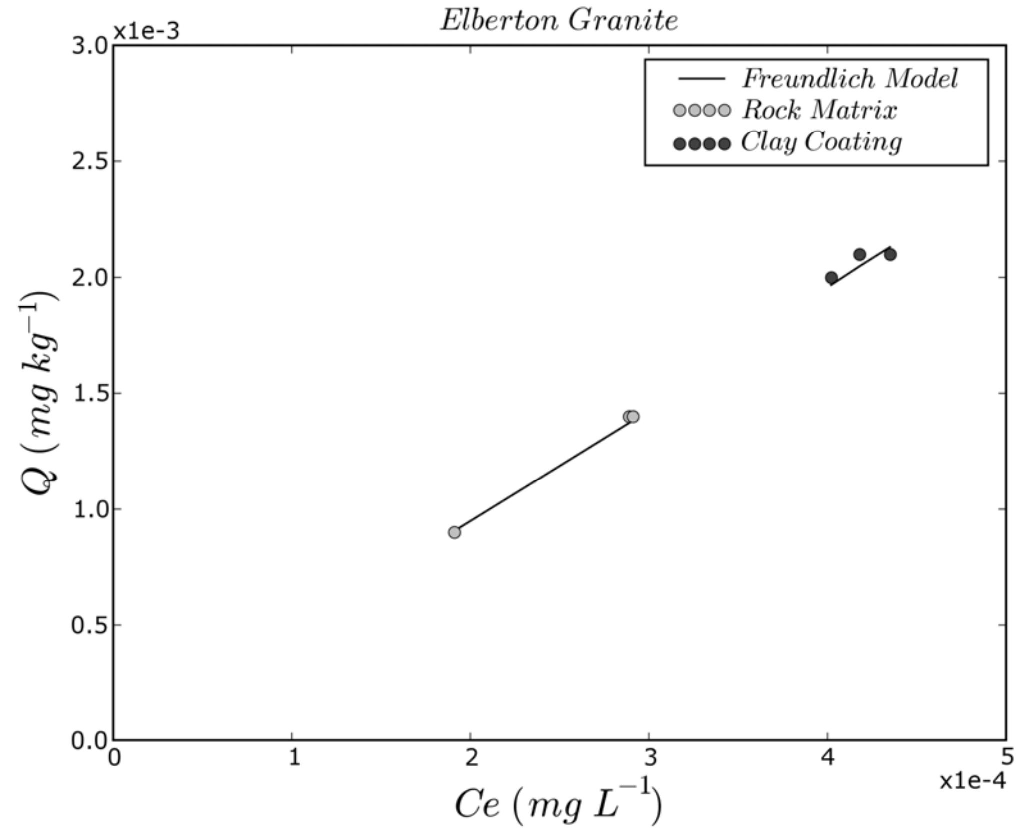

Figure 3.11: Linear adsorption isotherm for rock matrix and clay coated samples from the Elberton Granite.

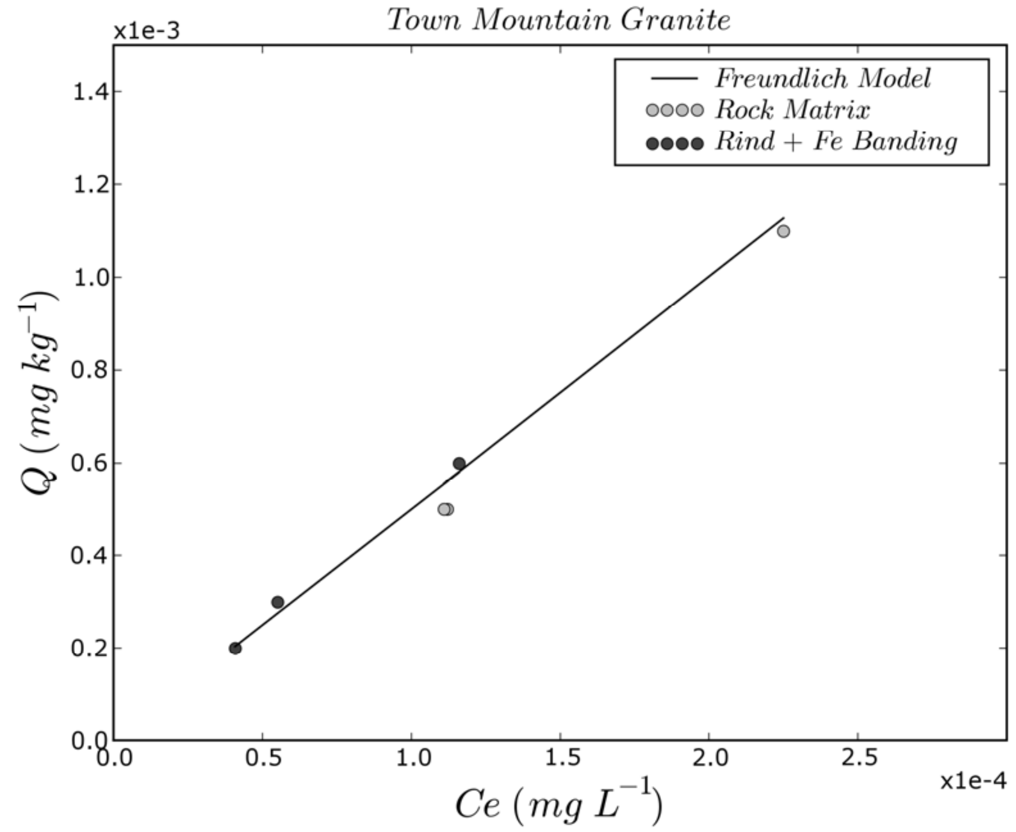

Figure 3.12: Linear adsorption isotherm for rock matrix and combined weathering rind and iron band samples from the Town Mountain Granite.

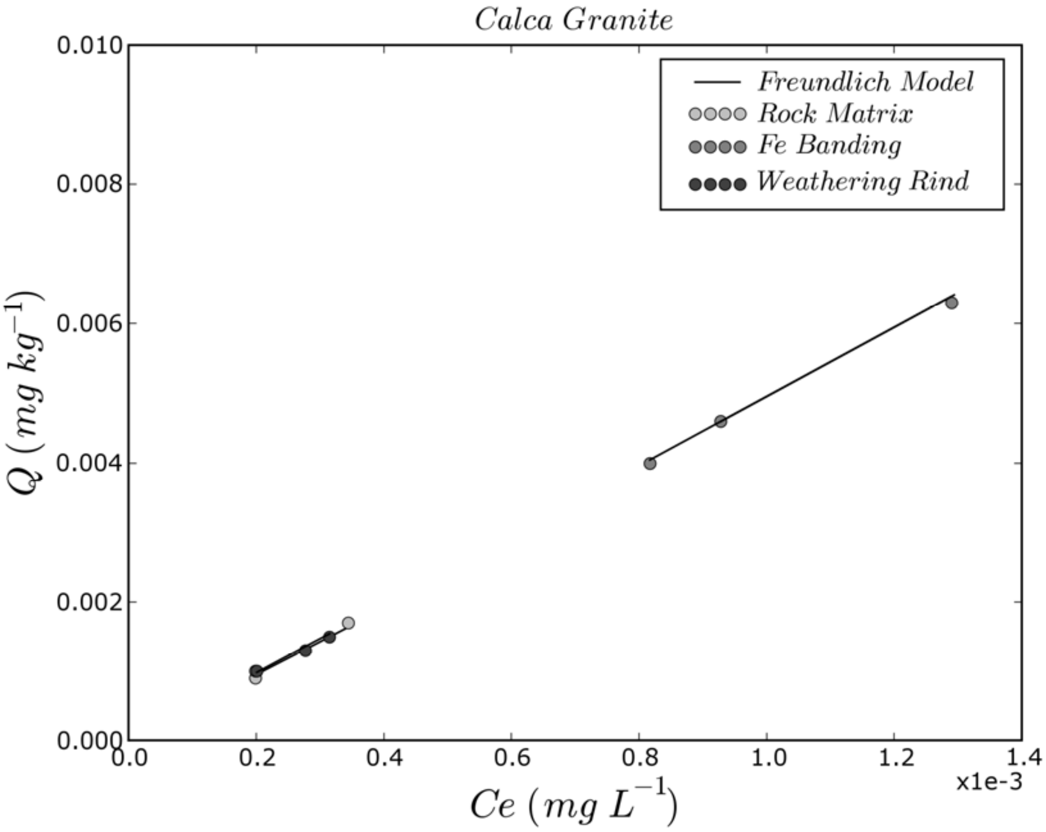

Figure 3.13: Linear adsorption isotherm for separate rock matrix, iron band, and weathering rind samples from the Calca Granite.

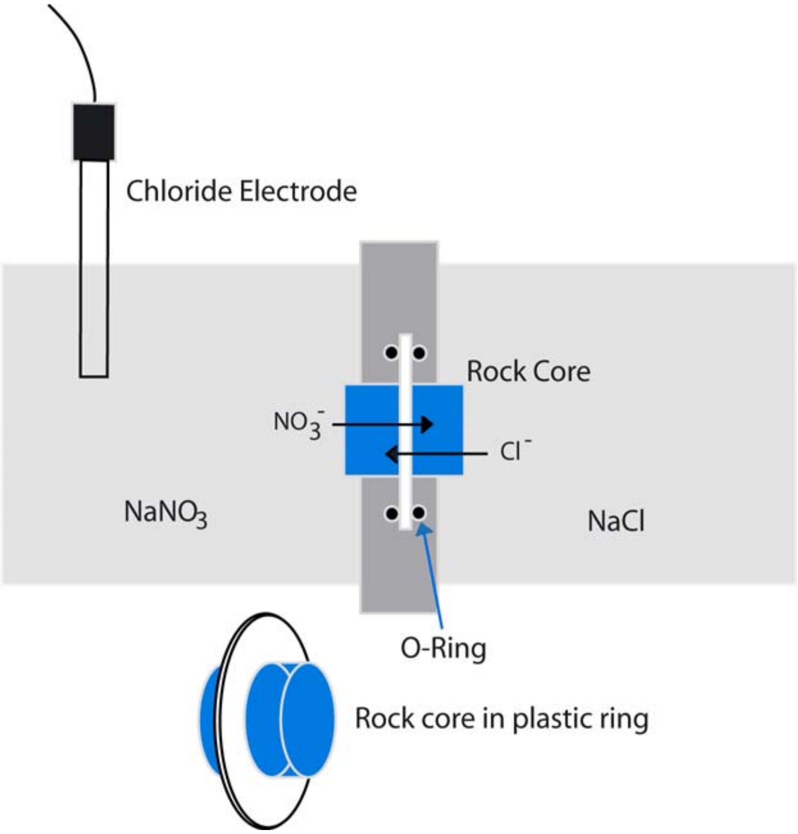

Figure 3.14: Schematic of diffusion cell used to determine diffusion coefficients. (After Landrum, 2000)

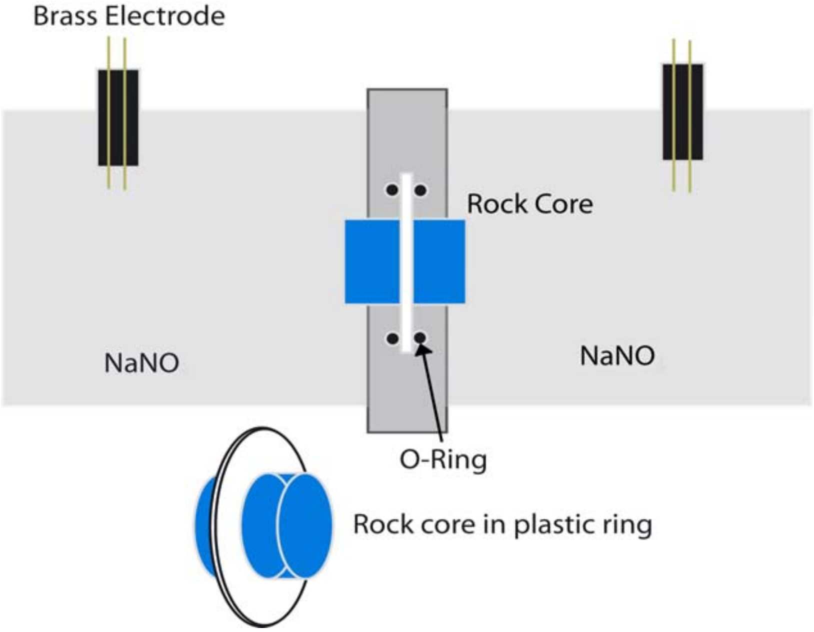

Figure 3.15: Diffusion cell rearranged to measure diffusion coefficients using resistivity. (After Landrum, 2000)

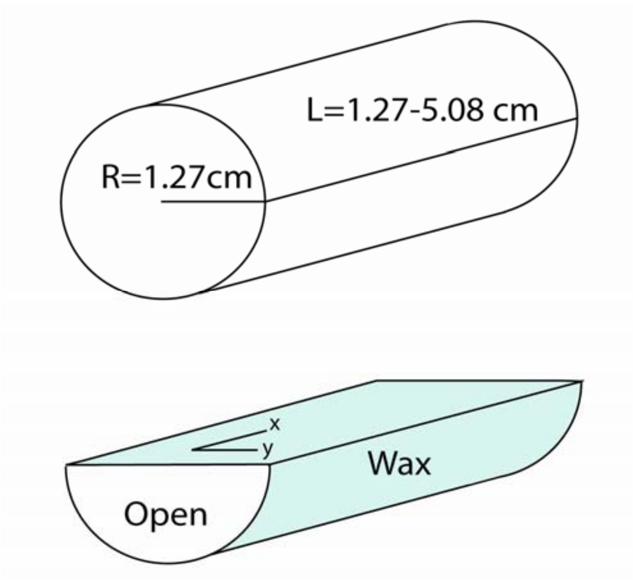

Figure 3.16: Rough core dimensions and image of method for allowing diffusion in one dimension in a granite sample.

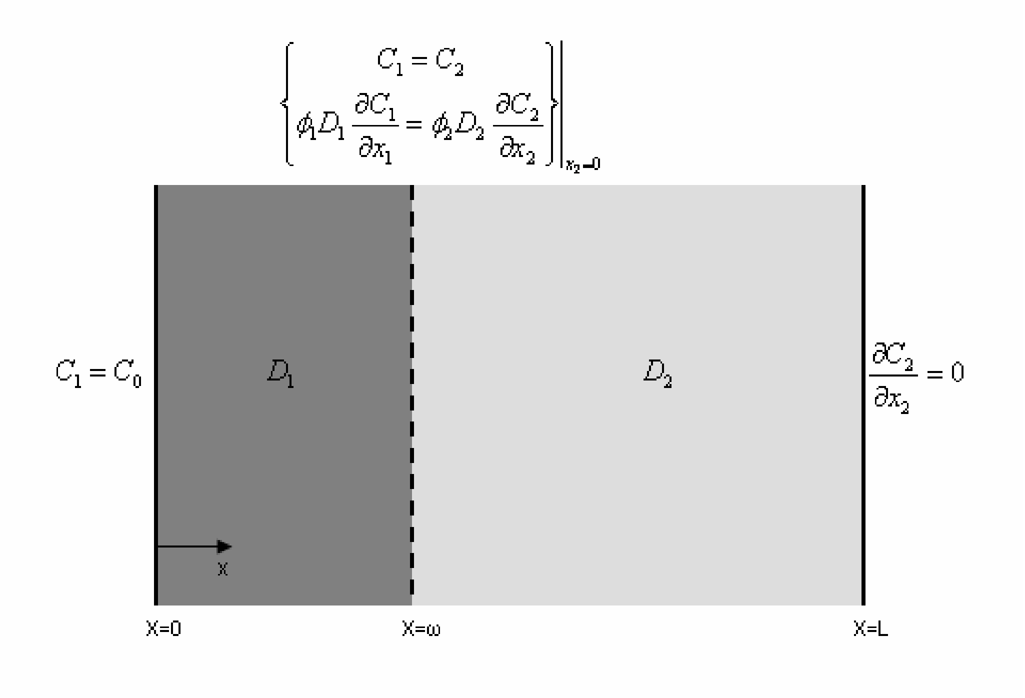

Figure 3.17: Conceptual model of diffusion in the x direction through an alteration layer with different transport properties than the rock matrix.

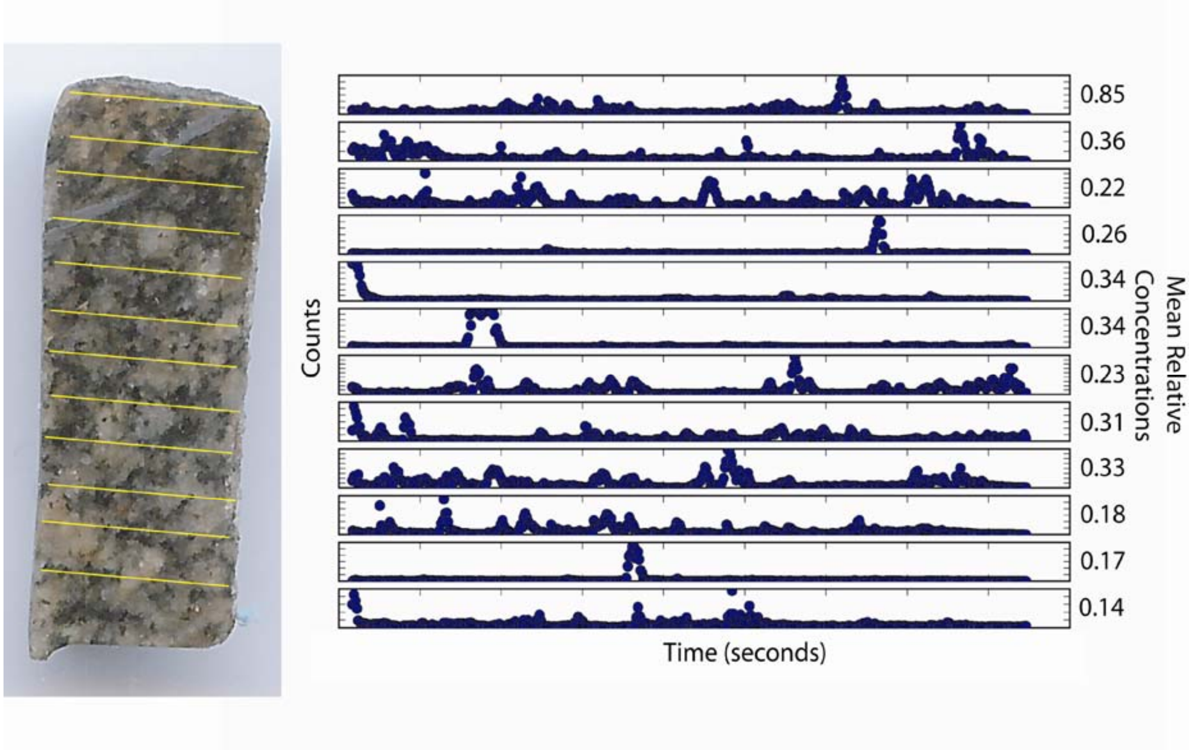

Figure 3.18: Chromatogram for sample E10 showing Cs counts verses the transect length. Each transect represents a 2 mm spacing on the granite sample. Mean relative concentration is also provided.

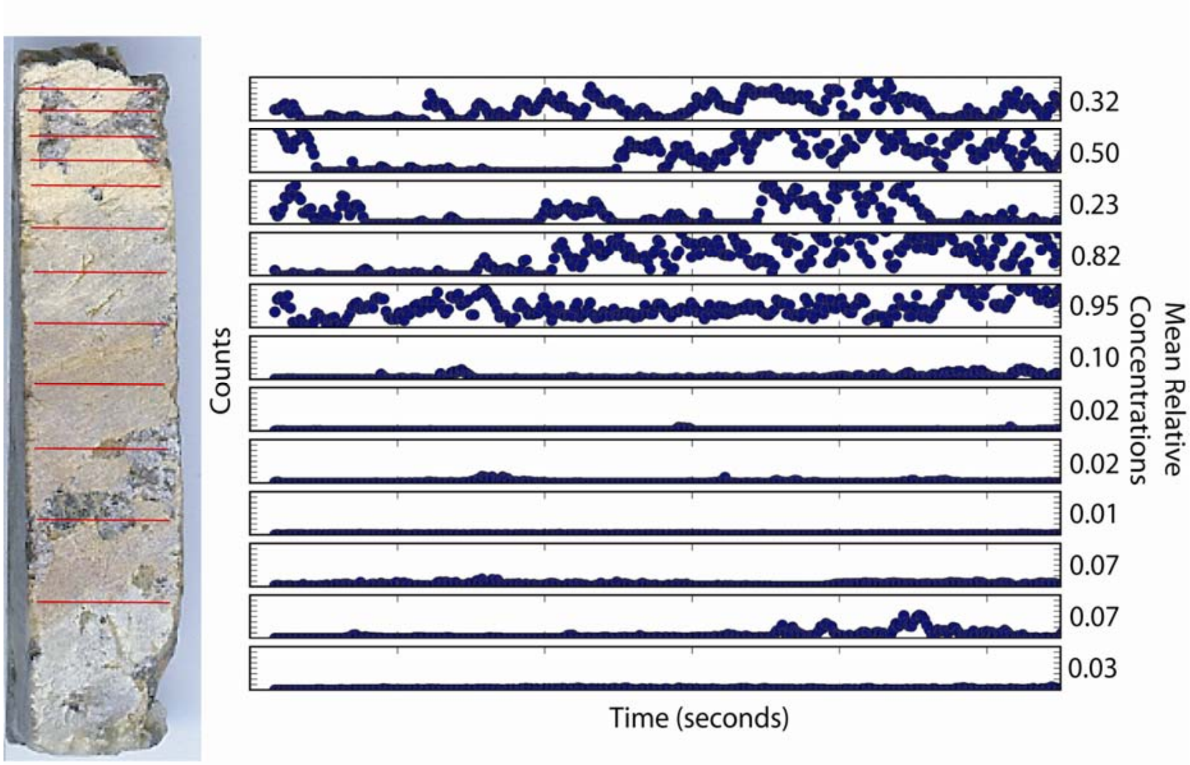

Figure 3.19: Chromatogram for sample NB4 showing Cs counts verses the transect length. Transects have an increasing spacing from 1 to 5 mm. Mean relative concentration is also provided.

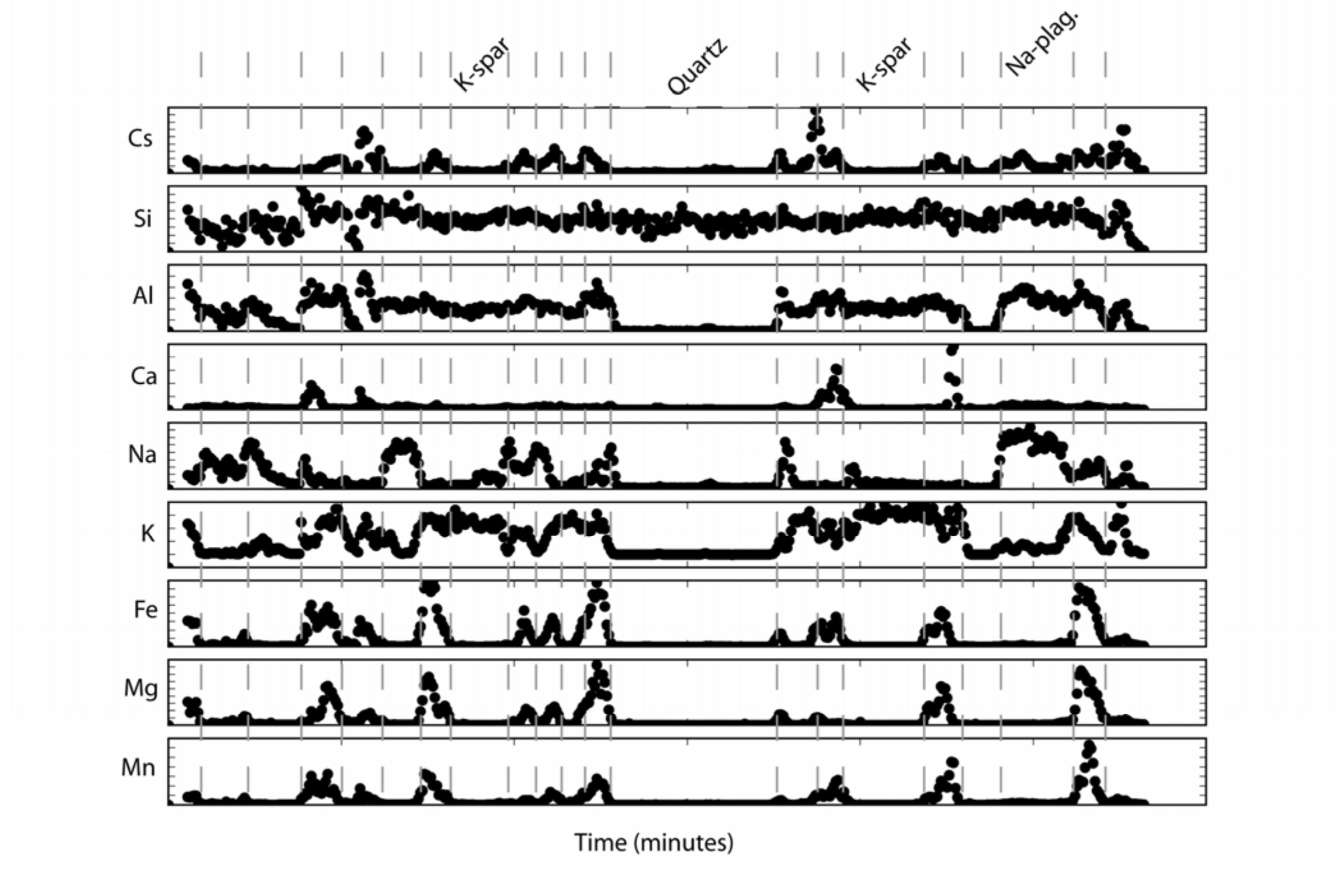

Figure 3.20: Chromatogram of all cations measured for line 7 of sample E10. The plot shows cation counts verses time with dashed gray lines inferring mineral boundaries along the scanned line. At the top of the image the four largest spacing of inferred mineralogy are labeled.

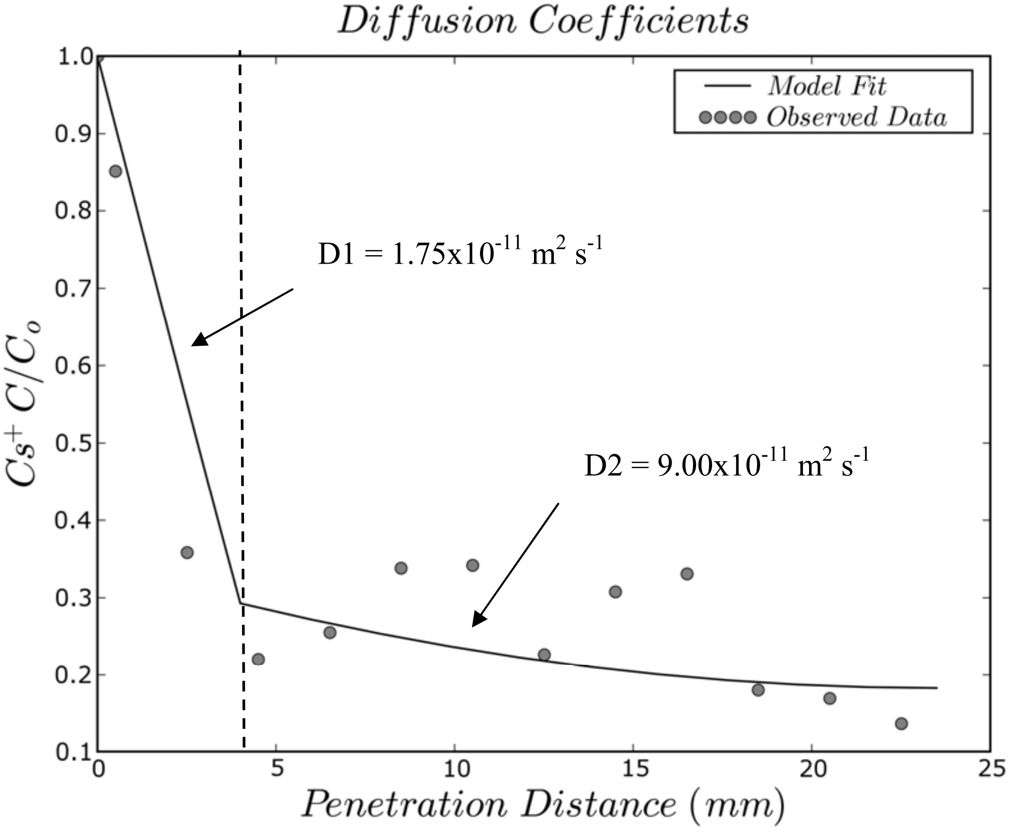

Figure 3.21: Sample E10 mean transect concentrations in dots. Line fit showing a diffusion coefficient of $9x10^{-11}$ m^2 s^{-1} in the matrix and $1.75x10^{-11}$ m^2 s^{-1} in the clay filled fracture skin.

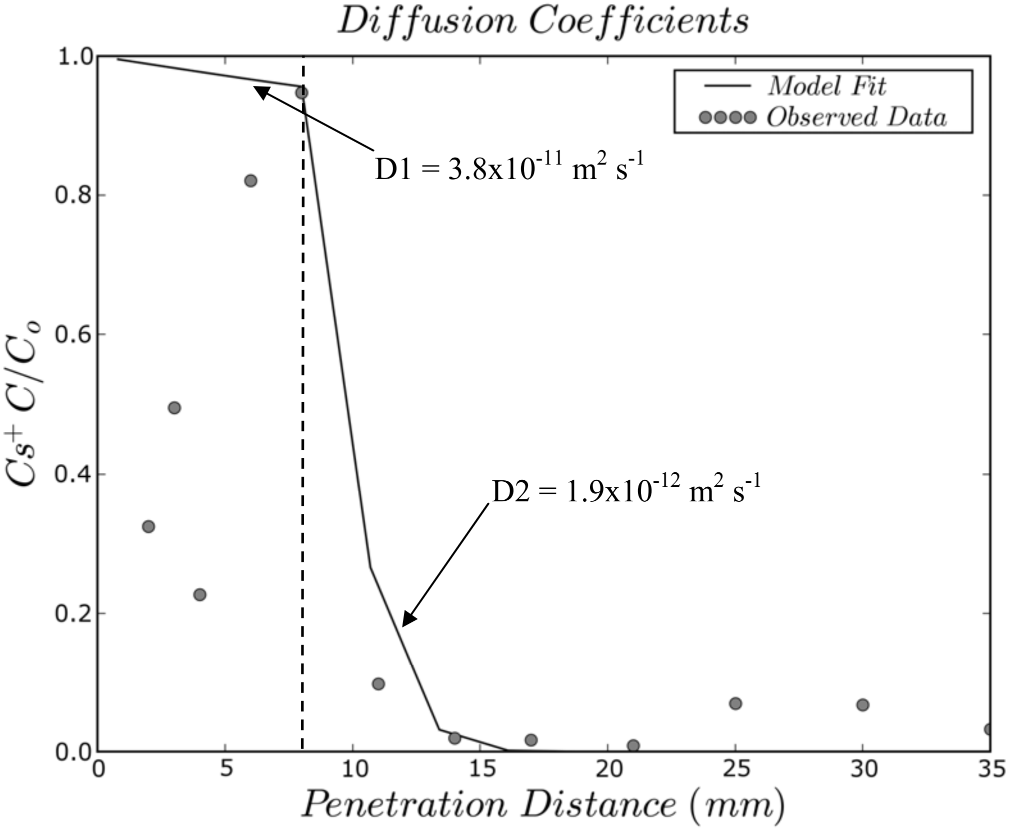

Figure 3.22: Sample NB4 mean transect concentrations in dots. Line fit showing a diffusion coefficient of 3.8×10^{-11} m^2 s^{-1} in the weathering rind and 1.9×10^{-12} m^2 s^{-1} in the iron banded fracture skin.

	Elberton, Georgia	
Sample #	**Description**	**Porosity %**
E_1	Weathering Rind	8.2
E_5a	Fe / Clay Stained Surface	BDL
E_5b	Matrix	3.1
E_7a	Stain & Organics	1.4
E_7b	Matrix	2.4
E_10a	Dust Film	0.8
E_10b	Matrix	2.3

Table 3.01: Elberton granite porosity measurements using mercury injection.

Fredericksburg, Texas		
Sample #	**Description**	**Porosity %**
F_4a	Weathering Rind	6.2
F_4b	Fe Banding	3.2
F_4c	Matrix	1.9
F_4d	MnO2 Coating	BDL
F_4e	Matrix	1.9
F_5a	Weathering Rind	6.9
F_5b	Fe Banding	3.0
F_5c	Matrix	1.7
F_8a	Weathering Rind	4.9
F_8b	Fe Banding	1.9
F_8c	Matrix	1.5
F_11	Slickenside	3.48
F_12a	Weathering Rind	13.9
F_12b	Fe Banding	1.4
F_12c	Matrix	4.9

Table 3.02: Town Mountain Granite porosity measurements using mercury injection.

South Australia			South Australia		
Sample #	**Description**	**Porosity %**	**Sample #**	**Description**	**Porosity %**
WQ1A	Clay fill (Frac. Surface)	5.48	WC1iii	Fe Band	5.03
WQ1B	Transition	5.52	WC1iv	Mx	0.23
WQ1C	Matrix	3.13	WC2A	Weathering Rind	6.40
MW1A	Clay Coating	6.44	WC2B	Fe banding	3.05
MW1B	Matrix	3.57	WC2C	Matrix	4.74
TC1A	Weathering Rind	7.18	WC5A	Weathering Rind	6.71
TC1B	Matrix	4.12	WC5B	Fe Banding	3.45
YR1A	Weathering rind	8.74	WC5C	Matrix	3.39
YR1B	Fe Banding	2.30	WC6Ai	Rind	13.81
YR1C	Matrix	3.79	WC6Aii	Matrix	5.51
YR3i	Top of sample	6.14	WC6B	1/8" Rind +Matrix	7.28
YR3ii	Middle of sample Mx	3.98	WC7A	Weathering Rind	13.97
YR3iii	Matrix	4.32	WC7B	Weathering Rind	8.27
YR4A	Rind + Roots	13.45	WC7C	Fe & Rind	5.75
YR4B	Weathering Rind	19.32	WC7D	Fe	4.39
YR5A	Surface Coating	2.62	WC8i	Weathering Rind	7.92
YR5B	High Ferro/Mag.	2.33	WC8ii	Fe w/some leaching	5.28
YR5C	Matrix	1.96	WC8iii	Matix w/some leaching	4.51
WC1i	Weathering Rind	10.29	WC8iv	Matrix	4.51
WC1ii	Rind w/ Fe	13.18	WC12	Matrix	0.48

Table 3.03: Calca granite porosity measurements using mercury injection.

Mount Monster & Padthaway Quarry		
Sample #	**Description**	**Porosity %**
NB6A	Rind	12.9400
NB6B	Matrix	2.6100
NB6C	Rind/Fe Banding	4.1000
MM1A	Rind	21.4900
MM1B	Fe Banding	2.8100
MM1C	Matrix	7.2500
MM3A	Fe Banding/Thin Rind	3.8600
MM3B	Matrix	3.3500
MM3C	Matrix	2.1800
MM5A	Weathering Rind	14.0700
MM5B	Fe Banding	6.5300
MM6A	Weathering Rind	13.6400
MM6B	50% Fe & 50% Mx	4.7500
MM6C	Matrix	1.8000
MM7A	Epidote Vein	12.1400
MM7B	Transition Zone	1.8100
MM7C	Matrix	2.3900

Table 3.04: Mount Monster and Padthaway quarry porosity measurements using mercury injection.

Location	Description	Density (g cm^{-3})	Mico-Porosity %
Elberton, Georgia	clay coating	2.34	0.138
Elberton, Georgia	rock matrix	2.65	0.121
Fredericksberg, Texas	thin weathering rind with iron banding	2.12	0.147
Fredericksberg, Texas	rock matrix	2.58	0.126
South Australia	well developed weathering rind	2.47	0.126
South Australia	well developed iron band	2.35	0.176
South Australia	rock matrix	2.74	0.14

Table 3.05: Table shows densities determined by helium pycnometery and micro-porosity measurements determined using total pore volume from BET.

Location	Description	Surface Area (m^2 g)	Slope	Y-Intercept	C
Elberton, Georgia	clay coating	1.265	1646	46.34	36.52
Elberton, Georgia	rock matrix	1.129	1855	40.33	47
Fredericksberg, Texas	thin weathering rind with iron banding	1.699	1212	48.58	25.94
Fredericksberg, Texas	rock matrix	1.203	1731	49.28	36.12
South Australia	well developed weathering rind	0.876	2386	57.18	42.74
South Australia	well developed iron band	1.447	1469	10.63	139.1
South Australia	rock matrix	0.9213	2291	32.28	71.97

Table 3.06: BET surface area measurements using argon gas as a sorbate. Slope, Y-Intercept, and BET C constant provided to show validity of analyses and parameters needed to build isotherm

	Hg Injection			BET (Ar Injection)			Ka (m)	R (-) Porous	b (cm)	R (-) Fracture
Elberton	**porosity**	**density**	**A_S (m^2 g^{-1})**	**porosity**	**density**	**A_S (m^2 g^{-1})**				
Rock Matrix	0.024	2.604	3.473	0.001	2.650	1.129	4.21E-06	17	1.02E-06	9
Clay Coating	0.008	2.356	2.647	0.001	2.340	1.265	3.87E-06	32	2.50E-07	32
Town Mountain										
Rock Matrix	0.049	2.511	3.217	0.001	2.580	1.203	4.16E-06	8	7.10E-07	13
Rind and Fe Band	0.058	2.501	4.478	0.001	2.120	1.699	2.94E-06	7	2.05E-06	4
Calca										
Rock Matrix	0.005	2.599	6.047	0.001	2.740	0.921	5.16E-06	170	1.02E-06	11
Fe Band	0.044	2.546	4.564	0.002	2.350	1.447	3.42E-06	10	1.51E-06	6
Weathering Rind	0.140	2.301	3.461	0.001	2.470	0.876	5.59E-06	4	4.14E-06	4

Table 3.07: Table of calculated retardation factors treating the rock as a porous media and a fracture network.

Chapter 4

Field Scale Tracer Tests and Channel Imaging

Introduction

Tracer tests in fractured rocks are commonly conducted over large scales or with the aid of borehole packers. Transport properties evaluated include advection, dispersion, diffusion, and convection, but there are inconsistencies in the interpretation of tracer test data. Long tailing has been explained by Becker and Shapiro (1998) as an advection-dominated process, while Zimmerman et al. (2002) explained long tails as a result of sorption and desorption. Diffusion of solute from the fracture into the matrix has been discussed as a controlling factor at Äspö in SE Sweden (Mazurek et al. 2003) and Lindau in The Black Forest, Germany (Himmelsbach et al. 1998). To explain tracer behavior, computer models are used to match mathematical curves to tracer test data collected in the field.

Field scale tracer tests were conducted in Wudina and Minnipa, South Australia, and Burnet County, Texas. The tests address the questions: how do fracture skins affect transport properties and what other environmental factors affect transport through single fractures? To address the question, several factors are considered: 1) identifying a single fracture, 2) transport properties of the rock, 3) tracer type, and 4) sampling method. From the collected field data, numerical techniques evaluate transport properties measured in the laboratory.

Isolating a single fracture on bornhardts can be done by using sheeting joints.

Fracturing of granite is notable in the form of sheeting joints and if intersecting vertical fractures are identified by visual inspection around the slab. Sheeting joints can be easily accessed from the surface. Abandoned granite quarries allowed access to potential granite slabs so drilling injection points would be of little concern.

A suite of samples were collected in the field to measure porosity, retardation, and diffusion coefficients in the laboratory. In the field, the fracture selected for the tracer test is represented by the hand sample of rock matrix and fracture skins.

Determining appropriate tracers for a tracer test can be a complex decision. The first consideration is the use of conservative or reactive tracers. D'Alessandro (1997) and Wood et al. (1990) concluded that even conservative tracers may not act conservatively (i.e., Cl^- or Br^-) when intergranular microporosity is significant. Florescent dyes have been used as a conservative tracer on a large scale. McKay et al. (2000) found that colloid tracers were transported up to 500 times faster than He, Ne, and Rhodamine WT. Polystyrene microspheres are also a common nonreactive tracer, but Becker (2003) notes buoyancy problems and microspheres can be filtered because of the physical size of the spheres.

Physical size of multiple tracers and the size of the void space through which they travel should be considered. Brusseau (1993) found that in porous media, grain size controlled hydrodynamic dispersion and multiple tracer sizes would yield similar dispersion results. For aggregated soils, different sized tracers should not be used in simulations with different dispersivities because transport can also be controlled by diffusion. Despite how tracer is transported, in order to evaluate effects of retardation, a suite with different molecular sizes and affinity for reaction are needed. Tracers selected for small scale tracer tests are NaCl and CsBr. These tracers provide use a reactive tracer in Cs^+ and a suite of conservative constituents to characterize transport through a single fracture.

Tracer Test – Wudina, South Australia

Introduction

Two suitable granite slabs were selected in Calca Granite from the Eyre Peninsula. The first is at Mount Wudina and the second in the floor of the Minnipa quarry (Figure 4.01). Restrictions on sampling or drilling injection holes existed at Mount Wudina. For this reason, the slab selected needed to be separated from the dome at the top and bottom of the slab. This allows access to the fracture for injection and sampling.

Mount Wudina is a bornhart with no quarry; this required that water be transported to the injection site in drums. Tracer is injected into the fracture on the up-gradient end of the fracture by carboy (Figure 4.02). The length of the fracture from injection to outlet is 11.6m and fluid flow velocity is 3.3 m min^{-1}. At the Wudina site, two tracer tests were conducted. The first test used grab samples to measure cation (Na^+ and Cs^+) concentrations from two catchments constructed to sample from the two major channels discharging form the fracture. A third sample point was constructed down slope to sample concentrations for total discharge from the fracture (Figure 4.03). Conductivity was also periodically measured throughout the test at sample point three. For the second tracer test only NaCl is injected and tracer breakthrough was monitored using specific conductance (SC).

The first test used a NaCl and CsBr cocktail and lasted 46.1 minutes. 18 grab samples were taken on a 30-second interval from sample point 1 and 39 samples were taken at sample point 3. In the initial design sample point 2 was located at a channel providing enough flow to sample. During the early stages of the test discharge at point 2 decreased below reasonable sampling volume and sampling was abandoned. The remaining bottles were allotted to sample point 3. Sample point 3 is a total accumulation point for total discharge from the fracture. Data from this point represent the average tracer breakthrough for the fracture. Simultaneously, SC was measured at point 3.

The second test at Mount Wudina was conducted using only NaCl and the test lasted 40.5 minutes. Monitoring tracer breakthrough was done using a SC probe taking measurements every 15 seconds. Measurements were only taken at sample point 3.

Results and Discussion

The first tracer test measured breakthrough curves of Cs^+, Na^+, and SC discharging from the fracture. The second test only measured conductivity discharging from the fracture. Fluid discharge from the fracture was concentrated in two dominant flow channels with multiple smaller rivulets. Sample collection points were established at the two dominant channels (sample points 1 and 2) and a third (sample point 3) was established at a central catchment built of modeling clay. The funnel system collecting water below the fracture discharge was designed to sample a tracer breakthrough that would represent the mean for the entire fracture.

Discharge at sample point 2 decreased to below what could be sampled in a reasonable time shortly after the first test began. For this reason sample point 2 was abandoned yielding no breakthrough curve. Plotting concentration vs. time for sample point 1 shows a traditional S shaped tailing curve from a pulse injection of Na^+ and Cs^+ (Figure 4.04). First arrival of the curve was missed, though high velocity provides a sharp rise in concentration before the curve peaks then declines. On the declining slope of the curve both conservative and reactive tracers show a rise in concentration. This can be explained by back diffusion from the granite matrix or from stagnant zones in the fracture. At the end of the back-diffusion portion of the curve Cs^+ concentration approaches the Na^+ concentration suggesting adsorption of Cs^+ is occurring in the test. Desorption can be seen at about 4 minutes in the form of slightly rising Cs^+ concentration into the tail of the curve. As desorption continues the intensity decreases making Cs^+ concentration approach the conservative Na^+ concentration. Throughout the experiment reactive Cs^+ concentrations mimic conservative Na^+ concentrations, suggesting time for significant sorption to occur is too short in the tracer test.

Sample point 3 (Figure 4.05) represents the mean tracer breakthrough for the fracture. By funneling all discharge to a central collection point, incorporation of all channels and rivulets can be measured. Most notable in the breakthrough curve is the higher concentration of Na^+ than reactive Cs^+ approaching the peak. On the down-slope of the curve, in about the same location as the desorption concentration rise from sample point 1, a second peak appears. This is similar to the bimodal and multimodal peaks caused by channeling of solute discussed by Tsang and Neretnieks, (1998). In this case, I suggest the bimodal peak is a combination of channeling and back diffusion.

Through the tail of the breakthrough curve, from sample point 3, separation between the Na^+ and Cs^+ curves can be seen. Desorption and continuing back diffusion could explain the concentration separation, but for the most part concentrations mimic each other. Effects of adsorption on transport through the fracture can be seen in both breakthrough curves with overall significance being minimal. This is primarily due to the short duration of tracer test run and lack of total saturation.

Also, measured at sample point 3 during the first tracer test is SC (Figure 4.06). SC measurements are not limited by the number of samples that can be taken. For this reason the duration of the tracer test monitored by SC is increased to 41.1 minutes. The increased time of the tracer test shows longer tailing that is traditional in tracer breakthrough curves. If grab samples were taken for a longer duration, it would be expected that Na^+ and Cs^+ concentrations would converge and continue to decline in a similar profile to that shown in the SC curve.

The second tracer test conducted at Mt. Wudina used only NaCl as a tracer and monitored SC change at sample point 3 (Figure 4.07). Tracer breakthrough is characterized by rapid arrival with a steep front slope. At the peak of the curve the bimodal peak can be seen. Again, this is contributed to the combination of channeling and backdiffusion. From the peak down the falling limb the curve is linear for the greatest portion of the curve. Linearity in the tracer breakthrough is caused by mixing of tracer from multiple channels and rivulets at the sampling point. After 20 minutes the breakthrough curve drops rapidly and continues at low concentration for the duration of the test. The rapid decline in SC is caused by widening of the funnel outlet to reduce clogging. The effects of tracer mixing are demonstrated and the bimodal distribution occurs at the same time as Figure 4.05. This gives incite into the effect of tracer mixing within a fracture and shows the bimodal distribution is repeatable at the site.

Flow and Transport Properties

Determining flow and transport properties from the tracer breakthrough curves provides estimates that cannot be determined in the laboratory. In order to characterize transport through a fracture, free water diffusion and hydrodynamic dispersion need to be delineated. Dispersion is a function of fluid flow in the fracture and requires knowledge of fluid velocity and hydraulic aperture from the fracture. Quantification of these parameters can be done from tracer test data.

Mean flow velocity is determined from known distances from injection to discharge and time extrapolated from the concentration peaks of the SC tracer breakthrough curve (Figure 4.07). The total length of the fracture to sample point 3 is 13.6 m with a travel time of 4.25 minutes. The mean flow velocity for sample point 3 is 3.2 m min^{-1}. From all the breakthrough curves for the site, the peak is better constrained for the SC data during the second tracer test (Figure 4.07).

From the mean velocity, the hydraulic aperture is estimated at 0.056 cm. The aperture measured in the field from the exposed fracture is 0.05 cm. Correlation between the hydraulic and measured aperture is good and suggests little aperture variation through the fracture.

Diffusion through the fracture is simply molecular diffusion (D_m), which is determined by the Stokes-Einstein equation

$$D_m(l) = \frac{\kappa T}{3\pi\mu d} . \tag{4.1}$$

Here, κ is Boltzmann's constant ($1.38805\text{x}10^{-23}$ J K^{-1}), T is absolute temperature (K), μ is dynamic viscosity (kg m^{-1} s^{-1}), and d is the molecular diameter of the diffusing ion (m). The free water diffusion coefficient for Na^+ is 2.55×10^{-9} m^2 s^{-1} and for Cs^+ the free water diffusion coefficient is 1.81×10^{-9} m^2 s^{-1}. It is expected that the actual free water diffusion coefficient for Na^+ to approach that of Cs^+ when the hydrated radius is considered. In most models the diffusion component in a fracture is incorporated into a hydrodynamic dispersion coefficient (D) (Bear, 1972) that is defined as the sum of the mechanical dispersion and apparent molecular diffusion coefficient.

The hydrodynamic dispersion can be estimated from the advection-dispersion equation

$$\frac{\partial C}{\partial t} + v\frac{\partial C}{\partial x} = D\frac{\partial^2 C}{\partial x^2} . \tag{4.2}$$

Solutions to the partial differential equation depend upon the initial and boundary conditions. Equation 4.2 is solved using the initial condition c(x,0)=0 and the outlet boundary conditions of infinite length with a degrading concentration gradient at infinity. The possible inlet boundary conditions are:

1) constant concentration;
2) well mixed source with constant flux; and
3) constant rate allowing advection upstream and downstream.

These and other solutions for the advection dispersion equation have been compiled in Charbeneau (2000) and van Genuchten and Alves (1982).

The inlet boundary condition that applies to the site condition is the constant mass injection rate allowing advection upstream and downstream. Solving Equation 4.2 gives:

$$\frac{C}{C_o} = \frac{1}{2}\left(erfc\left(\frac{x - vt}{\sqrt{4Dt}}\right) - \exp\left(\frac{xv}{D}\right) erfc\left(\frac{x + vt}{\sqrt{4Dt}}\right)\right). \qquad (4.3)$$

Here C is concentration, C_o is the initial concentration, x (m) is the distance of transport, v (m s^{-1}) is flow velocity, t (s) is time, D (m^2 s^{-1}) is hydrodynamic dispersion, and the function erfc is the complimentary error function.

In order to model advection-dispersion, the data must show the rising limb of the breakthrough curve. For this reason the SC data is converted into total dissolved solids (TDS) using TDS = 0.67 * SC (µS cm^{-1}) and normalized to the total concentration of NaCl introduced as a tracer. Using Equation 4.3 to model the TDS data for tests 1 and 2 enables the hydrodynamic dispersion coefficient to be estimated (Figure 4.08). Data collected during the run 2 constrains the breakthrough curve better than run 1. Advection dispersion matches the breakthrough curve of run 1 giving a D = 25 m^2 min^{-1} with R = 1. Matching the breakthrough front of run 2, gives a best fit with D = 6 m^2 min^{-1}. The curve match for run 2 overestimates the peak of the curve and the front of the rising limb. Advection-dispersion not being able to match breakthrough curves for fracture systems has been well documented (Tsang and Neretnieks, 1998) and is contributed to channeling.

Estimating longitudinal dispersion (α_L) within the fracture is done using the relationship:

$$D = D_m + \alpha_L v \tag{4.4}$$

Solving for α_L using D form the TDS data above gives α_L = 7.6 m for run 1 and α_L = 1.8 m for run 2. These estimates may overestimate longitudinal dispersion in a fracture because estimates of D using curve matching are overestimated.

The trend for the dispersion coefficients can be explained by the flow regime being a form of sheet flow near the injection point and breaking into rivulet flow prior to discharge from the fracture. Dispersion of an individual rivulet is minimal, but the mean of all the rivulets discharging from the fracture would be considerable. For the tests, flow and transport through the fracture is channeled into rivulets, making the use of saturated hydrodynamic dispersion coefficients questionable.

Tracer Test – Minnipa, South Australia

Introduction

Minnipa Hill is a bornhardt of Calca granite that is periodically quarried, depending on supply and demand. The quarry floor exposes a horizontal fracture with clay coating fracture skin. Minnipa is documented as a site under compressional stress (Twidale and Bourne, 2000; and Twidale et al., 1996). Evidence of compressional stress includes A-tents and reverse faults. In the floor of the quarry, four holes where drilled spaced 1 m apart to inject water and tracer. At the lower end of the slab, exposure was not available. Holes where drilled for sampling during the tracer test but after sufficient depth was reached no fracture was intersected. Water was injected into the fracture to determine if discharge occurred along the slabs left side where the fracture is exposed. Discharge occurred in three locations, the first two are at the slabs surface connected by small vertical fractures and the third at the lower left fracture exposure (Figure 4.09).

Water for the tracer test was pumped from the lower quarry excavation into a tanker truck and then pumped from the truck to the fracture injection ports. Standpipes where constructed to establish constant head and flow was regulated by a shutoff valve at each standpipe (Figure 4.10). One pulse injected tracer test was conducted at the site using a NaCl solution and sampled using grab samples on a 30 second interval for 16 minutes.

Results and Discussion

Sample locations were placed at three discharge locations, two located on top of the slab and the third on the lower left side of the slab. The lower collection point represents the mean breakthrough for the fracture. Conceptually, flow through the fracture is sheet flow from injection to the fracture pinch-out (right and lower portion of the slab) were pressure builds and forces discharge through small fractures connecting to the surface of the slab (Figure 4.09).

Flow and transport is interpreted to follow a single channel, therefore breakthrough curves of Na^+ from all sample points are plotted on a single plot (Figure 4.11). Sample point 1 is located closest to the injection point, followed by sample point 2, and finally the furthest away sample point 3. This shows the evolution of tracer transport with distance along a flow path. Model prediction suggests curves for pulse injections become more dispersed with a lower peak (Garner and Sharp, 2004 and Becker and Shapiro, 2003). The evolution of Na^+ transport appears to follow model prediction.

The prominent “hip” on the rising limb of the curves is assumed to be a function of channeling. Sample points 1 and 2 show very rapid breakthrough fronts contributing to high flow velocities, lower dispersion, less mixing, and relatively short distances for sorption to occur. At sample point 3 the breakthrough curve becomes wider showing effects of dispersion, matrix diffusion, retardation, and mixing from contributing sheet flow. Tracer breakthrough for the site is characterized by rapid transport with detectable effects from tracer-rock interactions and channeling.

Flow and Transport Properties

The time component for the average linear velocities is estimated using the tracer breakthrough peak. Duration for the tracer peaks to breakthrough are 3 minutes over a traveled distance of 1.5 meters for sample point 1, 3.5 minutes over 4.5 meters for sample point 2, and 4 minutes over 6.7 meters for sample point 3. Mean flow velocity calculated for the three discharge points are 0.5 m min^{-1} at point 1, 1.3 m min^{-1} at point 2, and 1.7 m min^{-1} at point 3.

The mean velocity for the horizontal fracture tracer is injected into is 1.7 m min^{-1}. Of the three sample points, number 3 is the only one collected directly from the horizontal fracture. Sample points 1 and 2 are sampled from vertical fractures connecting the main horizontal with the slab surface. Because the vertical fractures were not detectible until fluid was pumped into the system flow velocities through the vertical fractures is interpreted to be much slower.

Using the cubic law, hydraulic apertures are estimated 0.024 cm at sample point 1, 0.039 cm at sample point 2, and 0.045 cm at sample point 3. This supports the interpretation of the horizontal fracture being more conductive than the combination of horizontal and connecting vertical fractures.

Molecular diffusion of Na^+ is calculated using equation (4.1) and is estimated to be 2.55 x 10^{-9} m^2 sec^{-1}. Estimating D using equation (4.3) is partially successful (Figure 4.12). At sample point 1 the “hip” on the rising limb of the curve is ignored. Data from the peak through the falling limb are used to curve match. Advection dispersion undershoots the peak concentration and overestimates the front at the beginning of the tail. Na^+ is a conservative tracer so R = 1 for all analyses and for best fit at sample point 1 $D = 0.02\ m^2\ min^{-1}$. At sample point 2, advection dispersion accurately predicts the curve from the peak through the tail using $D = 0.1\ m^2\ min^{-1}$. The falling limb and the tail of sample point 3 are accurately predicted using $D = 0.3\ m^2\ min^{-1}$. Advection dispersion also fits the data towards the peak of the curve on the rising limb but overshoots the peak. Using the hydrodynamic dispersion estimates from the best fit curves to calculate longitudinal dispersion gives α_L equal to 0.04 m, 0.08 m, and 0.2 m.

Given the inability to model both the rising and falling limb of the breakthrough curves to estimate α_L using D from the curve matching is questionable. Brusseau (1993) showed through field and laboratory analyses of sediments that heterogeneity controlled hydrodynamic dispersion. Thus, minimal heterogeneity exists in this fracture suggesting expected dispersivities to be low. Comparing the α_L values for the Minnipa Hill quarry shows the trend using advection dispersion increases with distance. In theory, as a slug gets further from the source dispersion increases. Therefore, the α_L values determined using advection-dispersion are believed to be accurate.

Tracer Test - Burnet County, Texas

Introduction

A suitable granite slab was selected in Town Mountain Granite from the Llano uplift. The *insitu* slab was inspected for intersecting vertical fractures and the sheeting joint could be determined to continue to a suitable injection location. Once the slab was selected a grid of holes were drilled to intersect the fracture used a hammer drill. The drill holes varied in depth from 45.72 to 91.44 cm and are 2.54 cm in diameter. Eight holes are drilled in a grid of four columns by two rows. Spacing between the columns is 1 m and spacing between the rows is 2 m.

Source water for the tracer test was pumped from the abandoned quarry floor. Water was pumped into a 3.79 m^3 tank where water was then transferred by pump to the fracture. By using the tank as intermediate storage, constant head could be achieved. Water was pumped into the fracture through two of the drill holes in the upper right corner of the grid. The initial plan called for injection into all four holes along the top line of the grid. Constraints on the volume of water that could be transferred to the fracture prevented the use of four holes. Volumes of water injected are monitored using flow meters. In order to achieve roughly equal parts water being injected into the fracture a closed loop was designed. The tracer injection port was located on the upper right drill hole injection line coming from the closed loop. This meter location optimized the length of the tracer run and prevented tracer from backing into the loop and being injected into other injection holes.

Three tracer tests were run in Burnet County Texas: 1) pulse NaCl injection, 2) pulse CsBr injection, and 3) steady state NaCl injection. Pulse injections are sampled on a 15-second interval. Sample locations are selected by locating fluid channels that provide enough fluid to fill a 15 ml bottle in 15 seconds. Field preparation of samples consisted of filtering all samples with a 0.45um pore filter. Cation samples are acidified and anions are unacidified. Laboratory analyses of cations are done using an Agilent

7500ce ICP-MS. Anion analyses are done using a Dionex ICS 2000.

Pulse injections, are introduced by a ten liter Marriotte bottle gravity feed into the injection port at a rate of 1.15 L min^{-1}. The steady state injection is from a fifty five gallon drum equipped with a bilge pump used to inject NaCl solution at a rate of 6.5 L min^{-1}. Tracer injection methods are used for two separate goals. The first is to inject a pulse of NaCl and CsBr to evaluate the response of conservative and reactive ions. The second is to inject a constant rate of solute for a duration that would allow GPR imaging of the slab.

Results and Discussion

Tracer test samples from Burnet County were analyzed for Cs^+ and Cl^- to evaluate reactive and conservative transport through the fracture. Water, without tracer, injected into the fracture resulted in three significant streams of water discharging from the fracture. These three discharge points A, B, and C (Figure 4.13) are the sample locations for the succession of tests.

Results from sample point A shows little change in concentration when plotting normalized concentration verses time in minutes (Figure 4.14). Results for sample point B show the highest relative concentrations for both reactive Cs^+ and conservative Cl^-. At sample point C, concentrations of both tracers are slightly lower than concentrations at point B. Cl^- concentration is consistently higher and noisier than Cs^+ for all samples points. This increase in concentration is contributed to the background water used to inject into the fracture.

The higher tracer concentrations at point B and lower concentrations at A and C suggest dispersion of tracer within the fracture among the flow rivulets. Also showing dispersion between the channels, the breakthrough curves at sample point C for Cl^- and Cs^+ tracers are wider compared to the breakthrough curves at sample point B. Dispersion is commonly discussed in porous media but methods for combining effects of dispersion with channeling have not been established. Tsang and Neretnieks (1998) conclude that channeling is determined to be the cause of data variation from model prediction in fractured systems.

The use of reactive Cs^+ and conservative Cl^- in the tracer test design shows retardation effects during a small field scale tracer test. By comparing the rising limb of the Cl^- and Cs^+ breakthrough curves a change in slope of the curve can be seen. The effect of retardation is to cause reactive concentrations on the rising limb to advance slower than conservative tracer.

Focusing on sample points B and C, the shape of the breakthrough curve after the tracer peak shows a concentration rise at about 5 minutes for both sample points and both conservative and reactive tracers. Bimodal distribution of tracer breakthrough curves has been contributed to as effects of channeling in the fracture (Abelin et al., 1988 and 1990). Reactive Cs^+ tracer at point B also shows a faster rising limb than the Cs^+ breakthrough at point C. The greater rising limb slope at point B indicates faster plume arrival caused by either shorter travel path to the collection point or faster flow to the collection point.

The conservative Cl^- tracer also shows the second concentration spike on the falling limb (Figure 4.14, Point C). Arrival time of the second spike for the Cs^+ tracer appears to be uniform at about 5 minutes. The arrival time of the second spike for the Cl^- tracer occurs before the 5 minute mark at sample point B and after the 5 minute mark at sample point C. Since reactive and conservative tracers are traveling along the same path, it would be expected that Cl^- spike prior to the Cs^+. The expectation is that Cs^+ would have a greater affinity for adsorption to the fracture surface allowing Cl^- to breakthrough quicker than the reacting Cs^+, as shown at sample point B.

By smoothing the data using a moving 3-point averaging filter (Figure 4.15) the Cl^- concentrations can be more accurately assessed. The second Cl^- peaks decrease by using the filter, but the overall rise in concentration at the lower portion of the falling limb is greater than expected. At sample point B the anomalous portion of the breakthrough curve lies between 5 and 12 minutes and for sample point C the region lies between 5 and 15 minutes. These portions of the curve are interpreted as effects of tracer channeling and back-diffusion of tracer from matrix or stagnant zones into the fracture.

Flow and Transport Properties

The Burnet County pulse tracer test results are achieved by conducting two tracer tests. The first test injected a slug of NaCl and the second test injected a slug of CsBr. From the grab samples, Cl^- and Cs^+ were measured. Average linear velocity is calculated using the Cl^- and Cs^+ peaks of the breakthrough curves for each of the three sample locations. Distances from injection to sample points for locations A, B, and C are 6.4 m, 6.0 m, and 5.6 m. Cs^+ peak concentrations occur at 4.25 min, 2.75 min, and 3.25 min for locations A, B, and C. Average linear velocities of Cs^+ for the three locations in order are

1.5 m min^{-1}, 2.18 m min^{-1}, and 1.71 m min^{-1}. Taking the mean of the three velocities gives an average velocity for the main channels of 1.80 m min^{-1}. For the Cl^- peaks the distance remains the same but the peak concentrations occurred at 3.5 min, 3 min, and 3 min, respectively. This gives average linear velocities for the three sample points of 1.83 m min^{-1}, 2.00 m min^{-1}, and 1.86 m min^{-1} with an average for the three velocities of 1.89 m min^{-1}. In total, Cl^- traveled slightly faster through the fracture than Cs^+.

In the field fracture apertures were measured down boreholes, for the two measurable apertures b = 2.1 cm and b = 3 cm and four apertures are detectable but not measurable. The hydraulic apertures are determined using the cubic law for the conservative Cl^- tracers. Calculated apertures are 0.23 cm, 0.23 cm, and 0.22 cm for points A, B, and C. The difference between field measured and hydraulic apertures comes from variation in asperity not accounted for in field measurements and calculated hydraulic apertures give a mean estimate of aperture. To characterize aperture for the site, large variation exists (<1 mm to 3 cm) in aperture with a mean aperture of 0.23 cm.

Using the advection-dispersion equation to estimate hydrodynamic dispersion is not done using sample point A because a reasonable curve does not exist. Modeling the Cl^- peaks for sample points B and C is partially successful (Figure 4.16). For both locations the rising limbs and the falling limbs are reasonably predicted. Concentration peaks at both locations are overestimated by the model and the tails are underestimated. Hydrodynamic dispersions for both sample locations are estimated to be 0.3 $\text{m}^2\ \text{min}^{-1}$ when $R = 1$.

Advection dispersion does not fit the Cs^+ data (Figure 4.17). Again, only sample points B and C are considered. The Cs^+ curves are less noisy than the Cl^- making them easier to model but low concentrations proves difficult for accurate prediction. For the data from sample point B, the curve front can be predicted but prediction overestimates concentrations through the peak and tail of the curve. Concentration breakthrough at sample point C cannot be accurately predicted for any region of the curve. Model fits are shown with $D = 0.3\ m^2\ min^{-1}$ and $D = 0.2\ m^2\ min^{-1}$ for sample points B and C. Retardation is a reasonable variable to change for the reactive tracer but curves are best fit using $R = 1$. Determining α_L using the advection dispersion method gives 0.15 m and 0.16 m for the Cl^- data and 0.14 m and 0.12 m for the Cs^+ data.

Channel Mapping Using GPR

Introduction

Variations in tracer test results have been speculated to be caused by channeling in fractured rocks ((Abelin at al., 1988, 1990; Frick et al., 1992; Eikenberg et al.,1994 ; Hadermann and Heer, 1996; and Birgersson et al., 1993). I hypothesize that tracer tests results in the fractured granites are altered by channeling of mass in the subhorizontal fractures. By utilizing ground penetrating radar (GPR), channeling of high conductivity tracer in horizontal sheet fractures can be imaged providing a two dimensional (plan view) of tracer migration. Combining GPR imaging of tracer migration and tracer breakthrough tests the significance of channeling in horizontal fractured rocks. On of the scientific questions about channelized flow is: What are the subsurface fracture dimensions and how do they affect tracer test results? To address this question, GPR imaging and field tracer tests were integrated.

The use of surface geophysical methods can reduce the cost of site characterization by utilizing techniques that provide quick and efficient analysis. Robust models requiring defined channel and fracture geometries would also benefit from such a technique. This project utilizes GPR as a tool that can be applied to field investigations and flow and solute transport simulation work.

Current field and modeling techniques do not provide prediction of channel location between recharge and discharge locations. This study evaluates fracture channel geometry at high resolution for the purpose of characterizing flow and transport variation caused by the channeling phenomena.

Previous Work and Theory

Many significant studies have contributed to our understanding of channelized fracture flow (Tsang and Neretnieks, 1998). Studies that use geophysical techniques may define with more confidence on channeling between injection and discharge points on scales larger than laboratory scale.

Fluid flow through fractures has long been documented on several different scales (Tsang and Neretnieks, 1998). Transport of solutes through a fracture in channels allows inferences about channel location and geometry based on transport flow paths deviating from that inferred from hydraulic gradients alone. Shallow geophysical techniques may permit mapping of channel geometries based on differences in the electrical properties of dry fractures, fractures saturated with water, and fractures transporting electrically conductive solutes. This study maps 2D fracture channels to define accurate transport lengths for modeling and comparing effects of channeled transport on breakthrough curves.

Small scale field experiments suggest flow and transport are highly channelized. Furthermore, flow and transport apertures are different (Abelin et al., 1985). Bourke et al. (1987) found that ~20% of a fracture plane in granitic rocks conducts water. Their conclusions were derived by drilling series of boreholes parallel to fracture planes and measuring flow rates and tracer migration using packer systems. Dipole and radial convergent flow field and tracer tests conducted by Novakowski et al. (1985) and Raven et al. (1988) demonstrated that tracer breakthrough curves are altered when insufficient distance between boreholes and/or high pumping rates are used. Using boreholes to intersect known fracture zones researchers have shown uneven flow and discharge (Abelin at al., 1988, 1990; Frick et al., 1992; Eikenberg et al.,1994 ; Hadermann and Heer, 1996; and Birgersson et al., 1993).

Tracer breakthrough curves have a characteristic shape from channeled flow paths. The curves have been described to have a sharp rise and a long tail with double peak (Frick et al., 1992). Long tailing breakthrough curves are problematic when the advection dispersion equation is fit to the data. Breakthrough curve analyses in the literature have suggested that long tailing is the result of advective transport (Becker and Shapiro, 2003), diffusion and back diffusion from fracture skins (Garner and Sharp, 2004) and sorption (Zimmerman et al., 2002).

Ground penetrating radar (GPR) uses high frequency (10 MHz – 1.5 GHz) electromagnetic waves to image the shallow subsurface. Electromagnetic waves (EM) are transmitted by one antenna, propagate through the subsurface until they are reflected at a boundary and are received by a second antenna. The principles and methodology of GPR are given in detail by Davis and Annan (1989).

The presence of water in the medium has a strong influence on EM wave propagation due to the large electric conductivity value of water compared to most rocks. Therefore, the presence of water in a fracture shows significantly greater amplitudes in EM waves than the presence of air. Also, a negative reflection coefficient is produced as the wave travels from a low dielectric permittivity such as air or granite, to a high dielectric permittivity such as water as shown by Lane et al. (2000). This phenomenon makes GPR a promising tool for remotely imaging channeling of flow.

The utilization of surface GPR has been seldom used to image tracer migration through a single fracture. Tsoflias and Sharp (1998) investigated a fractured dolomite with GPR and were able to identify fractures and diagenetic zones that contained water. The results from Tsoflias and Sharp were ground-truthed with well log data. Day-Lewis et al., (2003) also imaged saline tracer movement through a fracture with time using borehole radar tomography, and Talley et al., (2005) imaged saline tracer movement through a fracture with time using surface ground penetrating radar.

This research differs from previous studies because: 1) the saline tracer is flowing through a fracture that can be partially saturated, 2) a high resolution image of the channel network is obtained with surface GPR, and 3) the flow constrained through a single subhorizontal fracture. The exposed outcrop and shallow depth of the fracture for the study allow visual confirmation that no other significant fractures intersect.

Results and Discussion

Field imaging of an isolated fracture using GPR utilizes the difference in conductivity between different materials. Of interest to this study is the conductivity difference between granite and air, granite and water, as well as the wavelet amplitude intensity difference between water and solution. GPR imaging of the fracture was done in three phases: 1) dry fracture, 2) water wet fracture, and 3) water with solution being injected into the fracture. Data acquisition in three phases allows the dry fracture, water wet, and tracer migration paths to be evaluated independently.

Establishing the fracture plane is done by mapping the phase change of each wavelet measured. At the boundary between granite and water, the wavelet reverses direction and at center of the maximum amplitude marks the fracture boundary. Details of methods for processing the acquired field data are provided by Bonal (2007). Because a narrow aperture allows the wavelets to overlap, obscuring boundary selection, the fracture plane is presented as a relative fracture plane location. Locations of phase change or intensity change is represented by black lines across measurement transects. By outlining areas were the black lines are concentrated the preferred flow pathways can be delineated.

GPR data acquired using a NaCl solution being injected into fracture shows preferential transport pathways trending towards the lower left hand side of the slab

(Figure 4.18). The fracture plane is represented for a 5.5 meter by 5 meter grid portion of the slab. Color variation through the image represents relative elevation in units of meters. Inferred channels are constrained by the black lines that represent high concentration solution and along the lower boundary by grab sample locations. Channels shown represent the major transport pathways. During tracer injection the discharge from the fracture consisted of multiple small rivulets with three dominant rivulets. Because only the three dominant rivulets could be sampled, inference of total discharge would be impossible. This does not degrade the significance of being able to map major transport pathways because the bulk of the mass transported through the fracture is discharging from the three main rivulets.

Determination of the dominant transport channels allows the comparison between the saline solution and water-only data acquisitions. Utilizing the inferred channels from the saline injection tracer, the inferred channels are overlain on the fracture plane with black dashes representing wavelet phase change (Figure 4.19). It is clear that water flows in more directions than implied using a saline solution. The significance of the saline channels is that these are the dominant flow paths in the fracture. Dilute tracer is probably moving in the areas outside the tracer channels but the dilution of tracer decreases the signal difference that is being utilized in processing. This finding explains why Talley et al. (2005) show saline tracer migrating in plumes from a continuous source.

Conclusions

Tracer tests were conducted at three field sites: 1) Mount Wudina, South Australia, 2) Minnipa Hill, South Australia, and 3) Burnet County, Texas. Skin types at the field site are characterized as a thin weathering rind at Mount Wudina and clay coatings from both Minnipa Hill and Burnet County. The clay-coated fractures are different in that Minnipa Hill utilized a quarry floor that provides a more recent outcrop. The fracture at Burnet County is on the side of a bornhardt and has probably been exposed for a much greater time.

Tracer breakthrough curves for all three field sites show characteristics related to channeling. Knowledge that flow is channeled also comes from visible evidence from fracture discharge. Breakthrough curves of conservative and reactive tracers from Wudina and Burnet show effects of retardation. Burnet shows the greatest effect from retardation. Use of the advection-dispersion equation to determine hydrodynamic dispersion shows reasonable fits overall considering matrix diffusion and channeling are not considered in the model. A summary of calculated flow and transport properties is given in Table 4.01.

GPR is shown to be a potentially useful tool for mapping channels in a single granite fracture. Inferred channels from saline solutions indicate the preferred transport pathways within a fracture. Combining the inferred channels with the water-only flow regime shows zones of fluid migration with lower variation in amplitude or phase change. This could be caused by smaller aperture, increased relative elevation, tracer dilution, or eddies.

Effects on transport caused by fracture skins are not obvious at these sites because of short tracer test runs, unsaturated conditions, and high flow velocities. The greatest effect on small scale tracer transport results is channeling.

Figure 4.01: Tracer test site at Mount Wudina, South Australia.

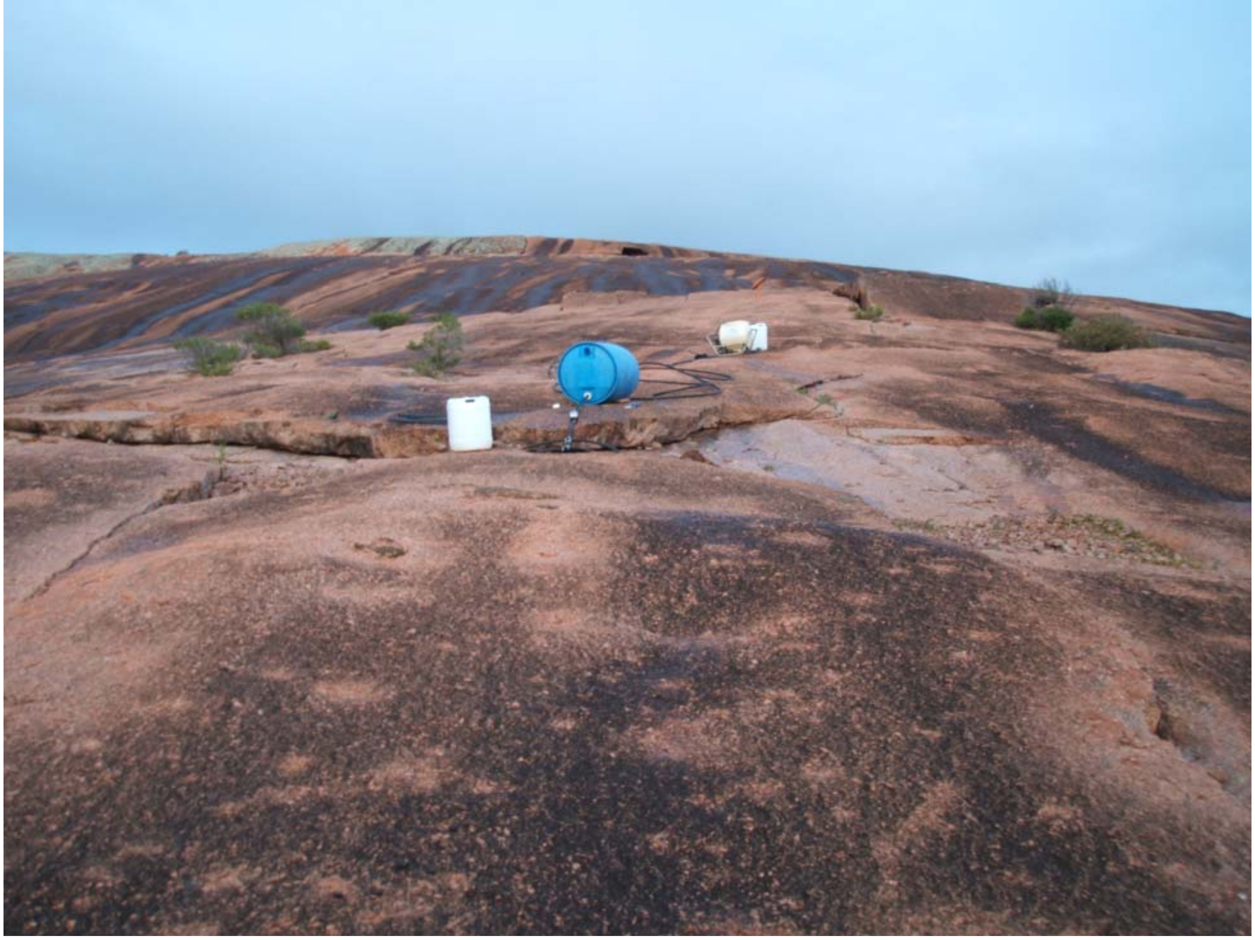

Figure 4.02: At the up-gradient end of the fracture water is injected from a drum and tracer is injected from a carboy at Mount Wudina, South Australia.

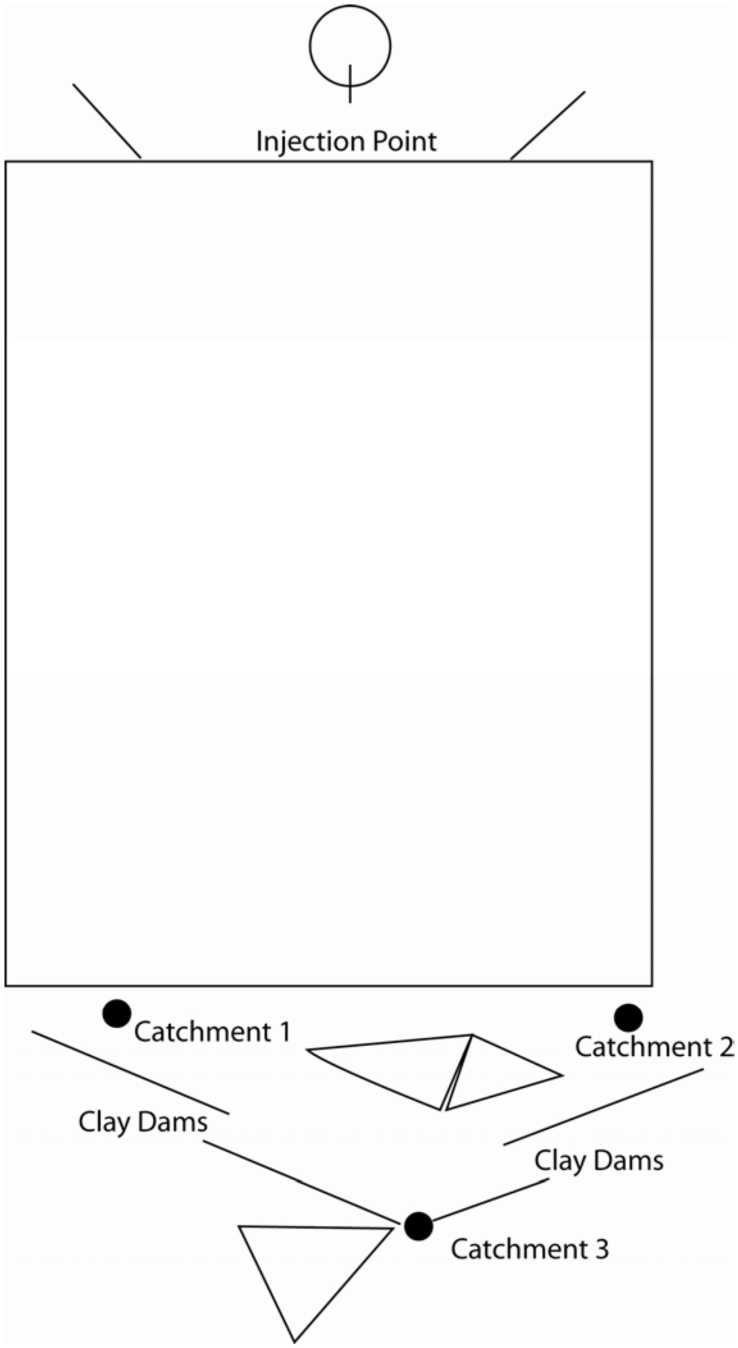

Figure 4.03: Sketch of the injection and sample points at Mt. Wudina. The solid black circles are catchments 1, 2, and 3. The solid lines represent clay dams constructed to divert discharge to collection points.

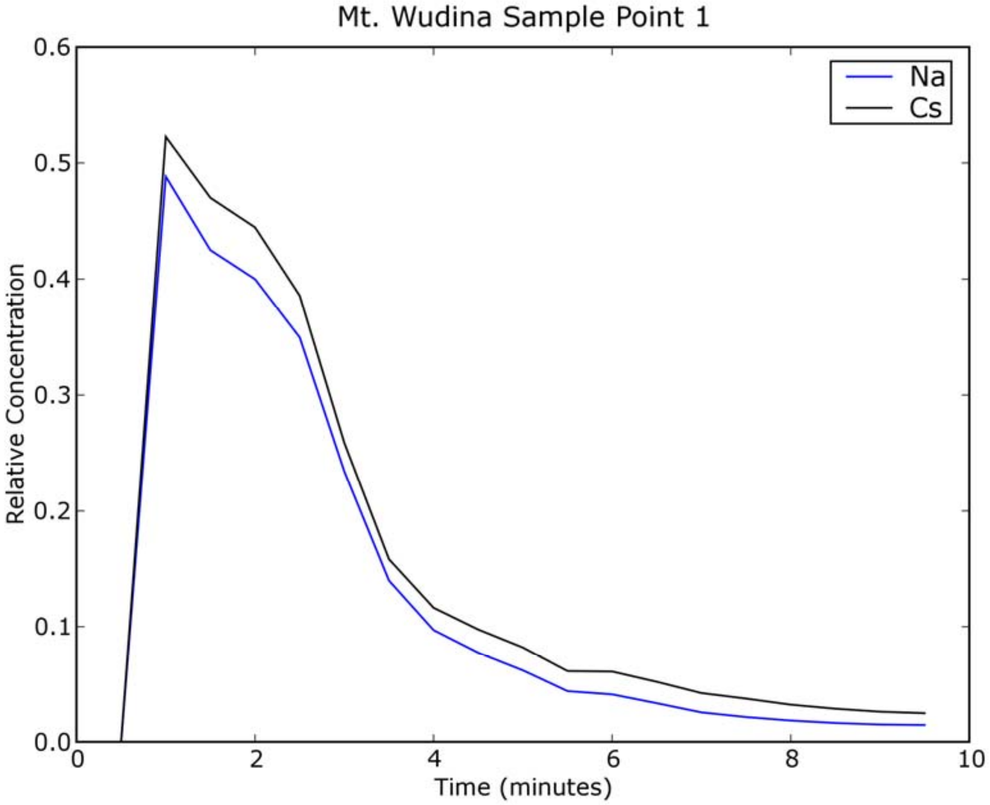

Figure 4.04: Tracer breakthrough curve for Na^+ and Cs^+ grab samples taken at point 1.

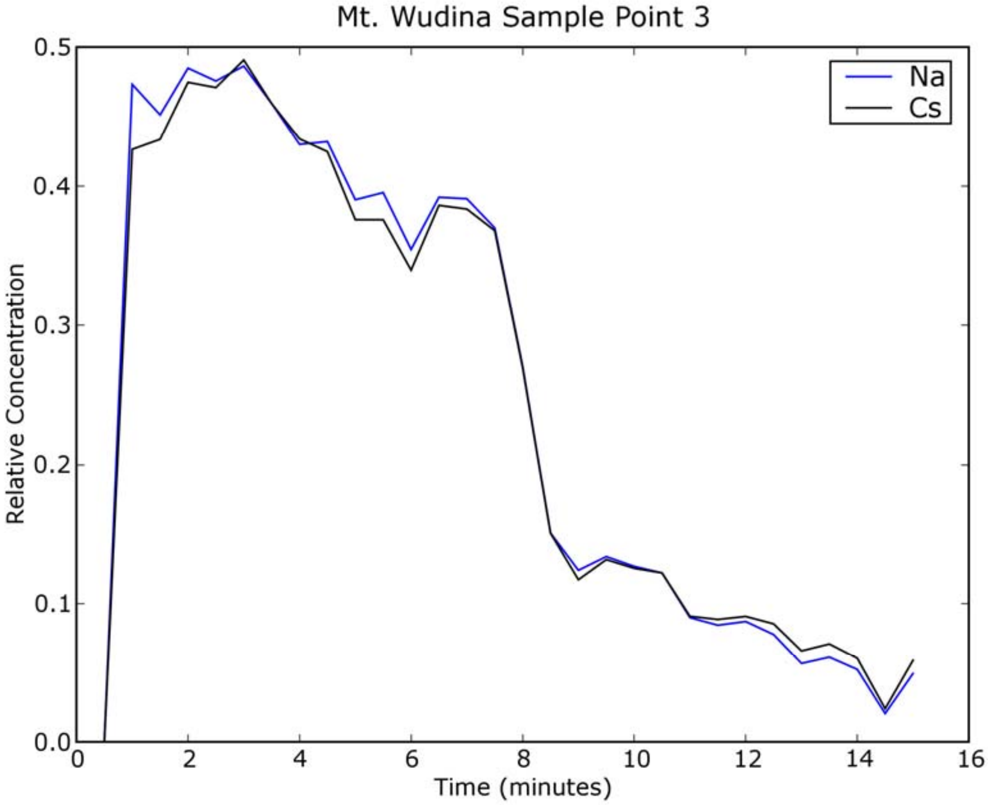

Figure 4.05: Tracer breakthrough curve for Na$^+$ and Cs$^+$ grab samples taken at sample point 3.

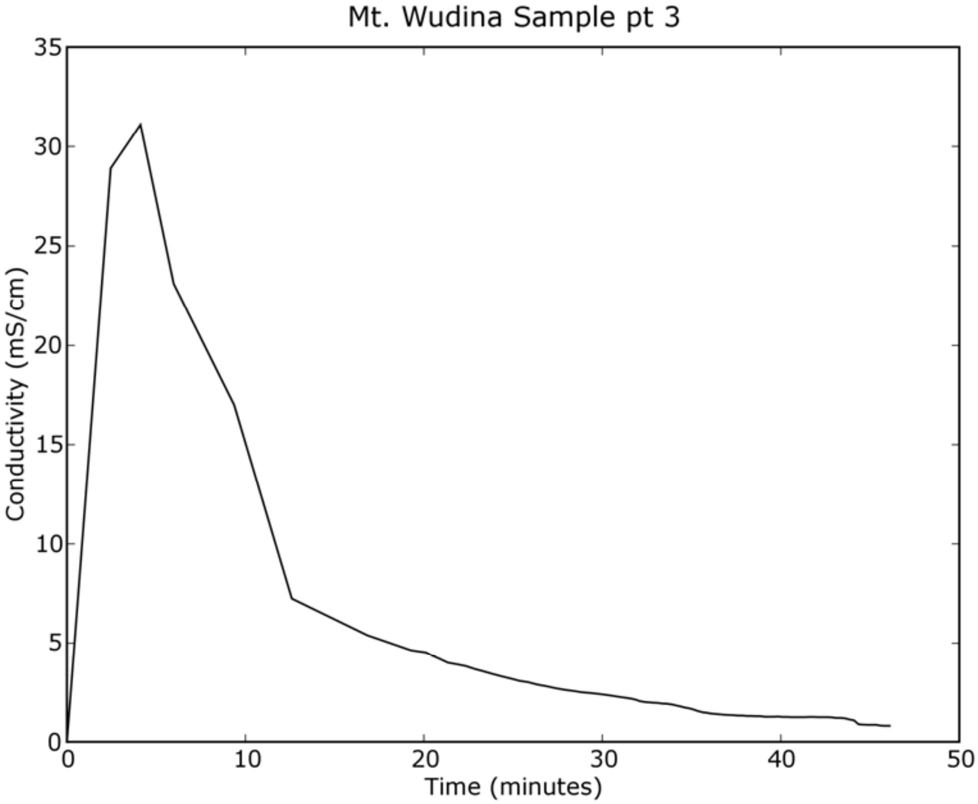

Figure 4.06: Tracer breakthrough curve measuring conductivity at point 3.

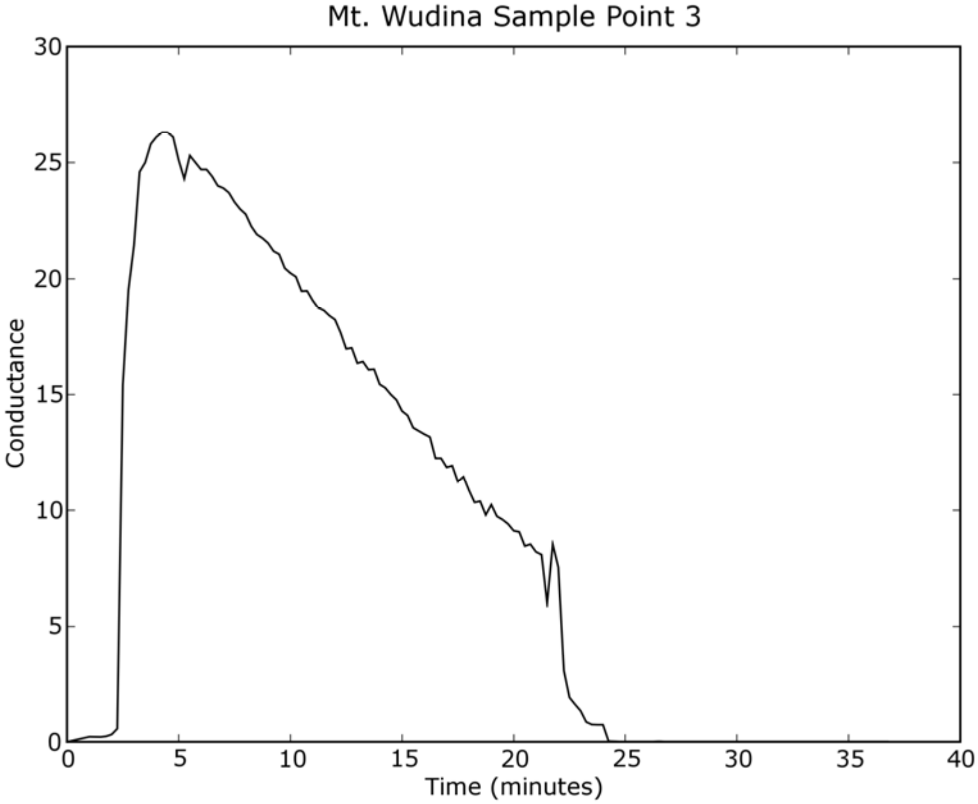

Figure 4.07: Tracer breakthrough curve measuring conductivity at sample point 3 for the second tracer run.

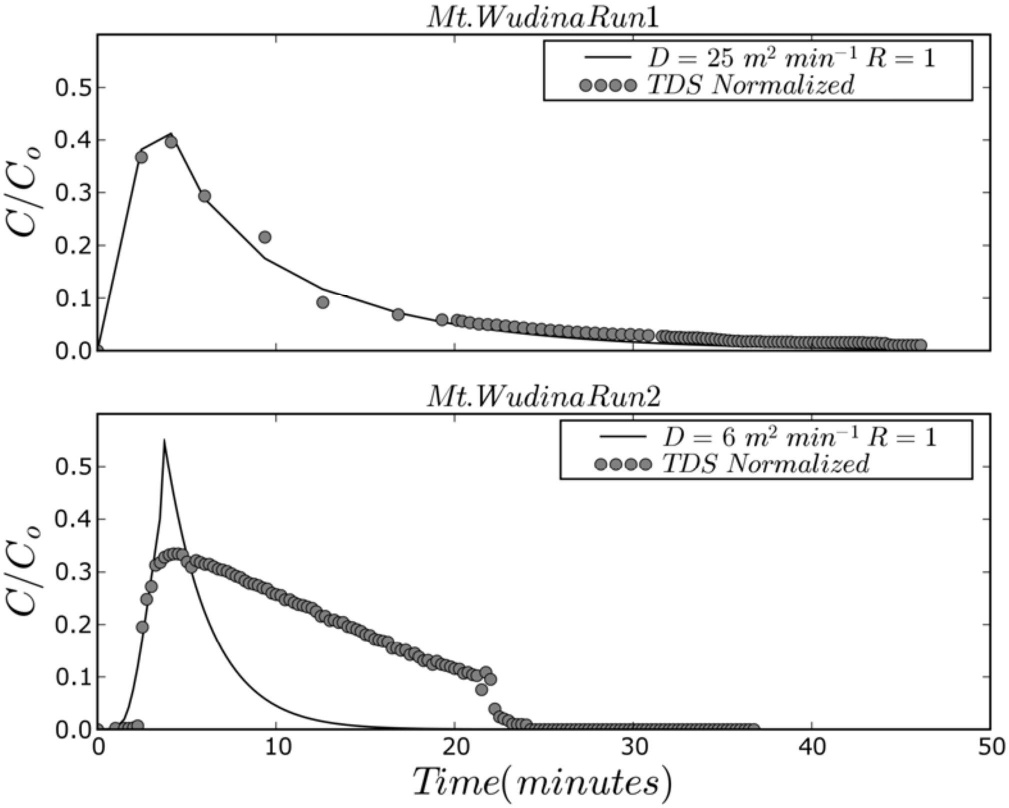

Figure 4.08: Plots of specific conductance data shown as normalized TDS for runs 1 and 2 at Mount Wudina. Solid lines are modeling results form the advection dispersion equation.

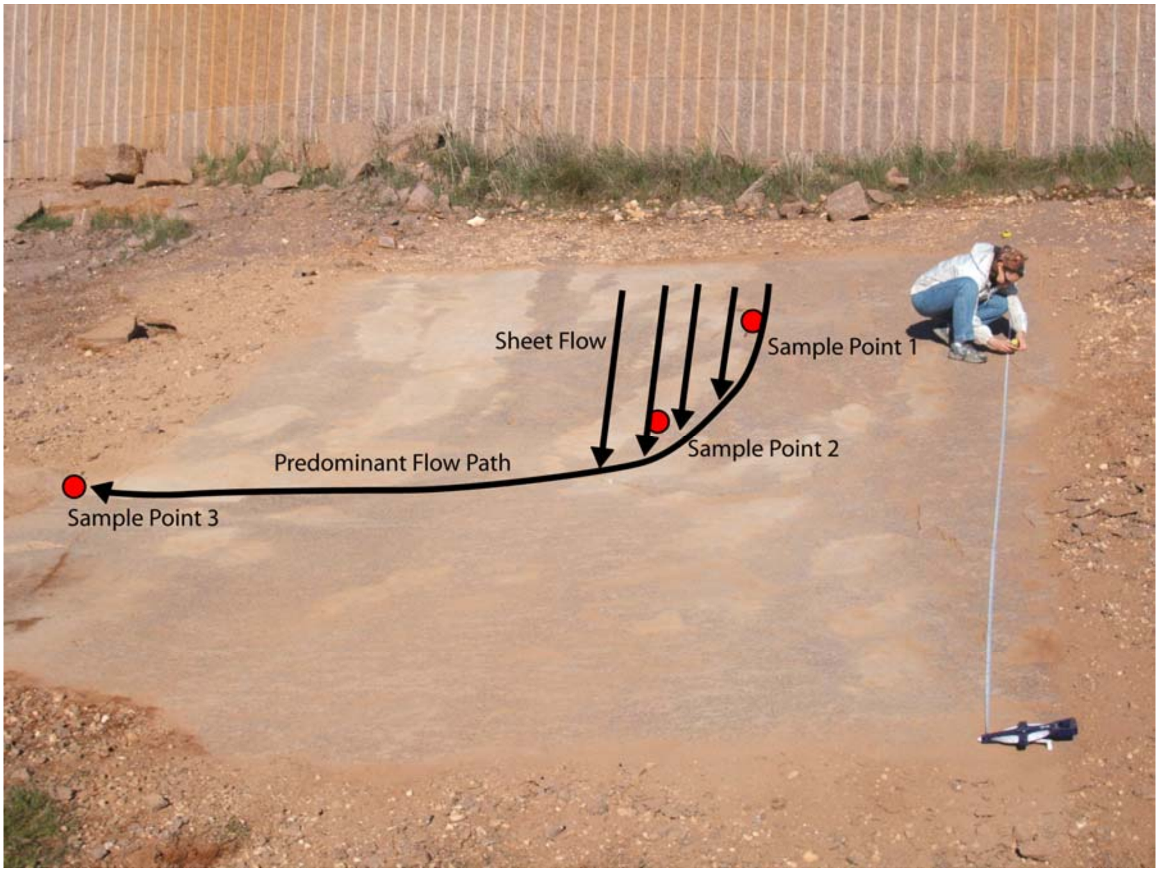

Figure 4.09: Photo of quarry floor at Minnipa Hill with black lines showing interpreted flow paths and red dots showing three sample points.

Figure 4.10: Stand pipes affixed into three pre-drilled injection points at the Minnipa Hill quarry.

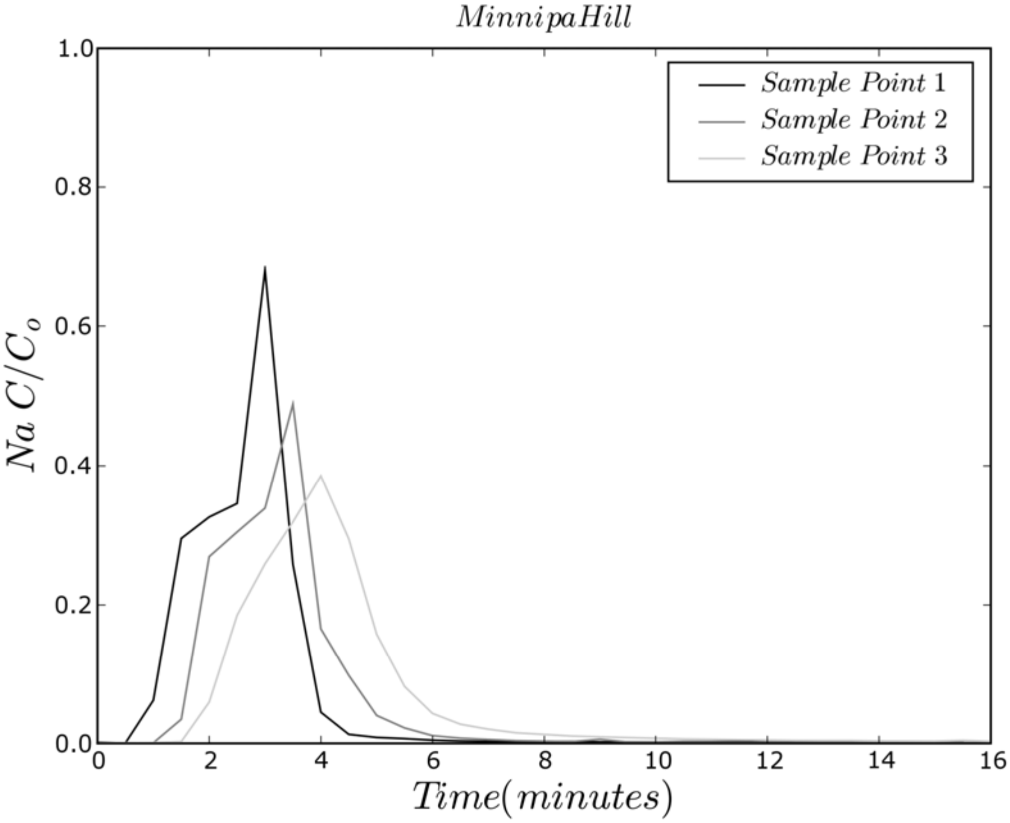

Figure 4.11: Tracer test breakthrough curves sampled from increasingly greater distances from the injection point form the Minnipa Hill quarry.

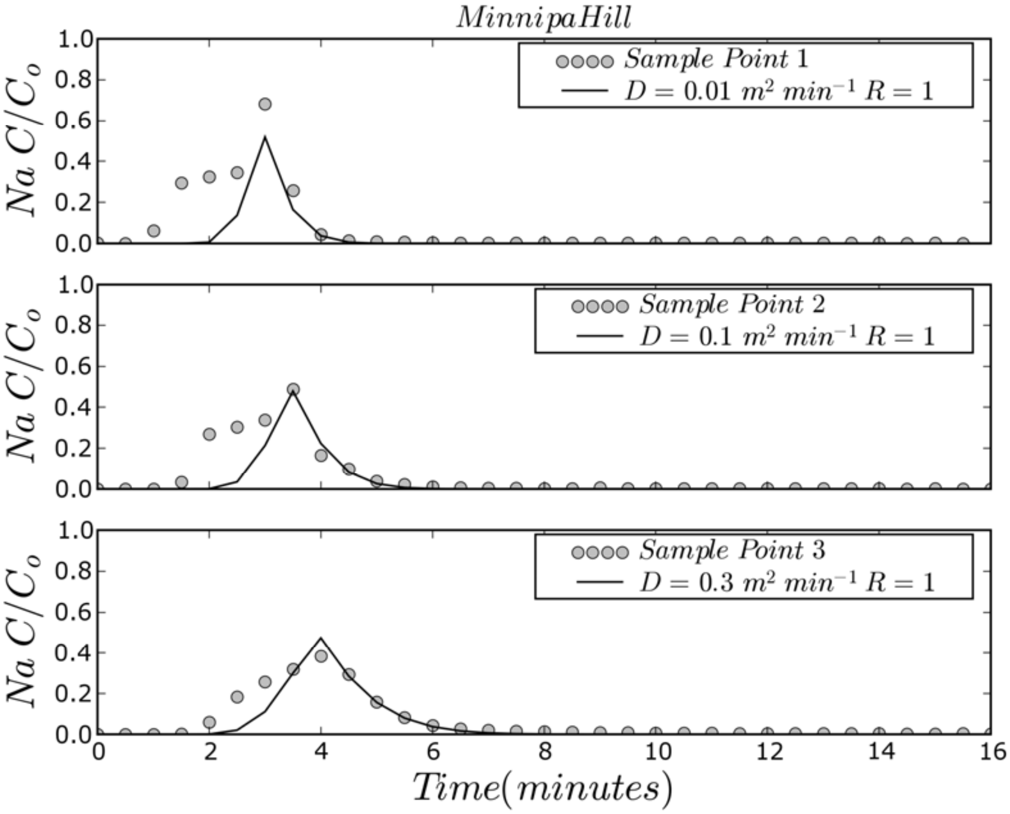

Figure 4.12: Model fit to Na^{+} data from Minnipa Hill using the advection-dispersion equation.

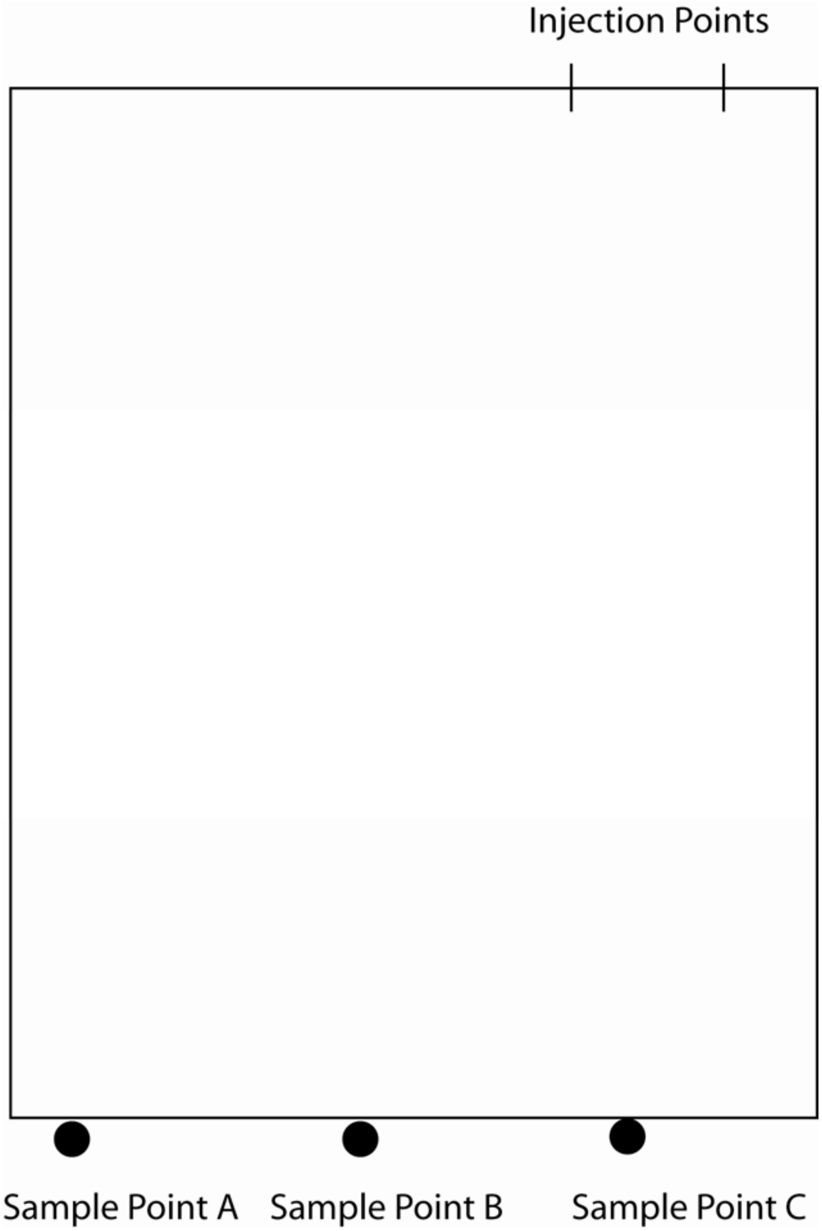

Figure 4.13: Line sketch of the Burnet County field site with fracture discharging background water.

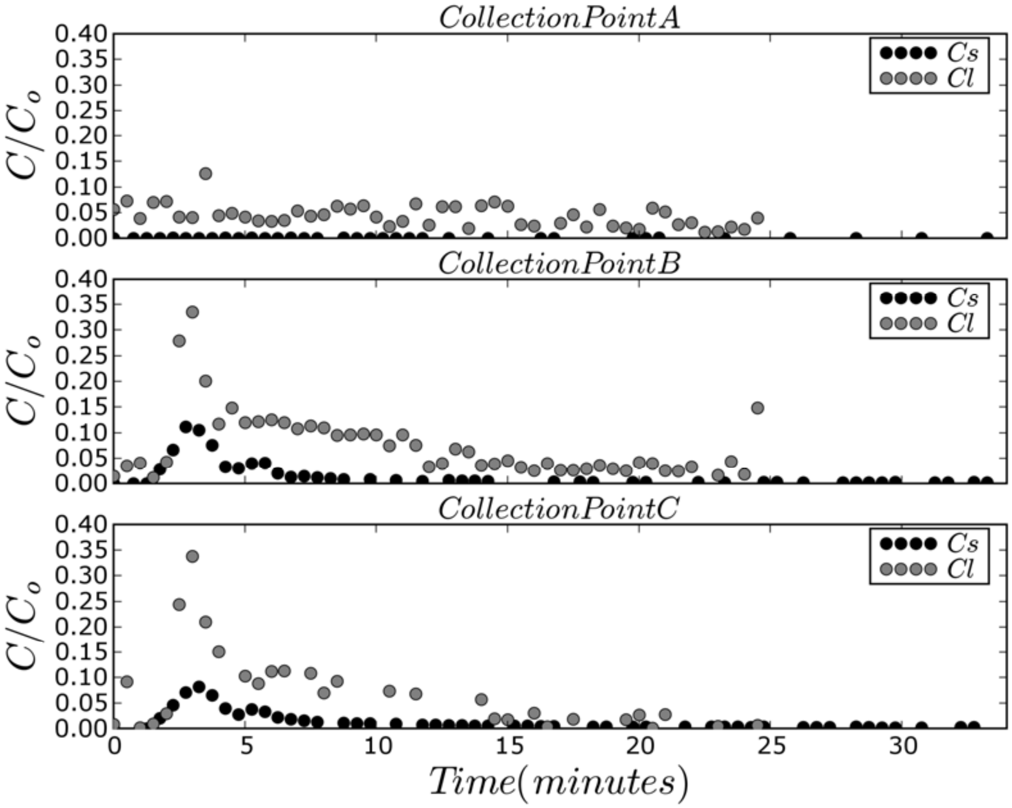

Figure 4.14: Measured Cs⁺ and Cl⁻ breakthrough curves for sample points A, B, and C from Burnet County.

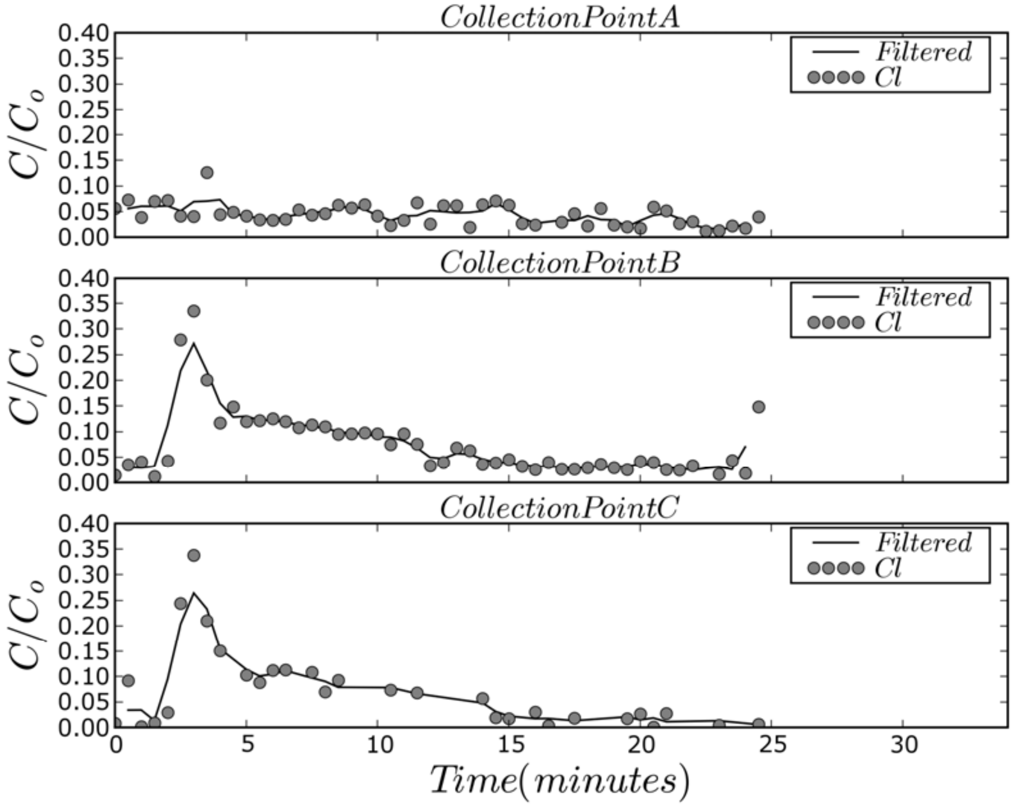

Figure 4.15: Cl⁻ breakthrough curves with a smoothing 3-point averaging filter.

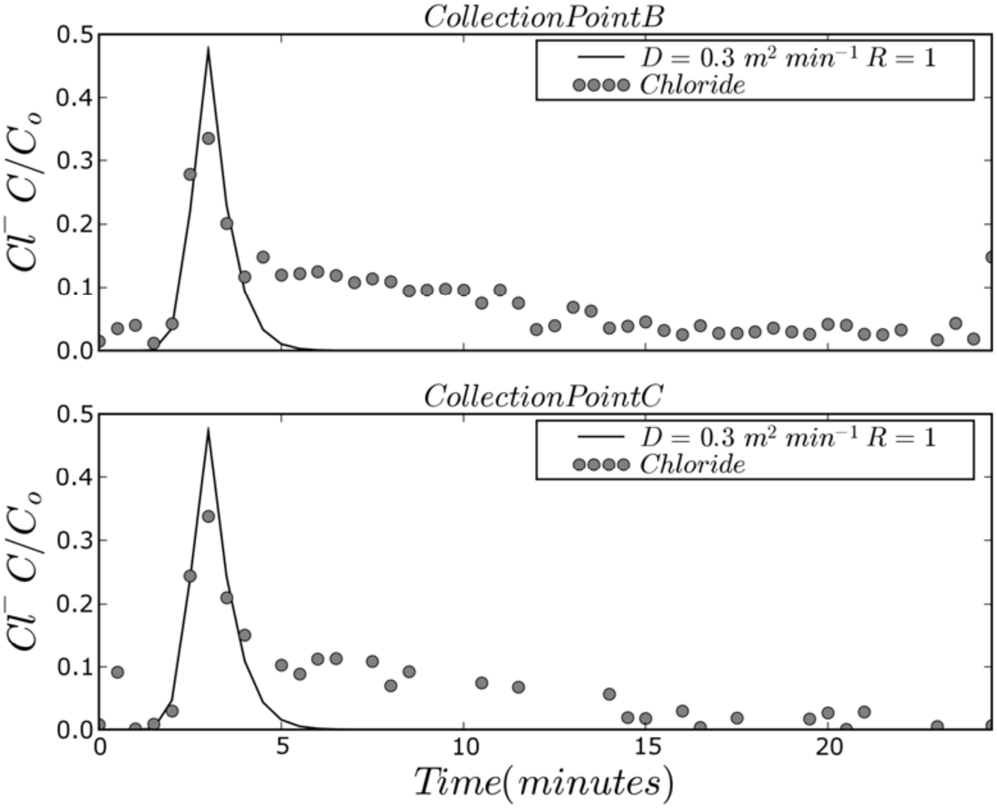

Figure 4.16: Cl⁻ breakthrough curves with best fits for advection-dispersion equation at sample points B and C.

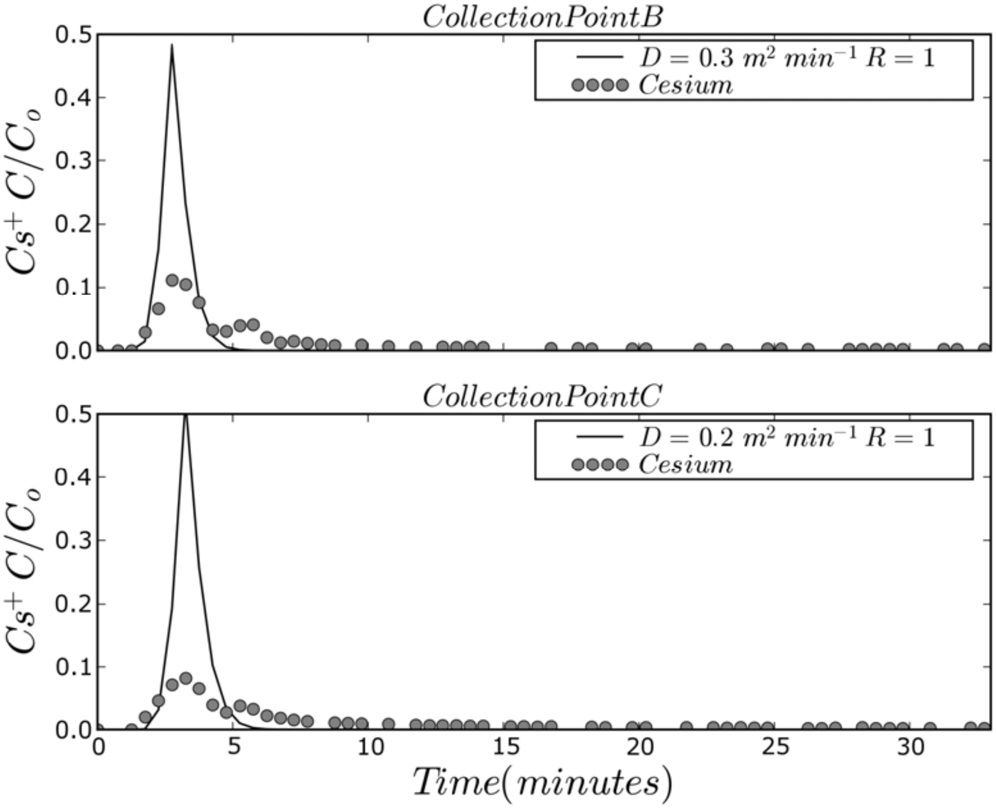

Figure 4.17: Cs^+ breakthrough curves with best fits using the advection-dispersion equation at sample points B and C.

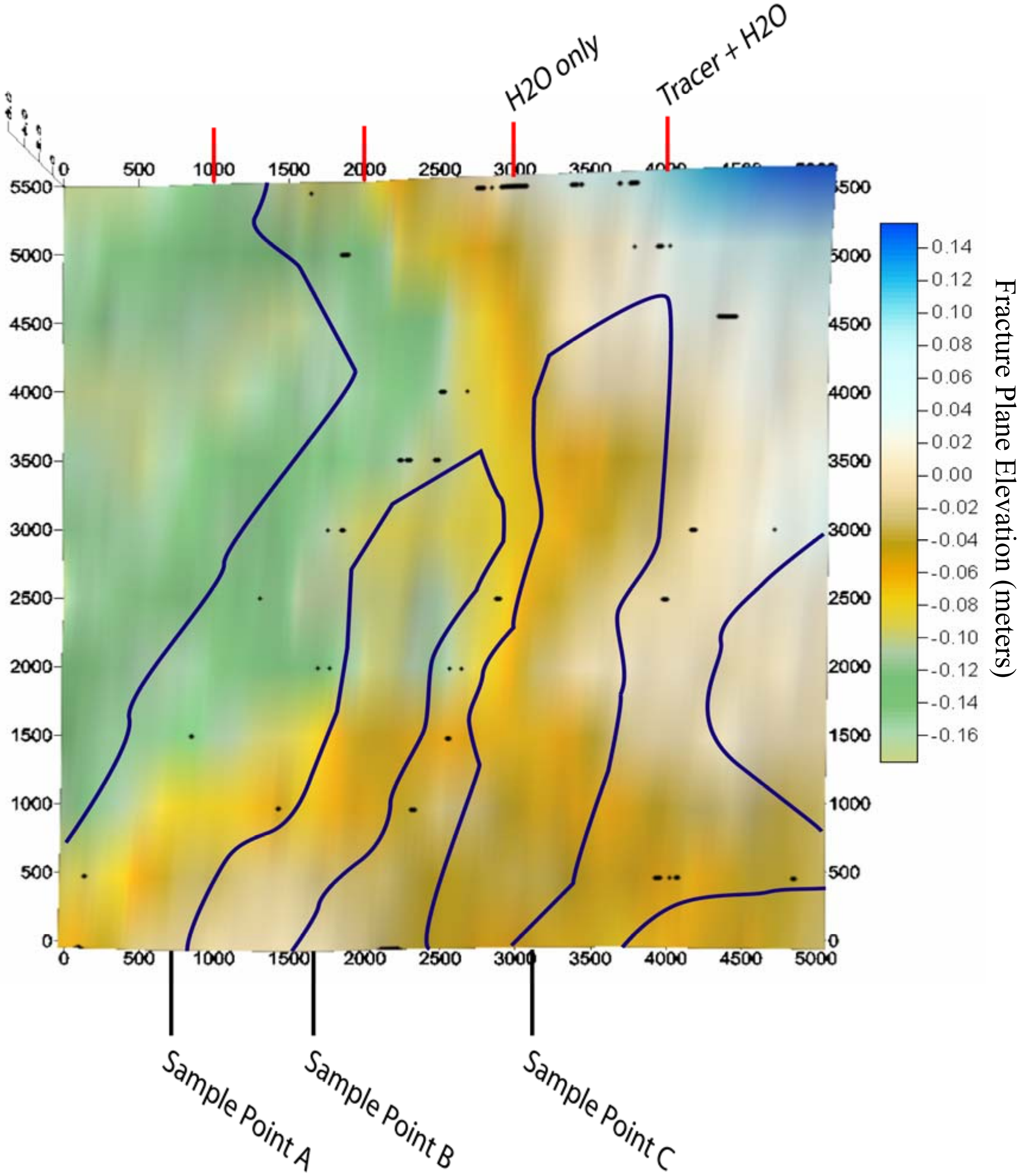

Figure 4.18: GPR image of the Burnet County fracture with black dots showing intensity change between water and saline solution and proposed channels based on tracer location and grid boundary constraints.

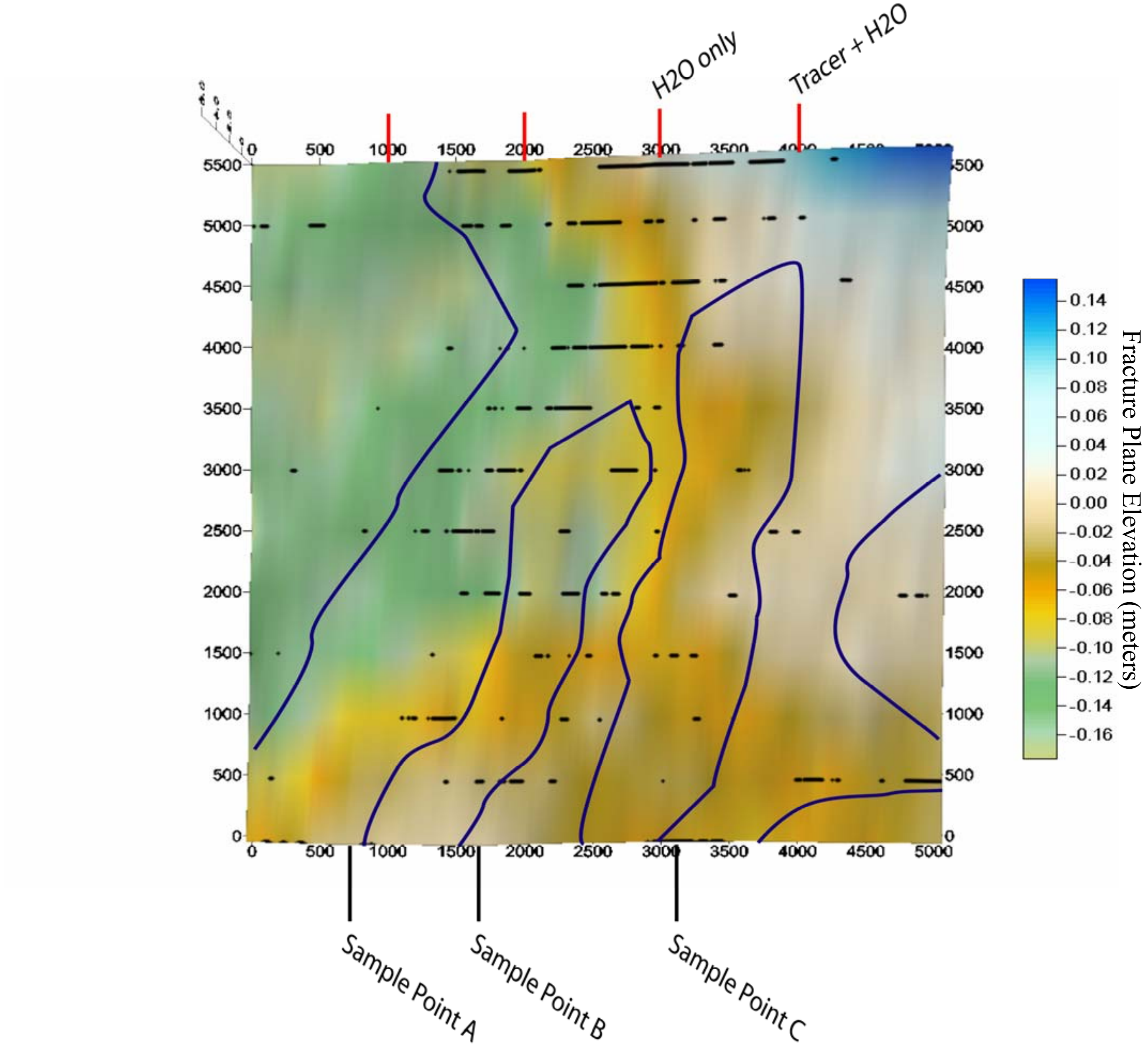

Figure 4.19.: GPR image of the fracture from Burnet County with black dots showing locations of phase from air to water. The channels overlain are from the proposed saline channels.

						Advection Dispersion	
	Tracer	**x (meters)**	**v ($m\ min^{-1}$)**	**b (cm)**	**D ($m^2\ min^{-1}$)**	**D_M ($m^2\ sec^{-1}$)**	**α_L (m)**
Mount Wudina							
Sample Point 1	Na	11.6	--	--	--	2.56×10^{-9}	--
Sample Point 1	Cs	11.6	--	--	--	1.82×10^{-9}	--
Sample Point 3	Na	13.6	--	--	--	2.56×10^{-9}	--
Sample Point 3	Cs	13.6	--	--	--	1.82×10^{-9}	--
TDS run 1	NaCl	13.6	3.3	0.06	25	7.57×10^{-9}	7.58
TDS run 2	NaCl	13.6	3.3	0.06	6	7.57×10^{-9}	1.82
Minnipa Hill							
Sample Point 1	Na	1.5	0.5	0.02	0.02	2.56×10^{-9}	0.04
Sample Point 2	Na	4.5	1.3	0.04	0.1	2.56×10^{-9}	0.08
Sample Point 3	Na	6.7	1.7	0.05	0.3	2.56×10^{-9}	0.18
Burnet County							
Sample Point A	Cl	6.4	1.8	0.23	--	--	--
Sample Point B	Cl	6.0	2	0.23	0.3	5.01×10^{-9}	0.15
Sample Point C	Cl	5.6	1.9	0.22	0.3	5.01×10^{-9}	0.16
Sample Point A	Cs	6.4	1.5	0.21	--	--	--
Sample Point B	Cs	6.0	2.2	0.24	0.3	1.82×10^{-9}	0.14
Sample Point C	Cs	5.6	1.7	0.21	0.2	1.82×10^{-9}	0.12

Table 4.01: Summary of calculated flow and transport properties.

Chapter 5

Conclusions and Future Work

General Conclusions

“Fracture skins” are defined as any physical, chemical, or biological alteration at the fracture surface that can enhance or impede fluid flow and solute transport (Moench, 1984; Kreisel and Sharp, 1996; Landrum, 2000; Robinson et al., 1998; Sharp, 1993; and Zimmerman et al., 2002). In spite of the existence of fracture skins, the impact of fracture skins on solute transport in fractured granitic rocks is commonly ignored. Prediction work that does account for fracture skins has limited datasets from which infer transport properties and, even where data are readily available, prediction of flow and transport in fracture systems is inherently uncertainty.

Granites from different climatic regions are sampled for alterations along fracture surfaces: Elberton Granite (Georgia), Town Mountain Granite (Texas), and Calca Granite (South Australia). Site observations, bulk chemical analyses, and optical analyses indicate that formation of granite fracture skins is a function of: 1) thickness of overlying soils; 2) compressional stress; 3) fracture orientation; 4) external sources (soluble salts); and 5) petrology and mineral textures.

All fracture skin samples are taken in the shallow subsurface. Outcrop profiles show fracture skin formation and rock alteration is pervasive in the top few meters at all locations. Thin sections and laboratory porosity measurements of rock matrix sampled in the top few meters of outcrop have greater than expected available porosity. At sites with thicker overlying soils, fracture alterations are dominated by clay coatings and iron-stained surfaces decreasing effective porosity. Weathering rinds and iron bands tend to form along subhorizontal fractures increasing effective porosity in the weathering rinds and decreasing porosity in the iron bands. Subvertical fractures are dominated by surface coatings, particularly pyrolusite, controlled by redox reactions.

Laser ablation was used to estimate diffusion coefficients in the samples. The use of laser ablation ICP-MS is relatively new to the field of geology and virtually non existent to hydrogeology. Chromatograms show linear features that correlate to microfractures, grain boundaries, or cleavage planes. The linear features show diffusion on the laboratory scale exists and actual paths of travel can be determined. Diffusion coefficients estimated using LA-ICP-MS are about two orders of magnitude higher than previously reported. This difference is contributed to sampling from the surface where stresses are reduced and the granite has relaxed. Analyses indicate that the method presented is useful and the derived diffusion coefficients are appropriate for granites at the near surface. This work shows and hypothesizes several applications for determining transport properties using LA-ICP-MS. Applications include estimating diffusion coefficients, mapping diffusion pathways, determining tortuosity, and inferring preferential sorption.

Tracer tests were conducted at three field sites: 1) Mount Wudina, South Australia, 2) Minnipa Hill, South Australia, and 3) Burnet County, Texas. Tracer breakthrough curves for all three field sites show characteristics related to channeling. Knowledge that flow is channeled also comes from visible evidence from fracture discharge. GPR is shown to be a potentially useful tool for mapping channels in a single granite fracture. Inferred channels from saline solutions indicate the preferred transport pathways within a fracture. On the small field scale, in a single fracture tracer is continuously transported in streams, not in plumes. Inferred channels match the greatest accumulation of tracer in the fracture, imaged using GPR, to the tracer test sample point with the greatest recovery of tracer.

Summary of Fracture Skin Properties

Transport properties of the granites and dominant skins for the three field sites are summarized. Porosity measurements using mercury injection porosimetry for the Elberton Granites the mean surface coating porosity is 1.81% and the granite matrix is 2.62%. Calculated mean porosities for the weathering rinds is 8.0%, which is significantly higher than that of iron precipitate (1.66%) and matrix (2.4%) in the Town Mountain Granite. Porosity measurements from the Calca granites show mean weathering rind porosity of 11.28%, mean surface coating porosity of 4.53%, mean iron band porosity of 2.33%, and rock matrix averages of 3.79%.

Micro-porosity measurements were estimated using the BET method. Disaggregated Elberton Granite fracture skin of clay coating (0.138%) is greater than the rock matrix (0.121%). The Town Mountain Granite matrix (0.126%) is slightly more porous than the Elberton Granite matrix (0.121%). Micro-porosity of the combined weathering rind and iron band increases to 0.147% from 0.126% in the rock matrix. The representative sample of Calca Granite shows micro-porosity is lowest in the weathering rind (0.126 %) the rock matrix being the middle porosity (0.14 %) and the most porous grains compose of the iron banded section (0.176%) of the sample.

Estimation of retardation factors was done using one of two assumptions; the first is that the granite samples are analogous to a porous media. The retardation factor for rock matrix of Elberton Granite is 17 and increases in the clay coating to 32. The Town Mountain Granites show virtually no change in R between the rock matrix (R = 8) and fracture skin (R = 7). Calca Granites show a decreasing trend from 170 in the matrix to 10 in the iron band to 4 in the weathering rind.

The second assumption for estimating retardation factors is that the effective transport pathways into the granite samples are analogous to a fracture. Using the mean pore throat diameter as the fracture aperture, retardation factors for the Elberton Granites are 9 in the rock matrix and 32 in the clay coating. Rock matrix of the Town Mountain Granite is estimated to be 13 and the combined iron band and weathering rind sample is 4. In the Calca Granite the rock matrix is 11, the iron band is 6, and the weathering rind is 4.

The effective diffusion coefficients for cesium (Cs) are 9×10^{-11} m^2 sec^{-1} in the rock matrix of Elberton Granite and 1.75×10^{-11} m^2 sec^{-1} in the clay coating fracture skin. In weathering rind and iron banded alteration samples from the Calca Granite (South Australia) the diffusion coefficients are estimated at 3.8×10^{-11} m^2 s^{-1} and 1.9×10^{-12} m^2 s^{-1}, respectively.

Suggested Future Work

Mineral composition of rock matrix and alteration zones is fundamental in determining what reactions occur during weathering. At this time x-ray defraction cannot be used to determine mineralogy because at least 5% of each mineral in a sample must be present to be detected. For clay minerals forming the clay coating, 5% of the sample must be the clay that forms the skin. Future work should include method development to separate clays or utilize *insitu* clay in fracture skins for mineral identification using x-ray defraction. The use of wet chemistry is useful in determing the bulk chemistry but normalization of these data require knowledge about mineral abundances.

The BET method was applied to disaggregated samples. This provides information about porosity on a grain scale. Information about rock samples is required with greater precision than mercry injection provides. Porosities for this study are adequate, but might be more precise by applying the BET method to consolidated rock samples.

Sample preparation for this study was aproached with the assumption that cut samples would have different transport properties than uncut samples. Addressing this assumption in future work could make sample preparation easier and simplify the modeling process.

Determining distribution coefficients using batch experiments is not representative of the amount of mass adsorbed in a fracture. Transport through a fracture has been shown to smaller amounts of mass than is represented in a disaggregated sample. The best way to measure sorption in a fracture is to transport mass through a fracture and determine retardation from the results. This can be done in the field or in the laboratory. Future work might include the combination of laboratory methods by Zimmerman et al., (2002) and utilization of small scale field sites to expand Zimmerman's work. In general work, regarding retardation is sparse in the literature and more work is needed.

The diffusion method discussed is a pilot study. Switching media to a relatively homogeneous sandstone would allow for more rapid turnover of sampleing, because diffusion coefficients would be more uniform. Multiple samples need to examined allowing progressively longer times in solution to address repeatability. Different methods of drying or not drying samples needs to be tested. This potentially will answer the question about what is happening on the rising limb of the penetration curves.

Monitoring cation ratios along each transect of a sample will allow grain boundaries to be delineated in the two dimensional sample. I predict that cation ratios and tracer distributions will show preferential sorption by certain minerals. This is of use when working with granites or more heterogeneous media. When mapping, spacing of the transects should to scaled depending on grain size (larger grain size can have a larger spacing). I also suggest that laser ablation method can be used for dating fractures. Iron bands and liesigng bands commonly show gradation in hand sample. By measuring the iron profile through these bands a diffusion coefficient can be determined. If the chemical reactions are limited by the ability to migrate product through the sample (Le Châtelier's principle) then time can be determined.

The use of cations and anions prove to be a useful combination for isolating effects from breakthrough curve data, but the number of samples required to generate multiple breakthrough curves to show variations between of reactive verses conservative tracers is costly. The use of multiple collection points also increases cost. A potential solution is to use a conservative dye that can be continuously monitored in the field and take grab samples for a reactive tracer. If water from quarries is being used, the conservative tracer should not be a constituent that concentrates with evaporation (i.e., Cl^-).

Using GPR to map channels is a useful tool in the field, but the frequency should be above 900 Mhz for shallow fractures (less than 1 meters). On bornhardts, fractures can have apertures on order of centimeters. These should be avoided because the tracer test will be very rapid making sampling difficult and near impossible to map using GPR.

Refernces:

Abelin, H., Neretnieks, I., Turnbrant S. , and Moreno, L., 1985, Final report of the migration in a single frature, Experimental results and evaluation, Stripa Proj. Tec. Rep., Nucl Field Safety Proj., Swed. Nucl. Fuel and Waste Manage Co. pp. 85-103.

Abelin, H., Birgersson, L., Agren, T., and Neretnieks, I., 1988, A channeling experiment to study flow and transport in natural fractures. Proceedings Scientific Basis of Nuclear Waste Management XII, edited by L. Lutze and R. C. Ewing, Mater. Res. Soc. Symp, Elsevier Science, v.127, pp. 661-668.

Abelin, H., Birgersson, L., Wilen, H. Agren, T., Moreno, L., and Neretnieks, I., 1990, Channeling experiment. Stripa Project Tech. Rep. Nucl Fuel Safety Proj., Swed. Nucl. Fuel and Waste Manage. Co., Stockholm.

Alonso, U., Missana, T., Alessandro, P., Rigato, V., and Rivas, P., 2003, Study of the contaminant transport into granite microfractures using nuclear ion beam techniques. Journal of Contaminant Hydrology, v. 61, pp. 95-105.

Anderson, M. P. and Woessner, W. W., 1992, Applied groundwater modeling: simulation of flow and advective transport. Academic Press, San Diego, CA, p.381.

Aris R.,1956, On dispersion of a solute in a fluid flow in through a tube: Proc Royal Society London, Series A, 235: pp. 67-77.

Bain, G.W., 1931, Spontaneous rock expansion. Journal of Geology, v. 39, pp. 715-735.

Baker, J. H., Beetem, W. A., and Wahlberg, J. S., 1964, Adsorption Equilibria between Earth Materials and Radionuclides, Cape Thompson, Alaska. Open-File Report, U. S. Geological Survey, Reston, Va.

Barenblatt, G.I., Zheltov, I.P., and Kocina, I.N., 1960, Basic concepts in the theory of Seepage of homogeneous liquids in fissured rocks (strata). Journal of Applied Mathematical Mechanics (English translation), v.24, pp. 1286-1303.

Beagle, E.A., 1978, The weathering of granite, Llano region central Texas. Thesis (Masters)—The University of Texas at Austin.

Bear, J., 1972, Dynamics of Fluids in Porous Media. Elsevier, N. Y., pp 764.

Becker, M.W., 2003, The effect of tracer buoyancy on tracer experiments conducted in fractured crystalline bedrock. Geophysics Research Letters, v. 30, no. 3, p. 1116.

Becker, M.W. and Shapiro, A.M., 1998, Advection-dominated tailing of tracer breakthrough in fractured rock. In: Abstracts with Programs, Geological Society of America, v. 30, issue 7, pp. 323.

Becker, M. W.and Shapiro, Allen M., 2003, Interpreting tracer breakthrough tailing from different forced gradient tracer experiment configurations in fractured bedrock. Water Resources Research, v. 39, no. 1, pp. 1024-1037.

Bird, R. B., Stewart, W. E., and Lightfoot, E. N., 2002, Transport Phenomena. second edition, John Wiley and Sons, Inc., Madison,WI, p. 895.

Birgersson, L., Moreno, L., Neretnieks, I., Widen, H., and Igren T., 1993, A tracer experiment in a small fracture zone in granite. Water Resour. Res., v. 29, i. 12, pp. 3867-3878.

Black, J. H., 1993, Hydrogeology of fractured rocks-a question of uncertainty about geometry. In: Banks, D., Banks, S. (Eds.), Hydrogeology of Hard Rocks, Memoirs of the 24th Congress, International Association of Hydrogeologists 24, part 2, Oslo, Norway, pp.783-796.

Blatt, H. and Tracy, R.J., 1999, Petrology igneous, sedimentary, and metamorphic: second edition, W. H. Freeman and Company, New York pp. 529 .

Bonal, N. D., 2007, Fracture Characterization Using Waves: Field Experiments of Anisotropy and Channel Imaging. Dissertation (PhD)—The University of Texas at Austin, submitted.

Bourke, P. J., 1987, Channeling of flow through fractures in rock. paper presented at GEOVAL-87 International Symposium, Swed. Nucl. Power Insp.(SKI).

Bradbury, M. H., and Green, A., 1985, Measurement of important parameters determining aqueous phase diffusion rates through crystalline rock matrices. Journal of Hydrology, v. 82, pp. 39-55.

Bradbury, M. H., and Green, A., 1986, Investigations into the factors influencing long range matrix diffusion rates and pore space accessibility at depth in granite. Journal of Hydrology, v. 89, pp. 123-139.

Bradbury, M.H., Lever, D., and Kinsey, D., 1982, Aqueous phase diffusion in crystalline rock. in Scientific Basis for Nuclear Waste Management V, v. 11, pp. 569-578.

Bradley, W. C., Hutton, J. T., and Twidale, C. R., 1978, Role of Salts in Development of Granitic Tafoni. South Australia. Journal of Geology, v. 86, pp. 647-654.

Brusseau, M.L.,1993, The influence of solute size, pore water velocity, and intraparticle porosity on solute dispersion and transport in soil. Water Resources Research, v. 29, n. 4, pp. 1071-1080.

Carlos, B., 1985, Minerals in fractures in the unsaturated zone from drill core USW G-4. Yucca Mountain, Nye County, Nevada, Rep. LA-10415-MS, Los Alamos Natl. Lab.

Carlos, B., 1989, Fracture-coating minerals in the Topopah Spring Member and upper tuff of Calico Hills from drill hole J-13. Yucca Mountain, Nye County, Nevada, Rep. LA-11504-MS, Los Alamos Natl. Lab.

Charbeneau, R. J., 2000, Groundwater hydraulics and pollutant transport. Prentice Hall, Upper Saddle River, NJ, 593p.

Cook, P.G. and Simmons, C.T., 2000, Using environmental tracers to constrain flow parameters in fractured rock aquifers; Clare Valley, South Australia, Dynamics of Fluids in Fractured Rock. Geophysical Monograph 122, American Geophysical Union, pp. 337-347.

Crank, J., 1975, The mathematics of diffusion: second edition, Oxford University Press, 414p.

D'Alessandro, M., Mousty, F., Bidoglio, G., Guimerà, J., Benet, I., Sánchez-Vila, X., García Gutiérrez, M., and Yllera De Llano, A., 1997, Field tracer experiment in a low permeability fractured medium: results from El Berrocal site. Journal of Contaminant Hydrology, v. 26, pp. 189-201.

Dagan, G., 1990, Transport in heterogeneous porous formations; spatial moments, ergodicity, and effective dispersion. Water Resources Research, v. 26, no. 6, pp. 1281-1290.

Darwin, C., 1897, Journal of researches into the natural history and geology of the countries visited during the voyage of the H.M.S. Beagle round the world, under the command of Capt. Fritz Roy, R.N.D. Appleton, New York, 519 p.

Davis, J.L., and Annan, A. P., 1988, Ground-Penetrating Radar for High-Resolution Mapping of Soil and Rock Stratigraphy. Geophysical Prospecting, v.36, pp. 531-551.

Day-Lewis, F. D., Lane, J. W., Jr., Harris, J. M., and Gorelick, S. M., 2003, Time-lapse imaging of saline-tracer transport in fractured rock using difference-attenuation radar tomography. Water Resources Research, v. 39, no. 10, 14p.

De Boer, J.H., 1958, The shape of capillaries, in: The structure and properties of porous materials, D.H. Everett, F.S. Stone (eds.), Butterworth, London.

Dixon, J C., Campbell, S. W., Thorp, C. E., Darmody, R. G., 2006, Incipient weathering rind development on introduced machine-polished granite discs in an Artic alpine environment, Northern Scandinavia. Earth Surface Processes and Landforms, v. 31, i. 1, pp. 111-121.

Blissett, A.H., Parker, A.J., Crooks, A.F., 1988, Geologic map of Yardea. Geologic Survey of South Australia, Department of mines and energy, Adelaide, 1:250000.

Dorn, R., 1998, Rock Coatings: In, Developments in Earth Surface Processes 6, Elsevier, Amsterdam – Lausanne, 379p.

Drever, J.I., 1997, The geochemistry of natural waters: surface and groundwater environments. Prentice Hall, Upper Saddle River, NJ, 436p.

Driese, S.G., McKay, L.D., and Penfield, C.P., 2001, Lithologic and pedogenic influences on porosity distribution and groundwater flow in fractured sedimentary saporolite: a new application of environmental sedimentology. Journal of Sedimentary Research, v. 71, no. 5, pp. 843-857.

Eikenberg, I., Hoehn, E., Fierz, T. and Frick, U., 1994, Grimsel test site: Preparation and performance of migration experiments with radio isotopes of sodium, strontium and iodine. PSI Ber. 94-11, Paul-Scherrer-Inst., Villigen, Switzerland.

Einstein, A., 1905, Uber die von der molekularkinetischen Theorie der Warme gefordete Bewegung von in Ruhenden Flussigkeiten suspendierten Teinchen, Ann. Phys., 17, pp. 539-560.

Fetter, C. W., 1994, Applied Hydrogeology: New Jersey, Prentice Hall, ed. 3, 616 p.

Fiori, A., Dagan, G., 1999, Concentration fluctuations in transport by groundwater; comparison between theory and field experiments. Water Resources Research, v. 35, no. 1, pp. 105-112.

Freuhndlich, H. 1909, Kapillarchemie, Akademische Verlagsgesellschaft, Leipziz.

Fu, L., Milliken, K.L., and Sharp Jr., J.M., 1993, Porosity and permeability variations in fractured and liesegang-banded Breathirr sandstones (middle Pennsylvanian), eastern Kentucky: diagenetic controls and implications for modeling dual-porosity systems. Journal of Hydrology, v. 154, pp. 351-381.

Fuller, C.M. and Sharp Jr., J.M., 1992, Permeability and fracture patterns in extrusive volcanic rocks: implications from the welded Santana Tuff, Trans Pecos Texas. Geol. Soc. America Bull., 104, pp. 1485-1496.

Garner, T.T., Lansdown, J.M., Robinson, N.I., and Sharp, J.M., Jr., in preparation, Determining diffusion coefficients in granite using laser ablation ICP-MS.

Garner, T. T. and Sharp, J. M., Jr., 2004, Hydraulic Properties of Granite Fracture Skins and Their Effect on Solute Transport. 2004 U.S. EPA/NGWA Fractured Rock Conference: State of the Science and Measuring Success in Remediation, Portland, Maine.

Garrels. R. M., Dreyer, R. M. and Howland, A. L., 1949. Diffusion of ions through intergranular spaces in water-saturated rocks. Bull. Geol. Soc. Am. 60, pp. 1809-1828.

Goldich, S.S., 1938, A study in rock-weathering. Journal of Geology, v. 46, pp. 17-58.

Hadermann, J., and Heer, W., 1996, The Grimsel (Switzerland) migration experiment: integrating field experiments, laboratory investigations and modeling. J. of Contaminant Hydrology, v. 21, pp. 87-100.

Himmelsbach, T., Holtz, H., and Malozewski, P., 1998, Solute transport processes in a highly permeable fault zone of Lindau fractured rock test site. Ground Water, v. 36. n. 5, pp. 792-799.

Hutton, J. T., Lindsay, D. S. and Twidale, C. R., 1977, The Weathering of Norite at Black Hill, South Australia. Journal of the Geological Society of Australia, v. 24, Pt 1, pp. 37-50.

Jenne, E A., 1998, Adsorption of Metals by Geomedia: Variables, Mechanisms, and Model Appolications, Academic Press, San Diego, pp. 1-583.

Johansson, H., Siitari-Kauppi, M., Skålberg, M., and Tullborg, E.L., 1998, Diffusion pathways in crystalline rock-examples from Äspö-diorite and fine-grained granite. J. of Contaminant Hydrology, v. 35, pp. 41-53.

Kabala, Z.J., 2001, Sensitivity analysis of a pumping test on a well with wellbore storage and skin. Advances in Water Resources, v. 24, pp. 483-504.

Kazemi, H., 1969, Pressure transient analysis of naturally fractured reservoirs with uniform fracture distribution. Trans. Soc. Pet. Eng. AIME, v. 246, pp. 451-462.

Klinkenberg, L. J., 1951, Analogy between diffusion and electrical conductivity in porous rocks. Bulletin of the Geological Society of America, v. 62, pp. 559-564.

Kreisel, I., 1996, Fracture skins and their effect on solute transport in a fractured porous medium with examples from the Brushy Canyon Formation. West Texas, Thesis (Masters)—The University of Texas at Austin, 109 p.

Kreisel, I. and Sharp, Jr., J. M., 1996, Fracture skins in the Brushy Canyon Formation, The Brushy Canyon Play in Outcrop and Subsurface: Concepts and Examples, W. D. DeMis and A. G. Cole. Eds., PBS-SEPM Pub. #96-38. pp. 147-152.

Landrum, M. T., 2000, Hydrogeologic properties of fracture skins and their effects on radionuclide transport. Thesis (Masters)—The University of Texas at Austin, 132 p.

Lane, J.W., Buursink, M. L., Haeni, F. P., Versteeg, R. J., (2000). Evaluation of ground-penetrating radar to detect free-phase hydrocarbons in fractured rocks – results of numerical modeling and physical experiments. Ground Water, v. 38, no. 6, pp.. 929-938.

Langmuir, D., 1918, The adsorption of gases on plane surfaces of glass, mica, and platinum. J. Am. Chem. Soc 40: pp. 1361-1403.

Langmuir, D., 1981, The power exchange function; A general model for metal adsorption onto geological materials: In “Adsorption from Aqueous Solutions” (P. H. Tewari, Ed.), Plenum, N. Y., pp. 1-18.

Langmuir, D., 1997, Aqueous Environmental Geohemistry. Prentice Hall, Toronto, 600p.

Larsen. E. S., 1948, Batholith and associated rocks of Corona, Elsinore and San Luis Rey quadrangles, southern California. Geological Society of America Memoirs, v. 29, p. 182.

Lee, M. R. and Parsons I., 1995, Microtextural controls of weathering of perthitic alkali feldspars. Geochim. Cosmochim. Acta, v. 59, pp. 4465-4492.

Levens, R. L., Williams, R. E., and Rushton, D. R., 1994, Hydrogeologic role of geologic structures. Part 2: analytical models. Journal of Hydrology, v. 156, pp. 245-263.

Lever, D.A., Bradbury, M.H., and Hemingway, S.J., 1985, The effect of dead-end porosity on rock-matrix diffusion. Journal of Hydrology, v. 80, pp. 45-76.

Long, L., 2003, personal communication.

Loughnan, F.C., 1969, Chemical Weathering of the Silicate Minerals. Elsevier, New York, 154 p.

Lowenstern, J., 2000, C.I.P.W. Normalization Software, USGS.

Maloszewski, P., and Zuber, A., 1997, Comment on "Convergent radial dispersion in a double-porosity aquifer with fracture skin: Analytical solution and application to a field experiment in fractured chalk" by Allen F. Moench. Water Resources Research, v. 33, no. 3, pp. 497-500.

Maréchal, J. C., Dewandel, B., and Subrahmanyam, K., 2003, Contribution of hydraulic tests at different scale to the characterization of fracture network properties in hard rock aquifers. Water Resources Research, In Press.

Mazurek, M., Alexander, W. R. MacKenzie A. B., 1996, Contaminant retardation in fractured shales: matrix diffusion and redox front entrapment. Elsevier Science, Journal of Contaminant Hydrology, v. 21, pp. 71-84.

Mazurek, M., Jakob, A., and Bossart, P., 2003, Solute transport in crystalline rocks at Äspö—I: Geological basis and model calibration. Journal of Contaminant Hydrology, v. 61, pp. 157-174.

McKay, L. D., Cherry, J. A., Gillham, R. W., 1993a, Field experiments in a fractured clay till; 1, Hydraulic conductivity and fracture aperture. Water Resources Research, v. 29, no. 4, pp. 1149-1162.

McKay, L. D., Gillham, R. W., Cherry, J. A., 1993b, Field experiments in a fractured clay till; 2, Solute and colloid transport. Water Resources Research, v. 29, no. 12, pp. 3879-3890.

McKay, L. D., Sanford, W. E., and Strong, J. M., 2000, Field-scale migration of colloidal tracers in a fractured shale saprolite. Ground Water, v. 38, no. 1, pp. 139-147.

Melnyk, T., 1983, Diffusion in crystalline rock. Tech. Rec. TR-216, Atomic Energy of Canada Limited, pp. 242-254.

Moench, A. F., 1984, Double-Porosity models for a fissured groundwater reservoir with fracture skin. Water Resour. Res., v. 20, no. 7, pp. 831-846.

Moench, A., 1997, Reply. Water Resources Research, v. 33, no. 3, pp. 501-503.

Neretnieks, I., 1980, Diffusion in the rock matrix: An important factor in radionuclide retardation?, J. Geophys. Research, v. 85, no. B8, pp. 4379-4397.

Novakowski, K. S., Evans, G. V., Lever, D. A., and Raven, K. G., 1985, A field example of measuring hydrodynamic dispersion in a single fracture. Water Resour. Res., v. 24, i. 8, pp 1165-1174.

Parnell, J., Honghan, C., Middleton, D. Haggan, T., and Carey, P., 2000, Significance of fiberous mineral veins in hydrocarbon migration: fluid inclusion studies. Journal of Geochemical Exploration, v. 69-70, pp. 623-627.

Passchier, C.W., and Trouw, R.A.J., 1996, Micro-tectonics. Springer, Berlin, 289p.

Phyu, T., 2002, Transient modeling of contaminant transport in dual porosity media with fracture skins. Thesis (Masters), The University of Texas at Austin, 125 p.

Pickens, J. F. and Grisak, G. E., 1981, Modeling of Scale-Dependent Dispersion in Hydrogeologic Systems. Water Resources Research, v. 17, i. 6, pp. 1701-1711.

Raven, K. G., Novakowski, K. S., and Lapcevic, P. A., 1988, Interpretation of field tracer tests of a single fracture using a transient solute storage model. Water Resour. Res., v. 24, i. 12, pp. 2019-2032.

Robinson, N.I. and Sharp Jr., J.M., 1997, Analytical solution for solute transport in a finite set of parallel fractures with matrix diffusion. C.S.I.R.O. Mathematical and Information Sciences Report CMIS-C23, 26 p.

Robinson, N.I., Sharp Jr., J.M., and Kreisel, I., 1998, Contaminant transport in sets of parallel finite fractures with fracture skins. Journal of Contaminant Hydrology, v. 31, pp. 83-109.

Robinson, P.C. and Maul, P.R., 1991, Some experience with the numerical inversion of Laplace transforms. Math. Engng. Industry, v. 3, pp. 111-131.

Rudolph, D. L., Cherry, J. A., Farvolden, R. N., 1991, Groundwater flow and solute transport in fractured lacustrine clay near Mexico City. Water Resources Research, v. 27, no. 9, pp. 2187-2201.

Ruud, N.C. and Kabala, Z.J., 1997, Numerical evaluation of the flowmeter test in a layered aquifer with a skin zone. Journal of Hydrology, v. 203, pp. 101-108.

Sardini, P., Delay, F., Hellmuth, K., Porel, G., and Oila, E., 2003, Interpretation of out-diffusion experiments on crystalline rocks using random walk modeling. Journal of Contaminant Hydrology, v. 61, pp. 339-350.

Sharp, J.M., Jr., 1993, Fractured aquifers/reservoirs: Approaches, problems, and opportunities, In: Banks, D., Banks, S. (eds.), Hydrogeology of Hard Rocks, Memoires of the 24th Cong. International Association of Hydrogeologists, Oslo,Norway, 24, part 1, pp. 23-38.

Sharp, J. M., Jr., Garner, T. T., Phyu, T. and Robinson, N. Il, 2003, Solute Transport in Crystalline Rocks with Francture Skins: Proc., Int. Conference of Groundwater in Fractured Rocks, International Association of Hydrogeologists, Prague, Czech Republic.

Sharp, J.M., Jr., Smyth-Boulton, R.C., and Fuller,C.M., 1993, Permeability-porosity variations and fracture patterns in tuffs, In: Banks, D., Banks, S. (eds.), Hydrogeology of Hard Rocks, Memoires of the 24th Cong. International Association of Hydrogeologists, Oslo,Norway, 24, part 1, pp. 103-114.

Sharp, J.M., Jr., Robinson, N.I., Smyth-Boulton, R.C., and Milliken, K.L., 1995, Fracture skin effects in groundwater transport, In: Rossmanith, H.P. (Ed.), Mechanics of Jointed and Faulted Rock, A.A. Balkeme, Rotterdam, pp. 449-454.

Sharp, J.M., Jr., Kreisel, I., Milliken, K.L., Mace, R.E., and Robinson, N.I., 1996, Fracture skin properties and effects on solute transport, Geotechnical and environmental implications. Proceedings Second North Amer. Rock Mechanics Symposium, Montreal, 2, pp. 1329-1336.

Shikaze, S. G., Sudicky, E. A., Schwartz, F. W., 1998, Density-dependent solute transport in discretely-fractured geologic media; is prediction possible? Schwartz, Franklin W. (editor) (Ohio State University, Department of Geological Sciences, Columbus, OH, United States), Sudicky, E. A. (editor), Mass transport in variable-density flow systems, Journal of Contaminant Hydrology, v. 34, no. 3, pp. 273-291.

Singhal, B.B.S., and Gupta, R.P., 1999, Applied hydrogeology of fractured rocks. Kluwer Academic Publishers, Dordrecht, The Netherlands, 367p.

Skagius, K., and Neretnieks, I., 1982, Diffusion in crystalline rocks. Scientific Basis for Radioactive Waste Management-V, Werner, Lutze, editor, pp.509-518.

Skagius, K., and Neretnieks, I., 1985, Diffusivities in crystalline rock materials. Material Research Society Symposium Proceedings, v. 50, pp. 73-80.

Skagius, K., and Neretnieks, I., 1986, Diffusivity measurements and electrical resistivity measurements in rock samples under mechanical stress. Water Resources Research, v. 22, no. 4, pp. 570-580.

Skagius, K., and Neretnieks, I., 1986, Porosities and diffusivities of some nonsorbing species in crystalline rocks. Water Resources Research, v. 22, no. 3, pp. 389-398.

Skagius, K., and Neretnieks, I., 1988, Measurements of cesium and strontium diffusion in biotite gneiss. Water Resources Research, v. 24, no. 1, pp. 75-84.

Stafford, P., Toran, L., and McKay, L., 1998, Influence of fractured truncation on dispersion: a dual permeability model. Journal of Contaminant Hydrology, v. 30, pp. 79-100.

Steefel, C.I. and Lichtner, P.C., 1998, Multicomponent reactive transport in discrete fractures: I. Controls on reaction front geometry. Journal of Hydrology, v. 209, pp. 186-199.

Stober, I., and Bucher, K. (eds.), Hydrogeology of Crystalline Rocks. Kluwer Academic Publishers, Dordrecht, The Netherlands, 275 p.

Stormer, J. C., Jr., and Whitney, J. A., 1980, Geological, geochemical, and geophysical studies of the Elberton Batholith, eastern Georgia: a guidebook to accompany the 15th annual Georgia Geological Society field trip. Guidebook-Georgia Geological Society, v. 19, 134.p.

Sudickey, E.A., and Frind, E.O., 1982, Contaminant transport in fractured porous media: analytical solutions for a set of parallel fractures. Water Resources Research, v. 18, pp. 1634-1642.

Talbot, A., 1979, The accurate numerical inversion of Laplace transforms. J. Inst. Math. Applicns., v. 23, pp. 97-120.

Talley, J., Baker, G. S., Becker, M. W., and Beyrle, N., 2005, Four dimensional mapping of tracer channelization in subhorizontal bedrock fractures using surface ground penetrating radar. Geophysical Research Letters, v. 32

Tang, D.H., Sudicky, E.A., and Frind, E.O., 1981, Contaminant transport in fractured porous media: analitical solution for a single fracture. Water Resources Research, v. 17, pp. 555-564.

Taylor, G., 1953, Dispersion of soluble matter in solvent flowing slowly through a tube. Proc Royal Society London, Series A, 219, pp. 186-203.

Thoma, S. G., Gallegos, D. P., and Smith, D. M., 1992, Impact of fracture coatings on fracture/matrix flow interactions in unsaturated, porous media. Water Resour. Res., v. 28, no. 5, pp. 1357-1367.

Tokunaga, T.K. and Wan, J., 2001, Surface-zone flow along unsaturated rock fractures. Water Resour. Res., v. 37, i. 2, pp. 287-296.

Tsang, C.-F., and Neretnieks, 1998, Flow channeling in heterogeneous fractured rocks. Reviews of Geophysics, v. 36, i. 2, pp. 275-298.

Tsoflias, G. P., and Sharp, J. M., Jr., 1998, Three-dimensional hydrogeologic characterization of fractured carbonate aquifers using ground-penetrating radar. Gulf Coast Association of Geological Societies Transactions, v. 48, pp. 439-338.

Twidale, C. R., 1982, Granite Landforms. Elsevier, Amsterdam, 372 p.

Twidale, C. R.., 1986. Granite landform evolution: factors and implications. Geol. Rundsch, v.75, pp. 769-779.

Twidale, C. R., 2005, personal communication.

Twidale, C. R. and Bourne, J. A., 2000, Rock Bursts and Associated Neotectonic Forms at Minnipa Hill, Northwestern Eyre Peninsula, South Australia. Environmental & Engineering Geoscience, v. 2, pp. 129-140.

Twidale, C. R., 2002, The two-stage concept of landform and landscape development involving etching: origin, development and implications of an idea. Earth-Science Reviews, v. 57, pp. 37-74.

Twidale, C.R., Bourne, J.A., and Romani, V., 2004, Identification of exposed weathering fronts. Geodinamica Acta, v. 17, pp. 107-123.

Twidale, C. R., Romani, V., Campbell, E. M. and Centeno, J. D., 1996. Sheet fractures: response to erosional offloading or to tectonic stress? Zeitschrift für Geomorphologie Supplement Band, v. 106, pp. 1-24

van Bemmelen, J. M., 1878, Das Adsorptionsvermogen der Ackererde. Landwirtsch.Vers. Stat. v. 21, pp. 135-191.

van Bemmelen, J. M., 1888, Die absorptions Verbindungen und das Absorptions Vermögen der Ackererde. Landwirtsch, Vers. Stat. v. 35, pp. 69-136.

van Genuchten, M.T. and Alves, W.J., 1982, Analytical Solutions of the one-dimensional convective-dispersive solute transport equation. U.S. Department of Agriculture, Tech. Bull. No. 1661, 151pp.

Vandergraaf, T. T., Ticknor, K. V., and Melnyk, T. W., 1993, The selection of a sorption database for the Geosphere model in the Canadian Nuclear Fuel Waste Management Program. J. Contam. Hydrol., v. 1, pp.327-345.

Vilks, P., Cramer, J. J., Jenson, M., Miller, N. H., Miller, H. G., and Sanchell, F. W., 2003, In situ diffusion experiment in granite: Phase I. Journal of Contaminant Hydrology, v. 61, pp. 191-202.

von Eynatten, H., Barceló-Vidal, C., and Pawlowsky-Glahn, V., 2003, Modeling compositional change: The example of chemical weathering of granitoid rocks. Mathematical Geology, v. 35, no. 3, pp. 231-251.

von Humboldt, A., 1812, Personal narrative of travels to the equinoctial regions of America during the years 1799-1804 V. II (Translated and edited by T. Ross in 1907), George Bell and Sons, London, 521 p.

Wadden, M.M., and Katsube, T.J., 1982, Radionuclide diffusion rates in igneous crystalline rocks. Chem. Geol., 36, pp. 191-214.

Wahlberg, J. S., Baker. J. H., Vernon. R. W., and Dewar, R;. S., 1965, Exchange Adsorption of Strontium on Clay Minerals. Bull. 1140-C. U. S. Geological Survey, Reston, Va., pp. C1-C26.

Wahlberg, J. S., and Fishman, M. J., 1962, Adsorption of Cesium on Clay Minerals. Bull. 1140-A. U. S. Geological Survey, Reston, Va., pp. A1-A30.

Wallach, R. and Parlange, J.-Y., 1998, Modeling transport in a single crack by the dual-porosity concept with a boundary layer at the interface. Journal of Contaminant Hydrology, v. 34, pp. 121-138.

Wang, H. F. and Anderson, M.P., 1982, Introduction to groundwater modeling: finite difference and finite element methods. W. H. Freeman and Co., San Francisco, CA, 233p.

Warren, J.E., and Root, P.J., 1963, The behavior of naturally fractured reservoirs. Trans. Soc. Pet. Eng. AIME, v. 228, issue 3, number 3, pp. 245-255.

Wels, C., and Smith, L., 1994, Retardation of sorbing solutes in fractured media. Water Resour. Res., v.30, i.9, pp.2547-2563.

Wels, C., Smith L., and Vandergraaf, T. T., 1996. Influence of Specific Surface Area on Transport of Sorbing Solutes in Fractures: an Experimental Analysis. Water Resour. Res., v. 32, i. 7, pp 1943-1954.

Wohletz, K.H., 1981, Scanning electron microscopy of basaltic ash, In: Abstracts with Programs, Geological Society of America, v. 13, i. 7, pp. 584.

Wood, W. W., Kraemer, T. F. and Hearn, P. P., Jr., 1990, Intragranular Diffusion: An Important Mechanism Influencing Solute Transport in Classic Aquifers?. Science, v. 247, pp. 1569-1572.

Wood, W. W., Shapiro, A. M., and Hsieh, P. A., 1996, Observational, experimental and inferred evidence of solute diffusion in granite rocks—Examples from the Mirror Lake watershed, Grafton County, New Hampshire, in Morganwalp, D. W., and Aronson, D. A., eds., U.S. Geological Survey Toxic Substances Hydrology Program—Proceedings of the Technical Meeting, Colorado Springs, Colorado, September 20-24, 1993: U.S. Geological Survey Water-Resources Investigations Report 94-4015, pp. 167-170.

Zhang, D. and Winter, C.L., 2000, Theory, modeling, and field investigation in hydrogeology: a special volume in honor of Shlomo P. Neuman's 60th birthday, Geological Society of America, Special Paper 348, Boulder, CO, 245p.

Zimmerman, M. D., Bennett, P. C., Sharp, J. M., Jr., and Choi, W. J., 2002, Experimental determination of sorption in fractured flow systems. Journal of Contaminant Hydrology, v. 58, i. 1-2, pp. 51-77.

VITA

Terence Travis Garner was born in Atlanta, Georgia on April 6, 1975, the son of William Travis and JoAnn Garner. After completing his work at Lovejoy High School, Hampton, Georgia, in 1993, he began working as a Master Barber in Peachtree City, Georgia. In 1999 he entered The University of West Georgia at Carrollton, Georgia, were he received his Bachelor of Science in Geology in May 2002. In September 2002 he entered the Graduate School of The University of Texas.

Permanent Address: 4707 St. Michaels Ct. Sugar Land, Texas 77479

This dissertation was typed be the author.